
Transient analyses of accelerator driven systems using modal expansion techniques

PNR-131-2010-005

Frank Wols

August 2010

Delft University of Technology
Faculty of Applied Sciences
Department of Radiation Radionuclides Reactors
Section Physics of Nuclear Reactors

Transient analyses of accelerator driven systems using modal expansion techniques

Frank Wols

Supervisor:
dr.ir. Danny Lathouwers

Delft, August 2010

Abstract

To have a constant power level in a subcritical system an external source is required to compensate for the difference between neutron loss and production. In an *accelerator driven system* (ADS) the external source is provided by coupling an accelerator to a subcritical assembly. The shape of the neutron flux in an ADS is different from a conventional critical reactor due to this external source. The time-dependent behavior of an ADS is also different as the importance of the delayed neutrons is reduced with increasing subcriticality. The *analysis of transients* in accelerator driven systems is an important aspect to assess the safety of the reactor.

Transients inside an ADS can be analyzed numerically by solving the time-dependent neutron transport equation directly, but this is an expensive method. Alternative methods to describe the time-dependent neutron flux are provided by *modal expansion techniques*. In modal expansion techniques the neutron flux is expressed as a summation over the product of spatial modes and time-dependent coefficients. The main interest of this thesis is found in the use of alpha modes as the spatial modes of a modal expansion technique. The alpha modes lead to an uncoupled set of ODEs to describe the time-dependency of the expansion coefficients. Also lambda modes and a set of basis functions obtained by proper orthogonal decomposition were investigated as alternative spatial modes for the modal expansion technique. The PHANTOM code package was used in this work to calculate the alpha and lambda modes used in the modal expansion and to calculate reference solutions by solving the time-dependent neutron transport equation directly.

The alpha mode expansion technique was applied to a 1D-model and two 2D-models. The modal expansion was used to reconstruct the steady-state flux and the time-dependent flux during different transients. When the results are compared with the reference solutions it was found that the alpha modes can reconstruct the time-dependent neutron flux of an ADS quite accurately during a transient. There are however some problems in reconstructing the flux contributions associated with the very fast time scales due to difficulties in the determination of the higher alpha modes, which is computationally expensive and often less accurate for the higher modes. Improvements in the calculation of the alpha modes should improve the accuracy of the modal expansion technique.

During the thesis also a geometrical model was made of the GUINEVERE facility, located at SCK in Mol, to perform calculations of k_{eff}. The value obtained for k_{eff} was consistent with other reference calculations. Two transient scenarios were studied for this realistic 3D ADS model by solving the time-dependent transport equation directly. The calculation of the alpha modes in 3D was too expensive making it impossible to use alpha modes to reconstruct the transients of this 3D-model.

The lambda mode expansion technique was used to reconstruct the neutron flux in the same 1D ADS model. The reconstruction of the time-dependent flux by the lambda mode expansion led to quite inaccurate results, especially in the multi-group case. It is concluded that despite the short calculation time of the lambda modes the alpha modes are a much better option to describe the time-dependent neutron flux in an ADS accurately.

Finally the proper orthogonal decomposition was investigated as a possibility to provide the spatial modes for the modal expansion technique. It was possible to reconstruct the steady-state flux of the 1D ADS accurately with only a few POD basis functions. The POD has not been applied to time-dependent problems since application of the transport operator is required to calculate the expansion coefficients and the implementation would have been outside the scope of this thesis.

List of symbols

$\tilde{a}$	extrapolated boundary [cm]
$A_n(t)$	alpha mode expansion coefficient [-]
$B_l(t)$	lambda mode expansion coefficient [-]
B_1	geometric buckling [cm^{-1}]
$C_i(\vec{r},t)$	(time-dependent) precursor concentrations [cm^{-3}]
D	diffusion coefficient [cm]
E	neutron energy [eV]
$\langle f,g \rangle$	inner product of f and g
$\mathbf{F}$	fission operator
$h_n^e(x)$	FEM basis functions corresponding to node n on element e
h	mesh size used in the finite difference method [cm]
k_{eff}	effective multiplication factor [-]
k_∞	multiplication factor in an infinite system [-]
l_∞	average neutron lifetime in an infinite system [s]
$\mathbf{L}$	transport operator (including scattering)
L	diffusion length [cm]
$L(t)$	neutron loss rate [s^{-1}]
$P(t)$	neutron production rate [s^{-1}]; also used as reactor power in section 2.2.5
$Q(\vec{r},E,\hat{\Omega},t)$	external neutron source [$cm^{-3}\cdot s^{-1}\cdot eV^{-1}$]
$\mathbf{Q}(\hat{\Omega})$	vector containing the spherical harmonics polynomials
$\vec{r}$	neutron position vector (x,y,z)
$R[\psi]$	least squares functional
t / Δt	time [s]; size of time-step during time-integration [s]
V / V_g	neutron velocity / group velocity [$cm\cdot s^{-1}$]
$Y_{l,m}(\hat{\Omega})$	spherical harmonics polynomials [-]
$Z_k(x,t_k)$	snapshot k used in the proper orthogonal decomposition
α_n	time-eigenvalues [s^{-1}]
β	delayed neutron fraction [-]
λ_i	decay constant of precursor i [s^{-1}]
λ_n	lambda-eigenvalues [-]
ν	average number of neutrons released per fission [-]
Σ_a	absorption cross section [cm^{-1}]
Σ_f	fission cross section [cm^{-1}]
Σ_s	scattering cross section [cm^{-1}]

Σ_t	total cross section [cm^{-1}]
$\hat{\Phi}_j(\mathbf{x})$	POD basis functions
$\phi(\vec{r},E,t)$ / ϕ_g	scalar neutron flux [$cm^{-2}\cdot s^{-1}\cdot eV^{-1}$] / group flux [$cm^{-2}\cdot s^{-1}$]
$\chi(E)$	fission spectrum [-]
$\psi(\vec{r},E,\hat{\Omega},t)$ / ψ_g	angular neutron flux [$cm^{-2}\cdot s^{-1}\cdot eV^{-1}$] / group flux [$cm^{-2}\cdot s^{-1}$]
$\psi^{\dagger}$	adjoint neutron flux [$cm^{-2}\cdot s^{-1}\cdot eV^{-1}$]
$\psi_{\alpha}(\vec{r},E,\hat{\Omega})$	alpha mode flux [$cm^{-2}\cdot s^{-1}\cdot eV^{-1}$]
$\psi_{\lambda}(\vec{r},E,\hat{\Omega})$	lambda mode flux [$cm^{-2}\cdot s^{-1}\cdot eV^{-1}$]
$\hat{\Omega}$	neutron direction vector [-]

Table of contents

1 Introduction

1.1 General introduction

In a conventional critical nuclear reactor the production rate of neutrons by fission is equal to the loss rate by absorption and neutron leakage making the nuclear chain reaction self-sustaining. In a subcritical reactor the fission chain reaction cannot sustain itself since more neutrons are lost, due to absorption and leakage, than produced. To have a constant power level in a subcritical system an external neutron source is required to compensate for the difference between neutron loss and production. In an *accelerator driven system* the external source is provided by coupling an accelerator to a subcritical assembly. The accelerator produces a beam of high-energy particles which cause the production of spallation neutrons in a target somewhere in the center of the subcritical assembly.

The neutrons produced by the spallation source have a very high energy and are therefore capable of incinerating actinides and transmuting long-lived radionuclides. The capability of reducing the lifetime of nuclear waste is one of the interesting features of the ADS.

Due to the subcriticality of the assembly the fission chain reaction cannot sustain itself any longer inside an ADS when the accelerator is turned off. In case of emergency this is an interesting benefit of the ADS. An important safety issue on the other hand is that the time scale on which the flux changes inside an ADS after a change of reactivity, for instance due to a variation in source intensity, can be much faster than in a critical assembly. In a critical assembly this time scale is associated with the delayed neutrons. For a subcritical configuration the role of the delayed neutrons is much smaller and the system will react faster to a reactivity change. So the *analysis of transients* of accelerator driven systems is very important with respect to the actual safety of the reactor.

The transients in an ADS can be analyzed numerically by solving the time-dependent neutron transport equation directly. From a computational point of view this is an expensive method since a high-dimensional partial differential equation must be solved to describe the time-dependent neutron flux. The time-dependent neutron flux can also be described by expressing the neutron flux as a summation over the product of spatial modes and time-dependent coefficients. These are *modal expansion techniques*. The so-called alpha modes are the most interesting option to use as the spatial modes. Using the alpha modes the time-dependent expansion coefficients can be described by an uncoupled set of ODEs and the time dependent part of the calculation is computationally cheap to perform. But also alternatives such as the lambda modes or a set of basis function obtained by proper orthogonal decomposition can be considered. For a critical system the neutron flux can be described by using only the fundamental mode, while the steady-state neutron flux of an ADS also requires the use of higher modes due to the subcriticality of the system and the influence of the source neutrons upon the flux shape.

1.2 The GUINEVERE project

An important example of an accelerator driven system is found in the GUINEVERE project. The GUINEVERE (GEneration of Uninterrupted Intense NEutrons pulses at the lead VEnus REactor) project is a major experiment with the main goal to develop and qualify different techniques for the reactivity monitoring of subcritical accelerator driven systems. Another goal of GUINEVERE is to create representative conditions of a lead-cooled ADS by a lead matrix core. The lay-out of the

VENUS critical facility, located at the SCK-CEN site in Mol, was modified into a lead-matrix core, the so-called VENUS-F core, to accommodate the GUINEVERE project.

The experimental set-up is made by coupling a fast lead simulated cooled reactor with the GENEPI-3C neutron generator. The GENEPI neutron generator consists of a 250 KeV deuteron accelerator producing 2,5 MeV-neutrons by the D(d,n)^{3}He or 14 MeV-neutrons by the T(d,n)^{4}He nuclear fusion reactions in a target. A drawing of the reactor building is shown in Figure 1.1.

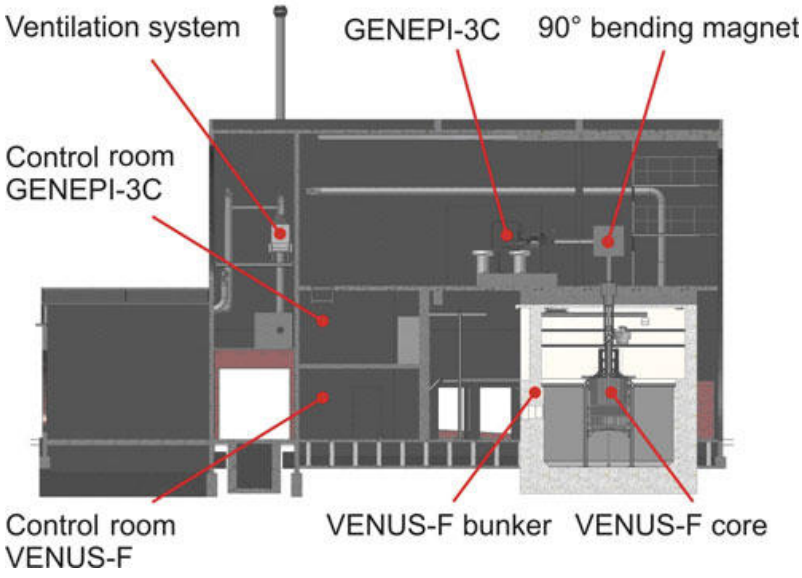

Figure 1.1 Schematic drawing of the GUINEVERE facility

The accelerator can be operated both in continuous mode and pulsed mode. Both are needed to validate different techniques for reactivity monitoring. In the predecessor of the GUINEVERE project, the MUSE project, the GENEPI-2 accelerator could only be operated in a pulsed mode. In the first stage of the project the reactor is operated in a critical configuration without the accelerator and later on in a subcritical configuration driven by the GENEPI-3C neutron generator.

1.3 The work in this thesis

This thesis work was performed as a Masters End Project (MEP) of the applied physics education at Delft University of Technology in the group Physics of Nuclear Reactors (PNR). The central question of the thesis is whether the flux expansion technique using alpha modes can accurately reconstruct the time-dependent neutron flux of an ADS during a transient. Important subquestions are related to the number of modes required to accurately describe the neutron flux and the influence of the delayed neutrons. Another question is whether the lambda modes and the POD basis functions can be used as an alternative basis for the modal expansion technique to describe the time-dependent neutron flux.

The influence of the delayed neutrons in an ADS is investigated in chapter 2. During the thesis the alpha and lambda modes are determined with the PHANTOM code package. The fixed-source or reference time-dependent calculations are also performed with PHANTOM. PHANTOM is an unstructured finite element neutron transport tool and the subject of the third chapter.

Ideally the alpha modal expansion technique should have been applied to the 3D model of the subcritical configuration of the GUINEVERE facility. Unfortunately it was computationally too demanding to calculate the alpha modes for this 3D model. Nevertheless calculations were performed of two different transients, turning on and off the source, to study the time-dependent behaviour of a

realistic 3D ADS-model. The results are presented in chapter 4 along with calculations of k_{eff} for the critical configuration.

The alpha mode expansion technique was applied to a 1D-model and two 2D-models in chapter 5. The models resemble the basic physical properties of a real ADS. The neutron flux is constructed by the alpha mode expansion for the steady-state problem and transient scenarios, such as turning off the source after operating at a constant power or switching on the source with zero initial flux. To check the accuracy of the alpha mode reconstructed flux reference solutions were calculated by performing the full time-dependent transport calculation with PHANTOM.

Two alternative bases for a modal expansion technique are investigated in chapter 6. The lambda modes are used in a modal expansion and the results are compared for the 1D ADS-model with the reference solution and the alpha mode expansion. As a second alternative the basis functions obtained by the proper orthogonal decomposition were used to reconstruct the steady-state flux of the 1D ADS.

2 Kinetics of accelerator driven systems

2.1 ADS physics in literature

The physics of subcritical source driven systems can be quite different compared with the critical core configurations normally studied in reactor physics. This section aims to discuss some important aspects of the physical behavior of accelerator driven systems. Also some of the important computational methods used in literature to determine the transient behavior of accelerator driven systems are discussed.

2.1.1 Source dominance

In critical reactors the neutron distribution is governed by one fundamental eigenstate of the system. Without an external source all higher modes die out after a sufficient amount of time. For an ADS the presence of a source and the subcriticality of the system causes the neutron flux shape to deviate from the fundamental eigenfunction as subcriticality increases.

Ravetto [2000] states that the stationary neutron distribution in a source driven strongly subcritical multiplying system is dominated by the presence of the source and can be very different from the fundamental critical eigenstate. According to Ravetto [2000] the neutron distribution approaches the fundamental eigenstate for a system approaching criticality. Ravetto [2003] also states this in other words: for subcritical systems the importance of higher-order harmonics increases with increasing subcriticality. This relationship between the subcriticality level and the source dominance of the system is also recognized by Dulla [2003] and Saracco & Ricco [2009].

With respect to the safety of accelerator driven system, Ravetto [2000] also makes a few interesting remarks. Subcriticality makes accelerator driven systems safer than conventional reactors with respect to sudden insertions of positive reactivity since it is not possible for the nuclear chain reaction to grow out of control. For subcritical systems a (large) localized fixed perturbation only results in slight changes of the flux nearby the perturbed region of the system, while the distortion sharply increases for a system approaching criticality. Or in the words of Dulla [2003]: Source driven systems are more resistant to spatial neutron distribution distortions. An important safety issue however is raised by the rapidity of the power responses due to external or accident perturbations. This is strongly connected to the role of the delayed neutrons, which is expected to be much smaller in subcritical systems.

2.1.2 Delayed neutrons

In the operation of nuclear reactors very different time scales have to be considered [Ravetto et al. 2003]. On the one hand the very fast scale of the prompt neutrons ($10^{-4} \sim 10^{-6}\ s$) and on the other hand a much slower scale associated with the delayed neutrons ($10^{-1} \sim 10^{1}\ s$). These delayed neutrons are vital for effective control of the nuclear chain reaction in a critical nuclear reactor.

According to Ravetto [2000] it appears that the relative weight of the delayed neutron source is significantly reduced with the subcriticality level. As a consequence the power response to sudden perturbations is almost instantaneous for highly subcritical systems. For systems devoted to actinide transmutation the low delayed neutron fraction of the actinides can even worsen this situation.

Ravetto [2000] shows for a point reactor model that the weight of the delayed source with respect to the effective external neutron source reduces as subcriticality increases. This feature is also observed in more realistic space-energy models.

Saracco & Ricco [2009] presented a model for a subcritical neutron multiplying sphere coupled to an external time-dependent neutron source, within one group diffusion theory. The problem was solved without any other approximation. Saracco & Ricco [2009] also showed with their model that the importance of the delayed neutrons decreases as the subcriticality of the system increases.

Saracco & Ricco [2009] distinguish three different operating regimes for a subcritical assembly.
Very far from criticality (k_{eff} < 0.8 to 0.9) the system almost immediately responds to a variation of the source, only a fraction β of the power evolves with the time scale of the delayed neutrons. In this case time and space behavior of the system practically factorize. According to Ravetto [2000] this property makes so-called quasi-static methods very useful for time-dependent calculations of subcritical systems.
Close to criticality (k_{eff} > 0.95 to 0.97) the fundamental mode becomes more and more relevant and a simple time behavior (such as point-kinetics) of the system with one dominant fundamental mode is recovered.
In the *intermediate region (0.8 to 0.9 < k_{eff} < 0.95 to 0.97)* the behavior of the system is more complicated to describe.

2.1.3 Computational methods

Direct methods are a straightforward way to solve the time-dependent neutron transport (or diffusion) equations. But they are often computationally expensive and to solve time-dependent problems with precursors a very large number of small time-steps is needed to accurately describe the behavior of the prompt neutrons and still capture the evolution of the delayed neutrons [Cao, 2008]. To save computational effort other methods are often preferred.

The time-dependent behavior of a conventional critical reactor is often described by the point-kinetics approximation. The classical point-kinetic model is based upon the factorization of the neutron flux into the product of a time-constant shape function for the whole reactor and a time-dependent amplitude function. A system of equations in the time-domain can then be constructed to describe the evolution of the bulk of the neutron population [Bosio et al., 2001]. Obviously the point-kinetics model greatly reduces the computational effort required to determine the time-dependent behavior of a reactor.

In point kinetics only the fundamental eigenfunction of the operator appears in the neutron distribution at all instants. The neutron distribution of source driven systems may however involve a superposition of many eigenfunctions. As a consequence the eigenfunction interpretation of the point-kinetics model fails for subcritical source driven systems [Ravetto et al., 2003]. In general this makes the point-kinetics model inapplicable to describe the transient behavior of accelerator driven systems.

A natural extension of the point-kinetics model is the quasi-static scheme [Bosio et al., 2001]. In the quasistatic method the neutron flux is factorized as the product of a rapidly varying amplitude and a slowly varying shape vector. Knowing the shape, the evolution of the amplitude can be solved on a fast time scale and then the shape function can be solved on a much slower time scale, still significantly reducing the required computational effort with respect to direct methods. In the end the

amplitude is solved for each time-step and the shape is only recalculated a few times. Using only one shape calculation the quasi-static method reduces to the point-kinetics model [Ravetto, 2000].

Ravetto [2000] shows for a source-driven system three-dimensional system with hexagonal fuel elements that a correct representation of the power evolution requires several shape recalculations over the time interval. Using only one shape calculation (point-kinetics) the calculated power after some time is significantly smaller than the actual power.

For decoupled systems (e.g. accelerator driven systems with a fast and thermal region) the quasi-static method may require many shape recalculations. For these cases Bosio [2001] advises the use of a quasi-static scheme using multipoint equations. In multipoint methods, as described by Dulla & Picca [2006], the system is divided into a smaller number of macro-regions in phase-space and the neutron flux is factorized in the product of shape and amplitude functions on each subdomain.

Another group of methods for performing space-time kinetics are the modal expansion methods. In modal expansion methods the time-dependent neutron flux is expanded into known eigenfunctions, often called modes, describing the spatial dependence of the flux and unknown expansion coefficients describing the temporal dependence of the flux. Modal methods are used to obtain an economical, but accurate approximation of the time-dependent neutron flux.

The most common modes used in the modal expansion method, according to De Lima [2009], are the natural modes, also known as alpha modes, and the lambda modes. The alpha modes and lambda modes will be investigated during this thesis. The alpha modes are the eigenfunctions associated with the neutron balance and time-dependent precursor operators. The alpha mode expansion leads to a system of uncoupled modal equations describing the time-dependency of the system [De Lima et al., 2009]. Solving the system of uncoupled modal equations itself requires almost negligible computational effort.

The basic theory for the modal expansion method using alpha modes has been derived for the space-time neutron diffusion equation by Cao [2008]. Cao states that the modal expansion method is not very popular anymore because a large number of modes are required in order to obtain a sufficiently accurate solution, especially in regions with large perturbations. Cao [2008] mainly uses the modal expansion technique as a useful tool for analyzing the spatial effects in pulsed-neutron experiments. Verdu [2010] recommends the use of prompt alpha modes, when compared to lambda modes, to solve time-dependent source problems in subcritical configurations.

The Implicitly Restarted Arnoldi Method (IRAM) has been used by Lathouwers [2003] to calculate alpha modes in neutron transport. The IRAM offers the possibility to calculate a substantial number of alpha modes. An important objective of this thesis is to investigate the possibilities of using these alpha modes as a basis for a modal expansion method to perform space-time neutron kinetics for accelerator driven systems.

The lambda modes are the eigenfunctions associated with the steady-state neutron balance operator. The lambda eigenfunctions are relatively easy to calculate but also in this case complex eigenfunctions might occur [De Lima et al., 2009]. The modal expansion method based upon the lambda modes does not lead to an uncoupled system of equations. This is shown by González [2010] for a critical core configuration with perturbed fission and transport operators. The lambda modes are also investigated in this thesis as a possible basis for a modal expansion method.

2.2 The importance of delayed neutrons

In this section a reactor model based upon the one speed 1D diffusion equation with precursors is developed. The main purpose of this model is to study the role of the delayed neutrons in an ADS and to make a simple study of the influence of the level of subcriticality of an ADS upon the neutron flux shape.

The transient calculations performed later in this thesis take place on very short time scales ($\ll 1$ *ms*). Upon this time scale it is assumed that the contribution of delayed neutrons to the neutron flux can more or less be considered as a constant background. For this reason all calculations in this thesis work, except for this chapter, are performed with only prompt neutrons.

For two reasons it is however important to obtain more knowledge about the influence of delayed neutrons in the transient behavior of accelerator driven systems. The first reason is to check whether it is really a reasonable assumption to neglect the precursors during the calculations of these short-term transients. Secondly it is also relevant to have some idea what will happen on a longer time scale. The question is how the influence of the delayed neutrons in the power production of a reactor will vary as a function of the subcriticality of the system. In the end the 1D diffusion reactor model, which includes delayed neutrons, should give more knowledge about the time scales involved in an ADS.

Another reason to construct the 1D diffusion reactor model is to study the neutron flux shape as the subcriticality level of the ADS varies. According to literature discussed in section 2.1.1 the neutron flux becomes more source dominated as the subcriticality of the system increases. In the 1D-difussion model this behavior should also occur.

2.2.1 One dimensional homogeneous slab reactor model

To study the influence of the delayed neutrons and the effects of the source dominance with increasing subcriticality a simple 1-dimensional homogeneous slab reactor with a source in the center region was chosen and this case was studied in one-speed diffusion theory. The spatial discretization was performed by the finite difference method. A scheme of the spatial discretization of the homogeneous slab is given in Figure 2.1.

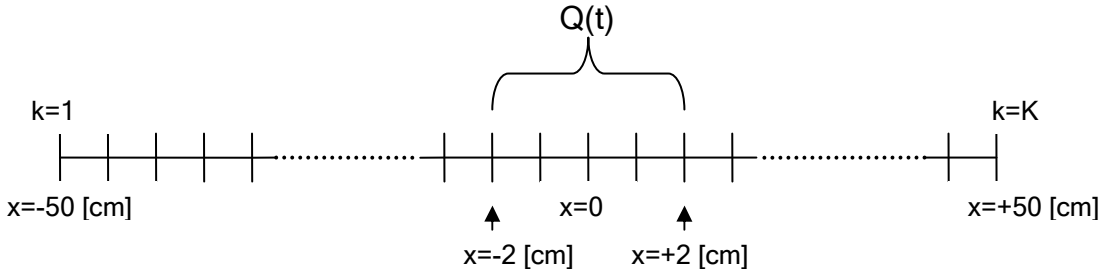

Figure 2.1 Spatial discretization scheme of the 1D ADS model

The neutron flux in one speed diffusion theory (with I precursor groups) is defined by

$$\begin{aligned} \frac{1}{V}\frac{\partial \phi}{\partial t} &= D\frac{\partial^2 \phi}{\partial x^2} - \Sigma_a \phi + (1-\beta)\nu\Sigma_f \phi + \sum_i \lambda_i C_i + Q \\ \frac{\partial C_i}{\partial t} &= -\lambda_i C_i + \beta_i \nu \Sigma_f \phi \qquad i = 1,2,...,I \end{aligned} \quad . \tag{2.1}$$

When the extrapolated length is neglected the boundary conditions are $\phi(-a/2,t)=0$ and $\phi(a/2,t)=0$, where a is the thickness of the slab reactor. When the source is turned on it is described as

$$q(x)=\begin{cases}1 & -2\le x\le 2\\ 0 & |x|>2\end{cases}. \tag{2.2}$$

The effective multiplication factor for such a system is, according to Duderstadt & Hamilton [1976], determined as

$$k_{eff}=\frac{\nu\Sigma_f}{\Sigma_a\left(1+L^2B_1^2\right)}, \tag{2.3}$$

where the diffusion length $L=\sqrt{\frac{D}{\Sigma_a}}$ and $B_1=\left(\frac{\pi}{a}\right)$.

The six precursor groups given in Table 2.1 are used in the calculations. These numbers are based upon values given by Duderstadt & Hamilton [1976] for U-235 with $\nu=2.5$.

Table 2.1 Delayed neutron fractions and decay constants of U-235

Group *i*	β_i	$\lambda_i\ (s^{-1})$
1	0.000254	0.0127
2	0.001421	0.0317
3	0.001254	0.1155
4	0.002716	0.3108
5	0.000854	1.3975
6	0.000173	3.8723

The values of some important constants in the calculations have to be chosen or determined. For the neutron yield ν a typical value of 2.5 is chosen. Scattering is assumed to be isotropic, so $D=1/3\Sigma_t$. The total delayed neutron fraction is given by $\beta=\sum_i\beta_i$. The neutron velocity V is set at $10^8\ cm{\cdot}s^{-1}$.

For the diffusion approximation to be valid it is desirable that Σ_a is small compared to Σ_t. To ensure this $\Sigma_t=1\ cm^{-1}$ and $\Sigma_a=0.2\ cm^{-1}$ was chosen during the calculations. In practice Σ_t is a bit smaller for uranium (Σ_t = 0.765 cm^{-1}, according to Duderstadt & Hamilton [1976]), but for computational simplicity 1 is a practical value to work with. It is also important to notice that the extrapolated distance ($1/\Sigma_t$) is small compared to the width of the whole slab reactor and can therefore be neglected. Σ_f will be varied during the calculation to obtain different subcriticality levels.

2.2.2 Solving the steady state flux with the 1D diffusive model

If the system is in a steady state ($\frac{\partial\phi}{\partial t}=0$, $\frac{\partial C_i}{\partial t}=0$) eq. (2.1) reduces to

$$\begin{aligned} D\frac{\partial^2\phi}{\partial x^2}&=\left(\Sigma_a-\nu\Sigma_f\right)\phi-q\\ C_i&=\frac{\beta_i\nu\Sigma_f}{\lambda_i}\phi \qquad i=1,2,...,I\end{aligned}, \tag{2.4}$$

where the steady-state neutron flux and the steady-state precursor concentrations are denoted by ϕ and C_i. The steady state neutron flux obviously does not depend on the precursor density.

The space dependence of the steady-state diffusion equation is discretized by finite differences. The x-domain is divided into K subintervals with length h, which leads to

$$\frac{\phi(x_{k-1})-2\phi(x_k)+\phi(x_{k+1})}{h^2}=\frac{\Sigma_a-\nu\Sigma_f}{D}\phi(x_k)-\frac{q(x_k)}{D}. \tag{2.5}$$

Since the extrapolated distance is neglected the boundary conditions are given by

$$\phi(x_1)=\phi(x_k)=0 \tag{2.6}$$

This can be written in matrix vector notation by writing

$$\mathbf{A}=\begin{bmatrix} 1 & 0 & 0 & 0 & 0 & 0 \\ -1 & 2+\frac{\Sigma_a-\nu\Sigma_f}{D}h^2 & -1 & 0 & 0 & 0 \\ 0 & -1 & 2+\frac{\Sigma_a-\nu\Sigma_f}{D}h^2 & -1 & 0 & 0 \\ 0 & 0 & -1 & \ddots & \ddots & \vdots \\ 0 & 0 & 0 & \ddots & 2+\frac{\Sigma_a-\nu\Sigma_f}{D}h^2 & -1 \\ 0 & 0 & 0 & \cdots & 0 & 1 \end{bmatrix},$$

$$\underline{\phi}=\begin{bmatrix}\phi(x_1)\\ \phi(x_2)\\ \vdots \\ \phi(x_K)\end{bmatrix}, \text{ and } \underline{q}=\frac{h^2}{D}\begin{bmatrix}q(x_1)\\ q(x_2)\\ \vdots \\ q(x_K)\end{bmatrix}$$

Now MATLAB can solve the following system

$$\mathbf{A}\underline{\phi}=\underline{q}. \tag{2.7}$$

Once the flux $\underline{\phi}$ is known the steady state precursor concentrations $\underline{C}_i$ can easily be calculated.

2.2.3 The steady state flux of the diffusive slab reactor

Calculations of the steady state neutron flux were performed for k_{eff} ranging from 0.9 to 0.9999. k_{eff} was varied by choosing the appropriate fission cross section Σ_f. The steady state neutron flux is normalized and plotted in Figure 2.2 for the different values of k_{eff}.

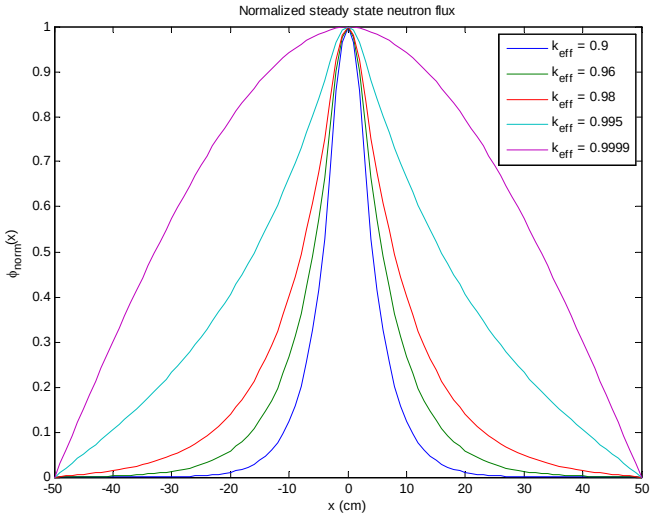

Figure 2.2 Normalized steady state neutron flux of the 1D diffusion problem for different k_{eff}

Interesting to notice is that shape of the neutron flux becomes more and more dominated by the source region as subcriticality increases. Only if the system is very close to criticality (k_{eff} = 0.9999) the cosine shape of the fundamental mode is recovered. The dominance of the source as subcriticality increases was already described in literature by Saracco & Ricco [2009], Dulla [2003] and Ravetto [2000]. The change in the shape of the neutron flux as subcriticality increases also illustrates that higher harmonics are needed to describe the neutron flux, and this is exactly why, according to Ravetto [2003], the point-kinetics model fails for (largely) subcritical systems.

2.2.4 Time dependent solution of the 1D diffusion problem

Now the steady state flux of the one-dimensional diffusive slab reactor can be determined. It is more interesting to determine the time-dependent solution of the problem since this should reveal the influence of the delayed neutrons during a transient in the system. By simply writing $\phi_k = \phi(x_k, t)$ and $C_{i,k} = C_i(x_k, t)$ the time dependent diffusion equation with finite difference discretization in the x-domain can be written as

$$\begin{aligned} \frac{1}{V}\frac{\partial \phi_k}{\partial t} &= D\frac{\phi_{k-1} - 2\phi_k + \phi_{k+1}}{h^2} - \Sigma_a \phi_k + (1-\beta)\nu\Sigma_f \phi_k + \sum_i \lambda_i C_{i,k} + Q_k \\ \frac{\partial C_{i,k}}{\partial t} &= -\lambda_i C_{i,k} + \beta_i \nu\Sigma_f \phi_k \qquad \forall i \end{aligned} \quad . \tag{2.8}$$

Now the time-integration is performed for each time-step n by means of implicit Euler, which leads to

$$\begin{aligned} \frac{1}{V}\frac{\phi_k^{n+1} - \phi_k^n}{\Delta t} &= D\frac{\phi_{k-1}^{n+1} - 2\phi_k^{n+1} + \phi_{k+1}^{n+1}}{h^2} - \Sigma_a \phi_k^{n+1} + (1-\beta)\nu\Sigma_f \phi_k^{n+1} + \sum_i \lambda_i C_{i,k}^{n+1} + Q_k^{n+1} \\ \frac{C_{i,k}^{n+1} - C_{i,k}^n}{\Delta t} &= -\lambda_i C_{i,k}^{n+1} + \beta_i \nu\Sigma_f \phi_k^{n+1} \qquad \forall i \end{aligned} \quad , \tag{2.9}$$

and upon rewriting

$$\begin{aligned} &\left(1 + V\Delta t\left[\Sigma_a - (1-\beta)\nu\Sigma_f + 2\frac{D}{h^2}\right]\right)\phi_k^{n+1} - V\Delta t\frac{D}{h^2}\left(\phi_{k-1}^{n+1} + \phi_{k+1}^{n+1}\right) = \phi_k^n + V\Delta t\sum_i \lambda_i C_{i,k}^{n+1} + V\Delta t Q_k^{n+1} \\ &C_{i,k}^{n+1} = \frac{C_{i,k}^n + \beta_i \nu\Sigma_f \Delta t \phi_k^{n+1}}{(1+\lambda_i \Delta t)} \qquad \forall i \end{aligned} \quad . \tag{2.10}$$

Now fill in $C_{i,k}^{n+1}$ into the upper equation of (2.10) to find

$$\begin{aligned} &\left(1 + V\Delta t\left[\Sigma_a - (1-\beta)\nu\Sigma_f + 2\frac{D}{h^2} - \sum_i \frac{\lambda_i \beta_i \nu\Sigma_f \Delta t}{(1+\lambda_i \Delta t)}\right]\right)\phi_k^{n+1} - V\Delta t\frac{D}{h^2}\left(\phi_{k-1}^{n+1} + \phi_{k+1}^{n+1}\right) = \\ &\qquad \phi_k^n + V\Delta t\sum_i \frac{\lambda_i C_{i,k}^n}{1+\lambda_i \Delta t} + V\Delta t Q_k^{n+1} \end{aligned} \quad . \tag{2.11}$$

This equation can also be written in matrix form

$$\mathbf{B}\underline{\phi}^{n+1} = \underline{\phi}^n + V\Delta t\left(\sum_i \frac{\lambda_i \underline{C}_i^n}{1+\lambda_i \Delta t} + \underline{Q}^{n+1}\right), \tag{2.12}$$

where the diagonal elements b_{kk} of $\mathbf{B}$ are given by

$$b_{kk} = 1 + V\Delta t\left[\Sigma_a - (1-\beta)\nu\Sigma_f + 2\frac{D}{h^2} - \sum_i \frac{\lambda_i \beta_i \nu\Sigma_f \Delta t}{1+\lambda_i \Delta t}\right]$$

and **B** is then given by

$$\mathbf{B}=\begin{bmatrix} 1 & 0 & 0 & 0 & 0 & 0 \\ -V\Delta t\frac{D}{h^2} & b_{kk} & -V\Delta t\frac{D}{h^2} & 0 & 0 & 0 \\ 0 & -V\Delta t\frac{D}{h^2} & b_{kk} & -V\Delta t\frac{D}{h^2} & 0 & 0 \\ 0 & 0 & -V\Delta t\frac{D}{h^2} & \ddots & \ddots & \vdots \\ 0 & 0 & 0 & \ddots & b_{kk} & -V\Delta t\frac{D}{h^2} \\ 0 & 0 & 0 & \cdots & 0 & 1 \end{bmatrix}.$$

Note that it might be necessary to use another value than 1 in the first and last coefficient on the diagonal to ensure numerical stability. The matrix **B** might otherwise become ill-conditioned since the other values in the matrix are of another order of magnitude. The matrix-vector equation can be solved easily by MATLAB and the resulting vector $\underline{\phi}^{n+1}$ is used to compute $\underline{C}_i^{n+1}$

$$\underline{C}_i^{n+1}=\frac{\underline{C}_i^n+\beta_i\nu\Sigma_f\Delta t\underline{\phi}^{n+1}}{\left(1+\lambda_i\Delta t\right)}. \tag{2.13}$$

This procedure is repeated for each time step.

There are two basic time-dependent scenarios for this problem. In the first the solution of the steady state equations ($\underline{\phi}^1=\underline{\phi}_{steady-state}$) is used as an initial condition combined with a shutdown of the source: $\underline{Q}^{(n>1)}=\underline{0}$. The second scenario starts with zero flux ($\underline{\phi}^1=\underline{0}$) and the source is turned on: $\underline{Q}^{(n>1)}=\underline{q}$.

2.2.5 Shutdown of the slab reactor

For the scenario of a shutdown of the source ($\underline{\phi}^1=\underline{\phi}_{steady-state}$ and $\underline{Q}^{(n>1)}=\underline{0}$) the time-dependent neutron flux was calculated for different values of k_{eff}, ranging from 0.9 to 0.997. The ratio between the instantaneous power production in the reactor and the steady-state power ($\frac{P(t)}{P_s}=\frac{\int_{x=-50}^{+50}\phi(x,t)\,dx}{\int_{x=-50}^{x=50}\phi_{steady-state}(x)\,dx}$) has been plotted as a function of time. The spatial integration was performed with a simple middle Riemann sum, characterized by $\int_x f(x)\,dx=\sum_{i=1}^{n_x}\frac{f(x_{i+1})+f(x_i)}{2}\Delta x$.

The time is given on a logarithmic scale to be able to capture the important events of the prompt neutrons and the delayed neutrons in one graph. To capture the time scales of both the prompt and the delayed neutrons Δt was increased after each time step of the calculation. As a consequence smaller steps were made in the prompt regime and larger steps in the delayed regime.

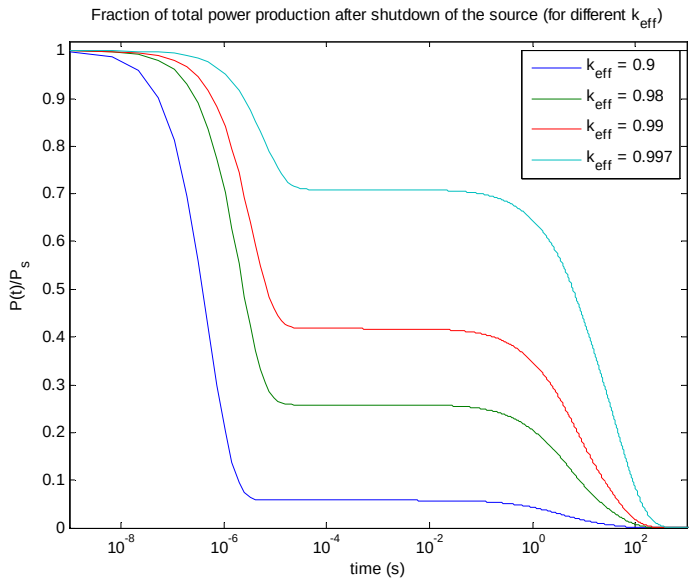

Figure 2.3 Fraction of steady-state power production after source shutdown for different k_{eff}

After the shutdown of the source the neutron flux will rapidly decrease. After a couple of microseconds (3~30 μs) the neutron flux in the system is almost stable. After 20 ms the neutron flux slowly starts to decrease again due to precursor decay. The largest decrease takes place on the timescale of seconds. On short time scales ($<1\,ms$) the decay of precursors can be treated as a constant background in the neutron flux. From the plot it also becomes clear that the delayed neutrons play a much larger role when k_{eff} approaches criticality. A similar relationship of reducing importance of delayed neutrons as subcriticality increases was also discovered by Ravetto [2000] and Saracco & Ricco [2009].

2.2.6 Start-up of the slab reactor

Also for the start-up of the reactor ($\underline{\phi}^1 = \underline{0}$ and $\underline{Q}^{n>1} = \underline{q}$) the fraction of the total power production as a function of time has been plotted in Figure 2.4. In this case a similar observation as with the shutdown of the source can be made: the delayed neutrons play a greater role as k_{eff} approaches criticality.

The prompt neutrons are responsible for a steep rise of the neutron flux in the first few μs after the source is switched on. Then the neutron flux remains at a stable level until the concentration of the precursors has built up significantly and the resulting delayed neutrons start contributing to the total neutron flux. In the end the neutron flux becomes equal to the flux of the steady-state problem.

In this case it can be noted again that the transient behaviour of the system during the early stages ($<1\,ms$) can be analysed by considering only the prompt neutrons. Since the initial flux and initial precursor concentrations are zero there is also no background due to the delayed neutrons.

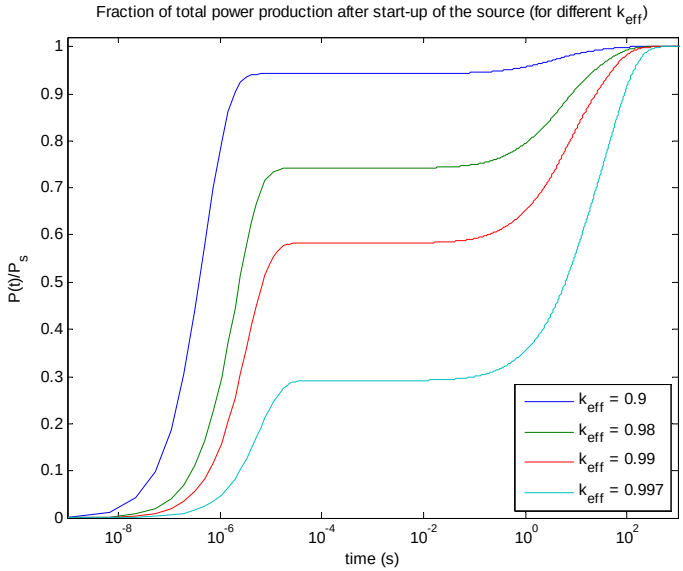

Figure 2.4 **Fraction of steady-state power production after source startup for different k_{eff}**

2.2.7 Conclusions

In section 2.1 about ADS literature three important characteristics of the transient behaviour of an ADS were mentioned. First of all the source dominates the neutron flux shape for highly subcritical systems. Secondly the prompt neutrons act on a very fast time scale and the delayed neutrons on a much slower time scale. Thirdly the weight of delayed neutrons in the total power production is significantly reduced as subcriticality of a system increases. These three characteristics encountered in literature were also discovered in the results of the relatively simple 1D-diffusion model.

This study also shows that the delayed neutrons can be considered as a constant background during a transient on a short-time scale (< 1 *ms*). Since the transients in the remainder of this thesis are only studied upon short time scales it seems reasonable to neglect the delayed neutrons during the transient calculations in this thesis. For highly subcritical systems the reduced weight of the delayed neutrons in the total power production can be considered as an additional justification to neglect the delayed neutrons. The reduced weight of the delayed neutrons can be an important issue with respect to the safety of an ADS during a transient.

3 Fixed source and mode calculations with PHANTOM

3.1 The neutron transport equation

The central problem in nuclear reactor theory is the determination of the distribution of the neutrons in the reactor. The neutron distribution determines the rate at which various nuclear reactions occur. In order to predict for instance the power production of a nuclear reactor the neutron flux must be calculated. The neutron flux, $\psi\left(\vec{r},E,\hat{\Omega},t\right)$, in a nuclear reactor is described by the neutron transport equation

$$\begin{aligned}\frac{1}{V}\frac{\partial\psi\left(\vec{r},E,\hat{\Omega},t\right)}{\partial t} &= -\hat{\Omega}\cdot\nabla\psi\left(\vec{r},E,\hat{\Omega},t\right)-\Sigma_t\left(\vec{r},E,t\right)\psi\left(\vec{r},E,\hat{\Omega},t\right)\\ &+\int_{4\pi}\int_{0}^{\infty}\Sigma_s\left(\vec{r},E'\to E,\hat{\Omega}'\to\hat{\Omega},t\right)\psi\left(\vec{r},E',\hat{\Omega}',t\right)dE'd\hat{\Omega}' \\ &+\frac{\chi(E)}{4\pi}\int_{4\pi}\int_{0}^{\infty}\nu\Sigma_f\left(\vec{r},E',t\right)\psi\left(\vec{r},E',\hat{\Omega}',t\right)dE'd\hat{\Omega}'+Q\left(\vec{r},E,\hat{\Omega},t\right)\end{aligned}, \tag{3.1}$$

where V represents the neutron speed, Σ_t the macroscopic total cross section $\left[cm^{-1}\right]$, Σ_s the scattering cross section, Σ_f the fission cross section, $\chi(E)$ the fission spectrum, ν the average number of neutrons released per fission and $Q\left(\vec{r},E,\hat{\Omega},t\right)$ the external source.

The transport equation can also be written in a shorter notation

$$\frac{1}{V}\frac{\partial\psi}{\partial t}=\left[\mathbf{F}-\mathbf{L}\right]\psi+Q. \tag{3.2}$$

The transport operator **L** contains the effects of neutron leakage, neutron collisions and the contribution of neutrons scattered into $d\hat{\Omega}dE$. The operator **F** describes the fission process. The notation of eq. (3.2) is used most throughout this thesis.

If the appropriate cross sections are used the neutron transport equation provides an essentially exact description of the neutron distribution within the reactor. The angular neutron flux $\psi\left(\vec{r},E,\hat{\Omega},t\right)$ contains all essential information about the neutronics of a nuclear reactor. In general the transport equation is difficult to solve since the neutron flux depends on space, angle, energy and time. Direct numerical methods to solve the transport equation are often computationally expensive, especially when delayed neutrons are included in time-dependent problems. In practice often simplified models are used. An extensive treatment of possible computational methods to solve the neutron transport problem was already given in section 2.1.3. During the thesis the transport equation was also solved by means of direct methods to obtain reference solutions to check the accuracy of the modal expansion methods.

3.2 Basic principles of PHANTOM

During the thesis the PHANTOM code package is used to solve the neutron transport equation. PHANTOM is an unstructured finite element neutron transport tool that can be used to solve fixed source problems, perform time-dependent calculations and to calculate α-modes or λ-modes.

In this section the least squares functional used by PHANTOM is introduced and the discretization of the space, angle and energy variables used in PHANTOM is treated. The same discretizations will also be used in the modal expansion methods in chapter 5 and 6.

3.2.1 First order least squares system

PHANTOM uses a least squares approach to discretize the neutron transport equation. Lathouwers [2007] gives a detailed treatment of the least squares approach. Here a short description will be sufficient. The one group neutron transport equation can be written as

$$\Omega \cdot \nabla \psi \left(\vec{r}, \hat{\Omega} \right) + M\psi \left(\vec{r}, \hat{\Omega} \right) = S\left(\vec{r}, \hat{\Omega} \right), \tag{3.3}$$

where the operator M accounts for scattering and removal and the source $S\left(\vec{r}, \hat{\Omega} \right)$ includes both the fission source and the external source. Vacuum boundary conditions are assumed, so at the boundary $\psi \left(\vec{r}, \hat{\Omega} \right) = 0$ for all inward directions ($\hat{\Omega} \cdot \hat{n} < 0$). The one group transport equation (3.3) can simply be written as

$$L\psi = S\,. \tag{3.4}$$

To obtain the neutron flux PHANTOM minimizes a least squares functional

$$R\left[\psi \right] = \left\langle L\psi - S, L\psi - S \right\rangle + 2\int_{\partial V} \int_{\hat{\Omega} \cdot \hat{n} < 0} d\partial V d\Omega \left| \hat{\Omega} \cdot \hat{n} \right| \psi^2\,. \tag{3.5}$$

The least squares approach can be extended to describe multi-group transport. PHANTOM then solves the least-squares function in an inner iteration loop for each energy group and the multi-group problem is solved in an outer iteration loop by means of a block Gauss-Seidel procedure. This block Gauss-Seidel procedure is briefly described in section 3.3.1.

3.2.2 Spherical harmonics expansion of the angular dependence

In order to solve the neutron transport equation the angle, energy and spatial variables must be discretized in some fashion. PHANTOM treats the angular dependence of the neutron flux by expanding the flux in terms of spherical harmonics. Any function $f\left(\vec{r}, \hat{\Omega} \right)$ can be written as an infinite expansion in terms of spherical harmonics

$$f\left(\vec{r}, \hat{\Omega} \right) = \sum_{l=0}^{\infty} \sum_{m=-l}^{l} f_{l,m}\left(\vec{r} \right) Y_{l,m}\left(\hat{\Omega} \right). \tag{3.6}$$

In practice the function $f\left(\vec{r}, \hat{\Omega} \right)$ will be approximated by truncating the series after $l = N$. This approximation is called the P_N -expansion. An overview of the (real) Y_{lm} -functions used by PHANTOM and their orthonormality relations can be found in appendix A.

For convenience the indices *l* and *m* can also be ordered into one vector, with index *i* describing all the spherical harmonics functions. Doing so the spherical harmonics expansion of the function $f\left(\vec{r}, \hat{\Omega} \right)$ becomes

$$f\left(\vec{r}, \hat{\Omega} \right) = \sum_{i=1}^{M} f_i\left(\vec{r} \right) Q_i\left(\hat{\Omega} \right). \tag{3.7}$$

This expansion can conveniently be written in vector notation

$$f\left(\vec{r}, \hat{\Omega} \right) = \mathbf{Q}^T\left(\hat{\Omega} \right) \mathbf{f}\left(\vec{r} \right) = \mathbf{f}^T\left(\vec{r} \right) \mathbf{Q}\left(\hat{\Omega} \right) \tag{3.8}$$

where the vector $\mathbf{Q}\left(\hat{\Omega}\right)$ contains the set of all spherical harmonics polynomials used in the expansion. The orthonormality relation is given by

$$\int_{4\pi} Q_i\left(\Omega\right) Q_j\left(\Omega\right) d\Omega = \delta_{i,j} \tag{3.9}$$

or in vector notation $\int_{4\pi} \mathbf{Q}\left(\Omega\right)\mathbf{Q}^T\left(\Omega\right) d\Omega = \mathbf{I}$. This orthonormality relation of the spherical harmonics will be useful in the alpha mode expansion theory.

3.2.3 Spatial finite elements

The neutron flux is to be determined by means of minimizing the functional $R\left[\psi\right]$ defined by eq. (3.5). The neutron flux can be expressed as a linear combination of previously chosen basis functions. The finite element method (FEM) originates from a clever choice of these basis functions. The FEM is well suited for unstructured grids and has a strict local character. All information on one element is used, without considering neighbors, making the method very attractive for computer implementation. Van Kan [2005] gives an introduction of the basics of the Finite Element Method.

The spatial dependence of the function $f_{l,m}$ can be written as a linear combination of basis functions

$$f_{l,m}\left(\vec{r}\right) = \sum_{n=1}^{N} f_{l,m}^{n} h_n\left(\vec{r}\right) \tag{3.10}$$

where N represents the number of nodes defining the FEM grid, $f_{l,m}^{n}$ is the value of the function $f_{l,m}$ at the node n and $h_n\left(\vec{r}\right)$ are the basis functions corresponding to the node n. In one dimension the basis functions can be represented by the so-called tent functions. An example of these tent functions and how they can reconstruct an original function is shown in Figure 3.1. The spatial interval is divided into 5 linear elements and as a consequence 6 nodes.

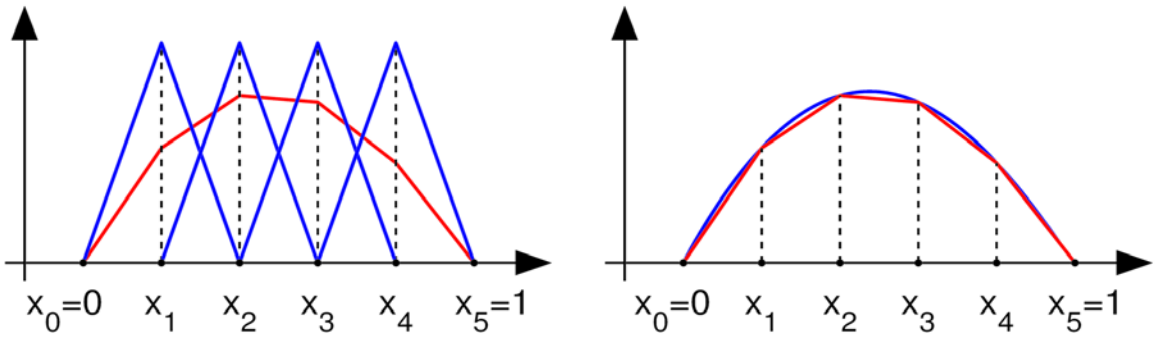

Figure 3.1 1D linear basis functions and example of reconstruction of original function

The linear basis functions $h_n\left(x\right)$ are defined as

$$h_n\left(x\right) = \begin{cases} 0 & x < x_{n-1} \\ \dfrac{x - x_{n-1}}{x_n - x_{n-1}} & x_{n-1} \le x < x_n \\ \dfrac{x_{n+1} - x}{x_{n+1} - x_n} & x_n \le x < x_{n+1} \\ 0 & x > x_{n+1} \end{cases} . \tag{3.11}$$

Another possibility is the use of elements with quadratic interpolation polynomials, simply called quadratic elements. Solving problems in terms of quadratic elements is more expensive, but also leads to very accurate results. In general the use of quadratic elements of a larger dimension can improve the accuracy of the calculation, without significantly increasing the computational time. During the thesis the maximum size of the elements is prescribed by the geometry of the system under consideration. Because of this only elements of a limited size could be used making quadratic elements too expensive for most of the calculations during this thesis. So, unless stated otherwise, the reader may assume that linear elements were used throughout the thesis.

The part of the basis functions $h_n(x)$ that runs over the element e can be defined as $h_n^e(x)$. In one dimension these can be recognised as 'half' tent functions. Using these half tent function the reconstruction of $f_{l,m}$ in terms of the FEM basis functions can also be performed by summing element-wise over the nodes belonging to the elements and finally sum over all elements

$$f_{l,m}(x) = \sum_{n=1}^{N} f_{l,m}^n h_n(x) = \sum_{e=1}^{E} \sum_{n=1}^{n_e} f_{l,m}^n h_n^e(x), \tag{3.12}$$

where E is the total number of elements and n_e is the number of nodes belonging to an element. PHANTOM performs the FEM-discretization in this way. It is very convenient for programming since a code just has to sum contributions from separate elements. It also shows the local character of the FEM: only the nodes belonging to the element e give a non-zero contribution in the summation. The FEM-discretization of the neutron flux can be extended towards two- and three-dimensional cases in a similar manner. In 2D the most common elements are the triangle and the quadrilateral.

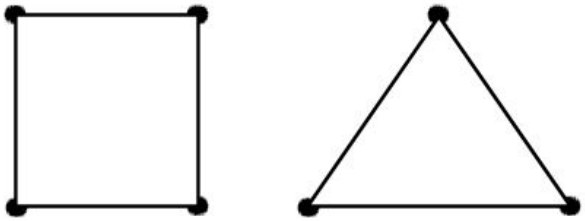

Figure 3.2 The 4-node quadrilateral and 3-node triangular element

The linear triangular element comprises 3 nodes and the linear quadrilateral element 4 nodes. The quadratic triangular element comprises 6 nodes and the quadratic quadrilateral comprises 8 nodes (incomplete) or 9 nodes (complete). In 3D the most used elements are the tetrahedron and the hexahedron depicted in Figure 3.3.

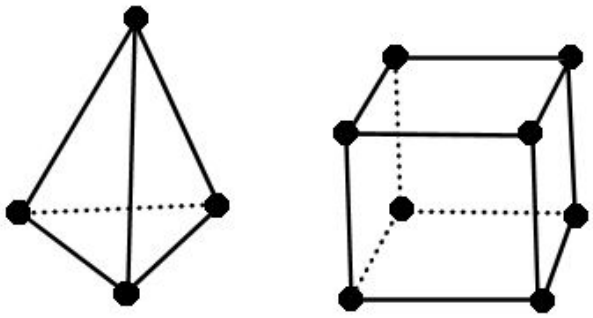

Figure 3.3 The 4-node tetrahedral and 8-node hexahedral element

The linear tetrahedron consists of 4 nodes and the linear hexahedron of 8 nodes. Basis functions for the 4-node quadrilateral are given by Van Kan [2005]. Some basis functions of other elements are given by Zienkiewicz & Taylor [2000].

One can see from shapes of the 2D and 3D-elements that the FEM allows for unstructured grids to be built. Unstructured grids are very convenient for representing complex geometries. During the calculations of the thesis structured grids were used, so the 2-node linear 1-dimensional element, the 4-node quadrilateral and the 8-node hexahedron are the most frequently used elements throughout the thesis.

For the determination of the least-squares functional, given by eq. (3.5), integrals such as $\int_{V_e} h_i^e(\vec{r}) h_j^e(\vec{r}) dV$, $\int_{V_e} \nabla h_i^e(\vec{r}) \cdot \nabla h_j^e(\vec{r}) dV$ and $\int_{V_e} f h_i^e(\vec{r}) dV$ must be evaluated. The calculation of those integrals is performed by means of quadrature. The quadrature rules are defined upon a reference line, surface or cube V_R with spatial coordinate(s) ranging from -1 to 1 in all one, two or three dimensions. The quadrature rules are defined as

$$\int_{V_e} f(\vec{s}) d\vec{s} = \sum_i w_i f(\vec{s}_i), \tag{3.13}$$

where w_i is are the quadrature weights and $\vec{s}_i$ the coordinates of the quadrature points. PHANTOM uses the 2-point quadrature rules for the integration over linear elements. In that case the weights are equal to 1 in 1, 2 or 3 dimensions and the quadrature points are given by $\left(\pm\sqrt{1/3}\right)$, $\left(\pm\sqrt{1/3}, \pm\sqrt{1/3}\right)$ and $\left(\pm\sqrt{1/3}, \pm\sqrt{1/3}, \pm\sqrt{1/3}\right)$ respectively. The 2-point quadrature rules yield an exact result for polynomials of degree 3 or less.

For the calculation of integrals over other volumes than the reference volume a mapping must be made. The quadrature rule is then given by

$$\int_V f(\vec{r}) d\vec{r} = \int_{V_R} f_R(\vec{s}) \left|\det(\mathbf{J})\right| d\vec{s} = \sum_{i=1}^{n} w_i \left|\det(\mathbf{J})\right|_i f_R(\vec{s}_i), \tag{3.14}$$

where $f_R(\vec{s})$ follows from mapping $f(\vec{r})$ upon the reference volume. The mapping can be defined as $f(\vec{r}) \xrightarrow{\vec{r}=\vec{r}(\vec{s})} f_R(\vec{s})$. $\mathbf{J}$ is the Jacobian of the coordinate transformation, which should also be sampled upon each quadrature point. More details about quadrature and the mapping can be found in Zienkiewicz & Taylor [2000] or Gockenbach [2006].

3.2.4 Multi-group transport

PHANTOM handles the energy dependence of the neutron flux by dividing the neutron flux into group fluxes corresponding to several energy groups. The multi-group discretization is well-known from reactor physics. A comprehensive treatment of multi-group theory can therefore be found in standard reactor physics literature. [Bell & Glasstone, 1985; Duderstadt & Hamilton, 1976].

Since neutrons usually lose energy during their lifetime a backward indexing scheme is used for the numbering of the energy groups. As a result the lowest energy group corresponds to the group with the highest energies of the neutrons. This is schematically shown in Figure 3.4.

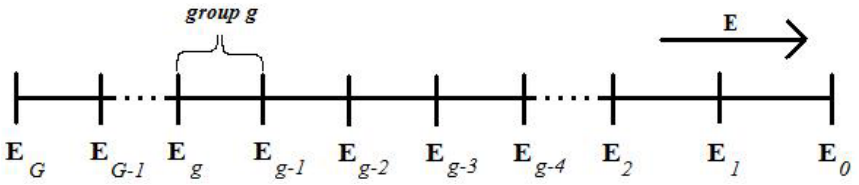

Figure 3.4 Discretization scheme of the continuous energy variable over the energy groups

In multi-group theory the neutron group flux is defined as

$$\psi_g\left(\vec{r},\hat{\Omega},t\right)=\int_{E_g}^{E_{g-1}}\psi\left(\vec{r},E,\hat{\Omega},t\right)dE \tag{3.15}$$

and the flux-weighted neutron speed of group g is given by

$$\frac{1}{V_g}=\frac{1}{\psi_g\left(\vec{r},\hat{\Omega},t\right)}\int_{E_g}^{E_{g-1}}\frac{1}{V}\psi\left(\vec{r},E,\hat{\Omega},t\right)dE\,. \tag{3.16}$$

The multi-group discretization of the adjoint flux is performed in a similar way.

3.3 Fixed source and time-dependent problems

Some aspects of solving fixed source problems and time-dependent problems with PHANTOM are treated in this section. Two simple test cases will show that PHANTOM can solve time-dependent problems in an accurate way.

3.3.1 The steady-state fixed source problem

If the time dependent term of eq. (3.2) is equal to zero a steady state fixed source problem is obtained

$$\left[\mathbf{L}-\mathbf{F}\right]\underline{\psi}=\underline{Q}_0\,. \tag{3.17}$$

Such steady state fixed source problems are solved in PHANTOM by means of the block Gauss-Seidel method for the energy groups. To solve eq. (3.17) an initial guess of the flux is chosen for $n=0$ and the flux is solved iteratively until the final solution fulfils the convergence criteria of the block Gauss-Seidel procedure. In case of a multi-group problem the block Gauss-Seidel procedure consists of an outer and an inner iteration loop. The outer iteration loop is terminated when the distribution of the neutron flux over the groups has converged. Inside the inner iteration loop the least-squares functional, given by eq. (3.5) is determined for all energy groups. Exact details of how the group fluxes themselves are calculated are not so relevant for the aims of this thesis and are therefore omitted. More information about the block Gauss-Seidel procedure can be found in Greenbaum [1997].

3.3.2 Time-dependent calculations

Starting from the time-dependent neutron transport equation

$$\frac{1}{V}\frac{\partial\psi}{\partial t}+\left[\mathbf{L}-\mathbf{F}\right]\psi=Q\,, \tag{3.18}$$

an Euler implicit scheme is used to discretize the time dependence in the equation

$$\frac{\underline{\psi}^{i+1}-\underline{\psi}^{i}}{V\Delta t}+\left[\mathbf{L}-\mathbf{F}\right]\underline{\psi}^{i+1}=\underline{Q}^{i+1}\,. \tag{3.19}$$

After rewriting

$$\left[\mathbf{L}-\mathbf{F}+\frac{\mathbf{I}}{V\Delta t}\right]\underline{\psi}^{i+1}=\underline{Q}^{i+1}+\frac{\underline{\psi}^{i}}{V\Delta t}\,, \tag{3.20}$$

the time-absorption term $\frac{\mathbf{I}}{V\Delta t}$ on the left hand side of the equation can be implemented into the transport operator $\mathbf{L}^* = \mathbf{L} + \frac{\mathbf{I}}{V\Delta t}$. In practice this time-absorption term can be added to the total macroscopic cross section Σ_t. After doing so a fixed source problem is obtained

$$\left[\mathbf{L}^* - \mathbf{F}\right]\underline{\underline{\psi}}^{i+1} = \underline{\underline{Q}}^{i+1} + \frac{\underline{\underline{\psi}}^{i}}{V\Delta t}, \tag{3.21}$$

where in the formulation of eq. (3.17) the fixed source is given by $\underline{\underline{Q}}_0 = \underline{\underline{Q}}^{i+1} + \frac{\underline{\underline{\psi}}^{i}}{V\Delta t}$. This fixed source problem can now be solved for each time step by the Gauss-Seidel method described in the previous subsection.

An important advantage of the implicit Euler scheme is that, in contrast to an explicit Euler scheme, it is numerically stable for each step size Δt. But one should realize that the implicit Euler scheme is only a first order approximation of the time-derivative. As a consequence sufficiently small time-steps should be used to obtain accurate results for the time integration.

Using a smaller time-step size Δt in eq. (3.21) makes the problem easier to solve. Using a smaller time-step the $\frac{\mathbf{I}}{V\Delta t}$ will become larger and $\mathbf{L}^* - \mathbf{F}$ becomes more diagonally dominant. This leads to a faster convergence of the calculation. So a reduction of the time-step with a factor two does not automatically lead to an increase of the computational time by a factor two.

Since PHANTOM has not been used very often for time-dependent calculations several simple test cases are used to check if PHANTOM produces accurate solutions. Time-dependent results from PHANTOM must be correct, since they will be used as reference solutions to verify the results of the modal expansion methods developed later in this thesis.

3.3.3 Test case 1: Time-dependent calculations in an infinite system

The first test case is that of an infinite homogeneous system with prompt neutrons only and one energy group. For such a system the evolution of the neutron population over time is described by

$$\frac{d\phi}{dt} = V\left[P(t) - L(t)\right] = V\left(k-1\right)L(t), \tag{3.22}$$

where $P(t)$ is the production rate and $L(t)$ the loss rate. For an infinite system $k = k_\infty$ and $L(t) = \frac{\phi(t)}{l_\infty V}$. As a consequence eq. (3.22) reduces to

$$\frac{d\phi}{dt} = \frac{\left(k_\infty - 1\right)}{l_\infty}\phi(t). \tag{3.23}$$

With the initial condition $\phi(t) = \phi_0$ the following solution is found

$$\phi(t) = \phi_0 e^{\left[\left(\frac{k_\infty - 1}{l_\infty}\right)t\right]}. \tag{3.24}$$

The neutron flux is found to vary exponentially in time. Further it is known that $l_\infty = \frac{1}{V\Sigma_a}$ and $k_\infty = \frac{\nu\Sigma_f}{\Sigma_a}$.

Calculations were performed with PHANTOM for a 1-dimensional homogeneous slab reactor with reflective boundary conditions. This is physically equivalent to an infinite system due to the reflective boundary conditions. The slab is divided into 100 first order elements ranging from x = -50 *cm* to x = +50 *cm*. The neutron speed is set to be 1 *cm/s*, Σ_a is 1 cm^{-1} and there is no scattering. For $\nu\Sigma_f$ four different values between 0.98 cm^{-1} and 1.02 cm^{-1} were used. A value of 1 was chosen for $\phi(0)$ and 50 time-steps of one second each were taken. The exact analytical solutions and the ones found by PHANTOM for different values of k_{eff} are plotted in Figure 3.5.

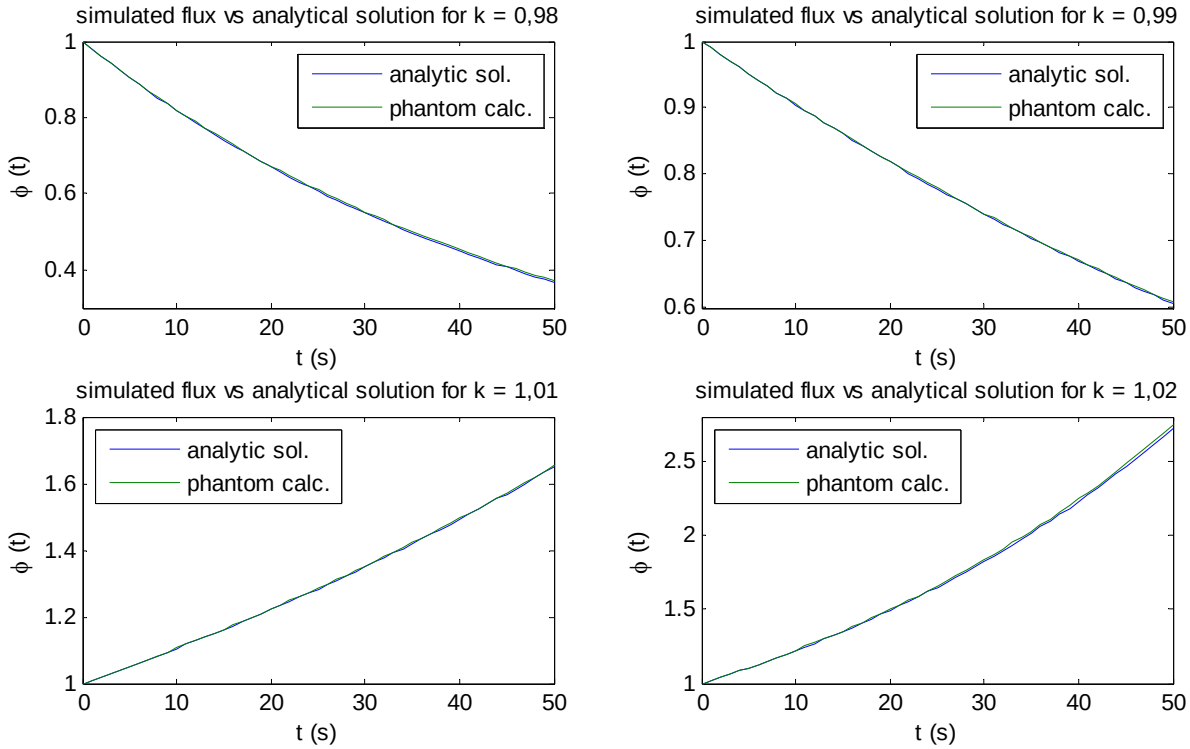

Figure 3.5 Time-dependent flux (PHANTOM vs analytical) for a reflective slab for different k_{eff}

The solution calculated by PHANTOM obviously corresponds very well to the exact solution. In order to check the influence of the magnitude of time-step Δt used in the PHANTOM calculation the time-dependent calculation for $k_{eff} = 0.98$ was also performed for different sizes of the time step Δt. The results are plotted in Figure 3.6.

The size of the time step Δt apparently has a significant influence upon the accuracy of the final result due to the implicit Euler time-integration scheme of PHANTOM. The use of a large time step can lead to significant errors at the end of the time domain of the calculation. Using 50 smaller time steps (1 *s*) an error of less than 1% compared to the analytical solution of the flux at *t* = 50 *s* was obtained. If the time-dependent PHANTOM-calculations are used as a reference solution it is important to use small time-steps, since the error in the reference solution may only be small. The next step is to check the results of time-dependent calculations for a more complex system.

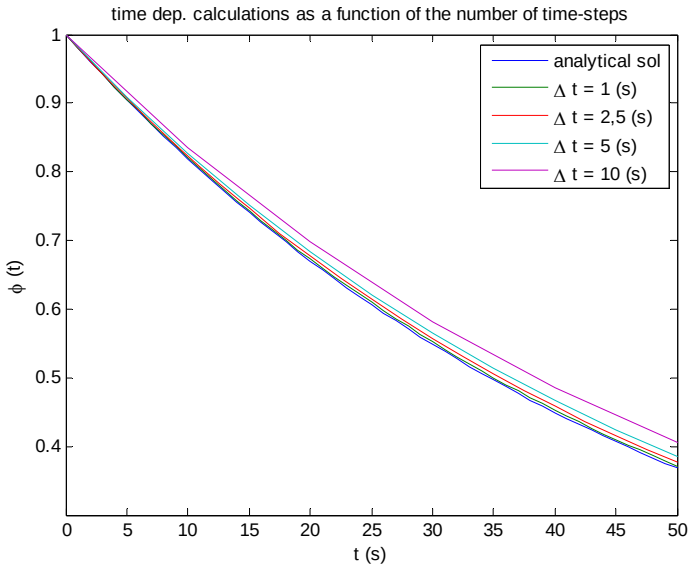

Figure 3.6 Time-dependent flux by PHANTOM for different time step Δt (k_{eff}= 0.98)

3.3.4 Test case 2: Time-dependent calculations for a bare slab geometry

For the second test case a similar slab reactor as in the previous test case is used. This time vacuum boundary conditions are used making it harder to predict the outcome of the calculation. However in a weakly absorbing medium with isotropic scattering and considering one energy group it is valid to use the one-speed diffusion approximation. According to eq. (5-198) of Duderstadt & Hamilton [1976] the neutron flux is given for such a system by

$$\phi(x,t) = \sum_{n_{odd}} A_n e^{\alpha_n t} \cos\left(\frac{n\pi x}{\tilde{a}}\right), \tag{3.25}$$

with

$$\alpha_n = V\nu\Sigma_f - V\Sigma_a - VD\left(\frac{n\pi}{\tilde{a}}\right)^2 \text{ for } n = 1,3,5,\ldots. \tag{3.26}$$

One might recognise these α_n as the time-eigenvalues or α-eigenvalues of the system. The values of the coefficients A_n depend on the shape of the initial flux $\phi(0,t)$. In case of isotropic scattering the diffusion coefficient is given by $D = \frac{1}{3\Sigma_t}$ and the extrapolation distance must be taken into account

$$\frac{\tilde{a}}{2} = \frac{L}{2} + \frac{0.7104}{\Sigma_t}. \tag{3.27}$$

The neutron speed is set at 1 *cm/s*, Σ_a is 0.2 cm^{-1}, Σ_s is 0.8 cm^{-1} and $\nu\Sigma_f$ is 0.22 cm^{-1}. Obviously scattering is much more important than absorption. This is necessary to allow for the diffusion approximation to be used. For this system with scattering and neutron leakage the PHANTOM calculation gave a value of 1.0982 for k_{eff}. Including the extrapolated distance the buckling becomes $B_1 = \left(\frac{\pi}{\tilde{a}}\right)$. Now using eq. (2.3), also a value of 1.0982 is found for k_{eff}. Time dependent calculations were performed for two initial fluxes, characterized by

$$\phi_1(x,0) = \cos\left(\frac{\pi x}{\tilde{a}}\right) \tag{3.28}$$

and

$$\phi_2(x,0) = \cos\left(\frac{\pi x}{\tilde{a}}\right) + \frac{1}{3}\cos\left(\frac{3\pi x}{\tilde{a}}\right) + \frac{1}{5}\cos\left(\frac{5\pi x}{\tilde{a}}\right). \tag{3.29}$$

In terms of the coefficients A_n of eq. (3.25) the first initial condition is described by $A_1 = 1$ and the other coefficients are zero, while the second initial condition is described by $A_1 = 1$, $A_3 = 1/3$, $A_5 = 1/5$ and the other coefficients are zero.

The progress of the flux in time at x = 0 *cm* and the solution at t = 50 *s* are plotted in Figure 3.7 if eq. (3.28) is used as the initial flux. Results were also plotted in Figure 3.8 when eq. (3.29) was used as the initial flux.

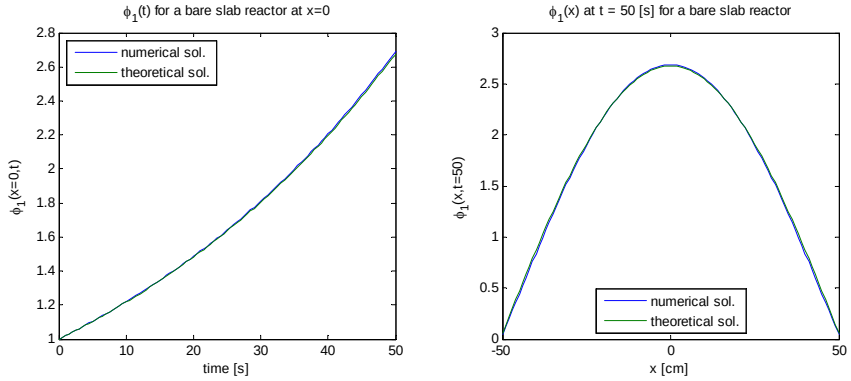

Figure 3.7 Flux as a function of time (*x*=0) and position (*t*=50 *s*) for the first initial condition

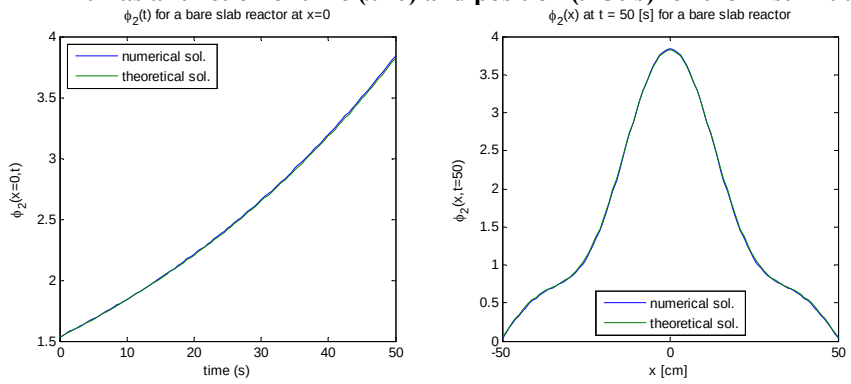

Figure 3.8 Flux as a function of time (*x*=0) and position (*t*=50 *s*) for the second initial condition

It is clear that the results for the time-dependent calculation obtained by PHANTOM agree very well with the theoretical solution. Also after a larger number of time-steps the solutions still correspond well.

After performing two simple time-dependent test cases a short recapitulation can be made. Time dependent calculations were performed with PHANTOM for a reflective slab reactor and a bare slab reactor. The result of the reflective slab reactor was compared with the analytical solution and the result of the bare slab reactor was compared with an analytical expression obtained by the diffusion approximation. For both the reflective and the bare slab reactor the calculations in PHANTOM show similar results as the analytical expressions. As a result it can be concluded that time dependent calculations in PHANTOM lead to correct results. This is important since PHANTOM will be used to create reference transient solutions to check the correctness of the time-dependent alpha mode expansion, treated in chapter 5.

3.4 Solving the alpha eigenvalue problem

3.4.1 The alpha eigenvalue equation

The so called alpha modes can be used as a basis for modal expansion techniques to describe the time-dependent neutron flux without performing a full transport calculation. The alpha modes are determined by solving the alpha eigenvalue problem, which will be derived from the transport equation. Only prompt neutrons are taken into account and the external source is neglected in eq. (3.2). The neutron flux is assumed to vary exponentially in time

$$\psi\left(\vec{r},E,\hat{\Omega},t\right)=\psi\left(\vec{r},E,\hat{\Omega}\right)e^{\alpha t}. \tag{3.30}$$

If this expression is plugged into eq. (3.2) the alpha eigenvalue problem is obtained

$$\frac{\alpha}{V}\psi_{\alpha}=\left[\mathbf{F}-\mathbf{L}\right]\psi_{\alpha}. \tag{3.31}$$

The eigenfunctions following from this problem are the alpha modes.

If the neutron flux in a (subcritical) system without a source has exactly the same shape as a certain alpha mode the neutron flux will decay exponentially over time with the alpha eigenvalue of the alpha mode as decay constant. This is the physical interpretation of the alpha modes.

One use of the alpha modes is found in the field of detector positioning in subcritical systems. It is important to continuously monitor the level of subcriticality of an ADS. The alpha modes can be a useful help to include effects of higher order harmonics into the problem of detector positioning in subcritical systems. The use of alpha modes for detector positioning has not been investigated during the thesis.

The main interest in the use of alpha modes during this thesis lies in the application of the modal expansion technique. The modal expansion technique is used to approximate the neutron flux for time-dependent problems without performing a full time-dependent transport calculation. The alpha modes will be used as a basis for the modal expansion technique in chapter 5.

For the modal expansion method in chapter 5 also the adjoint alpha modes will be required. The adjoint alpha modes are determined by solving the adjoint alpha eigenvalue problem, which is defined as

$$\frac{\alpha^{\dagger}}{V}\psi_{\alpha}^{\dagger}=\left[\mathbf{F}-\mathbf{L}\right]^{\dagger}\psi_{\alpha}^{\dagger}. \tag{3.32}$$

In the alpha mode expansion technique developed in chapter 5 the adjoint alpha eigenfunctions are used as a weighting function. The eigenfunctions $\psi_{\alpha}^{\dagger}$ are a measure of the importance of a neutron in establishing the contribution of a certain mode in the modal expansion of the neutron flux. A more extensive treatment of the adjoint neutron flux and adjoint operators is given by Williams [1988], Duderstadt & Hamilton [1976] or Bell & Glasstone [1985].

PHANTOM can determine the fundamental alpha mode numerically by the Power method. To obtain more dominant alpha modes the Implicitly Restarted Arnoldi Method is used.

3.4.2 The Power Method for alpha mode determination

The alpha eigenvalue problem can be solved for the fundamental eigenmode in PHANTOM by means of the Power method. A more mathematical treatment of the Power method can be found in Isaacson & Keller [1994].

A simple scheme of the power method for the calculation of the α -modes is the following:

Choose initial $\underline{\psi}_{old}$ with $\left\|\underline{\psi}_{old}\right\| = 1$

For $k = 1,\ldots..$ **do**

$$\left[\mathbf{L}-\mathbf{F}\right]\underline{\psi}_{new} = -\frac{\underline{\psi}_{old}}{V}$$

$$\alpha_0^{-1} = \underline{\psi}_{new} \cdot \underline{\psi}_{old}$$

$$\underline{\psi}_{new} = \frac{\underline{\psi}_{new}}{\left\|\underline{\psi}_{new}\right\|}$$

$$\underline{\psi}_{old} = \underline{\psi}_{new}$$

$$\underline{\psi}_{new} = \alpha_0^{-1}\underline{\psi}_{new}$$ this step gives a good initial guess for the next iteration

End

$$\alpha_0 = \frac{1}{\alpha_0^{-1}}$$

The calculation has converged when the relative change of α_0^{-1} and the relative change of the vector $\underline{\psi}$ between two iteration steps are smaller than user defined values. The rate of convergence of the power method depends on the dominance ratio of the eigenvalues. If the fundamental eigenvalue and the next dominant eigenvalue are close to each other the calculation will only converge slowly.

It is important to notice that the calculation of each single power iteration step is a fixed source calculation in itself (requiring several Gauss-Seidel iterations). For each power-iteration step eq. (3.17) is solved using $Q_0 = -\frac{\underline{\psi}^k}{V}$.

3.4.3 The Arnoldi Method for alpha mode determination

To obtain one or more dominant eigenmodes of the alpha eigenvalue problem PHANTOM uses the Implicitly Restarted Arnoldi Method (IRAM). A practical description of the Arnoldi method is found in Hogben [2007]. The IRAM has been implemented by means of the ARPACK package [Lehoucq et al., 1997]. The alpha eigenvalue equation can be written as a standard eigenvalue problem $\mathbf{A}\underline{x} = b\underline{x}$ by writing

$$-\frac{1}{V}\left[\mathbf{L}-\mathbf{F}\right]^{-1}\psi_\alpha = \alpha^{-1}\psi_\alpha\,, \tag{3.33}$$

so $\mathbf{A} = -\frac{1}{V}\left[\mathbf{L}-\mathbf{F}\right]^{-1}$ and $b = \alpha^{-1}$.

The standard eigenvalue problem can be solved using ARPACK and the eigenvalues α follow from a simple inversion of the dominant reciprocal eigenvalues α^{-1}. More details about the procedure are given by Lathouwers [2003]. The calculation of the alpha modes in both the Power and the Arnoldi method requires solving a fixed source problem making both methods inapplicable for calculating alpha modes of (super)critical systems. Singh [2009] proposed the addition of a shift to the left and right-hand side of the alpha eigenvalue equation to make the system artificially subcritical during the calculation. In this way the eigenvalues can also be calculated for supercritical systems by doing the inverse shift when the calculation has finished. ARPACK has an option to include such a shift in the

eigenvalue calculation. This method has not been tested during the thesis since accelerator driven systems ought to be subcritical anyway.

3.4.4 Test case 3: Fundamental alpha mode of an infinite homogeneous system

PHANTOM has not been used often to calculate alpha modes. An accurate determination of the alpha modes is a necessity for a successful realisation of the alpha mode expansion method. The best way to check the correctness of the calculation of the alpha modes by PHANTOM is to compare the alpha eigenvalues with analytical solutions of simple problems. Three simple test cases to check the alpha mode computation are performed in the coming three subsections.

The neutron population of an infinite homogeneous system with prompt neutrons and one energy group is determined by eq. (3.24). The α-modes describe the neutron population by assuming $\phi(t) = \phi_0 e^{\alpha t}$. For an infinite system an analytical expression for α_0 is then given by

$$\alpha_0 = \frac{k_\infty - 1}{l_\infty} = (k_\infty - 1) V \Sigma_a = V\left(\nu\Sigma_f - \Sigma_a\right). \tag{3.34}$$

By choosing the velocity and cross sections in the PHANTOM calculation the value of α_0 can be determined exactly. The fundamental alpha eigenvalue has been determined with PHANTOM by the Arnoldi method and the power method for a 1D-system with reflective boundary conditions. The results are given in Table 3.1.

Table 3.1 Comparison of analytical and numerical fundamental α-eigenvalue for an infinite system

ν [cm/s]	Σ_a [cm^{-1}]	$\nu\Sigma_f$ [cm^{-1}]	$\alpha_{0,exact}$ [s^{-1}]	$\alpha_{0,arnoldi}$ [s^{-1}]	CPU-t [s]	$\alpha_{0,power}$ [s^{-1}]	CPU-t [s]
1	0.1	0.09	-0.01	-0.010000002	22.46	-0.010000008	1.53
100	1.0	0.98	-2	-2.000000410	404.17	-2.000114338	2.17
100	1.0	0.99	-1.0	-1.000322326	271.89	-1.000116002	2.52

PHANTOM can clearly calculate the alpha eigenvalues in a correct way for this very simple problem. For systems close to criticality the solution converges at a slower rate. The power method requires more power iterations. The Arnoldi method requires more fixed source calculations and more Gauss-Seidel iterations to solve the problem because of slower convergence. Both the Power method and the Arnoldi method give accurate results for the determination of the fundamental alpha eigenvalue. The accuracy can be improved further by choosing stricter convergence criteria. Since stricter criteria lead to an increasing number of iterations the computational cost of the calculation will also increase. It is obvious from Table 3.1 that the Power method is much faster than the Arnoldi method.

3.4.5 Test case 4: Alpha modes of a purely scattering homogeneous slab

Another slightly more complicated case to verify the calculation of the time-eigenvalues by PHANTOM is the case of a purely scattering homogenous slab. Dahl [1983] studied this case semi-analytically in 1983 and Lathouwers [2003] calculated the dominant time-eigenvalues with a similar 1D transport code.

In this case Σ_t and Σ_s were set to 1 cm^{-1} and the neutron speed was set at a value of 1 *cm/s*. Calculations were performed with PHANTOM for different thicknesses of the slab with a P_{15}-expansion in angle and a discretization in space of 200 linear elements. Now a comparison between the dimensionless time-eigenvalues ($\alpha / V\Sigma_s$) found by Dahl [1983] and the calculations in PHANTOM is made in Table 3.2.

Table 3.2 Numerical and analytical dimensionless time eigenvalues for a slab of varying thickness

d (*cm*)	Mode	P_{15}	Dahl et. al. (1983)
1	1st even	$-6.1613\cdot10^{-1}$	$-6.08072\cdot10^{-1}$
2	1st even	$-2.9739\cdot10^{-1}$	$-2.96738\cdot10^{-1}$
5	1st even	$-8.1139\cdot10^{-2}$	$-8.10933\cdot10^{-2}$
	1st odd	$-3.4149\cdot10^{-1}$	$-3.41216\cdot10^{-1}$
	2nd even	$-8.3959\cdot10^{-1}$ (*)	$-8.34837\cdot10^{-1}$
10	1st even	$-2.5357\cdot10^{-2}$	$-2.53520\cdot10^{-2}$
	1st odd	$-1.0301\cdot10^{-1}$	$-1.02978\cdot10^{-1}$
	2nd even	$-2.3806\cdot10^{-1}$	$-2.37942\cdot10^{-1}$
	2nd odd	$-4.4022\cdot10^{-1}$	$-4.39814\cdot10^{-1}$
15	1st even	$-1.2233\cdot10^{-2}$	$-1.22306\cdot10^{-2}$
	1st odd	$-4.9299\cdot10^{-2}$	$-4.92855\cdot10^{-2}$
	2nd even	$-1.1234\cdot10^{-1}$	$-1.12291\cdot10^{-1}$
	2nd odd	$-2.0340\cdot10^{-1}$	$-2.03251\cdot10^{-1}$
	3rd even	$-3.2563\cdot10^{-1}$	$-3.25261\cdot10^{-1}$
	3rd odd	$-4.8369\cdot10^{-1}$	$-4.82830\cdot10^{-1}$
	4th even	$-6.8622\cdot10^{-1}$	$-6.82265\cdot10^{-1}$
	4th odd	$-8.4408\cdot10^{-1}$ (*)	$-9.31260\cdot10^{-1}$

* These eigenvalues also have small imaginary components

The eigenvalues calculated by PHANTOM correspond quite well to the values found by Dahl [1983], especially for neutronically thick media, and the time-eigenvalues show a great similarity with the P_{15}-expansion calculated by Lathouwers [2003] with a similar transport code.

The time-eigenvalues calculated by PHANTOM have now been validated for two relatively simple examples with theoretical results. This is important because the time-eigenvalues found by PHANTOM must be reliable to obtain useful results from the alpha mode expansion.

3.4.6 Test case 5: Alpha modes of a diffusive bare slab reactor

Using a diffusion approximation the alpha eigenvalues in a bare slab reactor consisting of a weakly absorbing medium with a thickness of 100 *cm* considering isotropic scattering only and one energy group were given by eq. (3.26). The first 15 dominant forward and adjoint alpha eigenvalues were computed by PHANTOM using $\nu\Sigma_f = 0.196\ cm^{-1}$, $\Sigma_t = 1\ cm^{-1}$ and $\Sigma_s = 0.8\ cm^{-1}$. The diffusion approximation is valid in case of a weakly absorbing medium. For this reason the scattering cross section is large compared to the absorption cross section to ensure that the medium is weakly absorbing. $\nu\Sigma_f$ was chosen to be a bit smaller than Σ_a to obtain a slightly subcritical system. The eigenvalues obtained by PHANTOM are compared with the theoretical alpha eigenvalues of eq. (3.26) in Table 3.3.

First of all the forward and adjoint calculation agree very well with each other, except for the 15th eigenvalue. Apparently the Arnoldi method has skipped one eigenvalue in the forward calculation. As the mode number *n* increases the deviation of the time-eigenvalues by PHANTOM and the analytical values increases, but for the first modes the eigenvalues are almost equal. Of course the analytical values are just a simplification of reality due to the diffusion approximation. But again PHANTOM at least appears to calculate the correct alpha eigenvalues for the first few modes.

Table 3.3 Comparison of numerical forward/adjoint and theoretical eigenvalues of a diffusive slab

Mode - n	$\alpha_n \left[s^{-1} \right]$ - PHANTOM	$\alpha_n^\dagger \left[s^{-1} \right]$ - PHANTOM	$\alpha_n \left[s^{-1} \right]$ - diffusion theory
1	-0.004321844	-0.004321844	-0.0043198
2	-0.005288607	-0.005288606	-0.0052793
3	-0.006905131	-0.006905131	-0.0068785
4	-0.009179201	-0.009179208	-0.0091173
5	-0.012121955	-0.012121956	-0.0119958
6	-0.015748081	-0.015748081	-0.0155140
7	-0.020076078	-0.020076078	-0.0196719
8	-0.025128635	-0.025128635	-0.0244694
9	-0.030933110	-0.030933110	-0.0299065
10	-0.037522146	-0.037522145	-0.0359834
11	-0.044934461	-0.044934461	-0.0426999
12	-0.053215880	-0.053215880	-0.0500561
13	-0.062420641	-0.062420641	-0.0580519
14	-0.072613143	-0.072613143	-0.0666874
15	-0.096284409	-0.083870249	-0.0759626

3.5 The lambda-eigenvalue problem

3.5.1 The lambda eigenvalue equation

In this paragraph the lambda eigenvalue problem is introduced. The neutron transport equation, given by eq. (3.2), is used as the starting point. The source is neglected and the fission operator is scaled by k_{eff} to make the reactor artificially critical. In that case the time-derivative of the flux is zero and writing λ instead of k_{eff} the lambda eigenvalue problem is obtained

$$\mathbf{L}\psi_l = \frac{\mathbf{F}}{\lambda_l}\psi_l . \tag{3.35}$$

The eigenfunctions of this problem are called λ-modes or k-modes. The largest eigenvalue λ_0 is equal to k_{eff} and its eigenfunction is the fundamental lambda mode. The shape of the fundamental lambda mode does not represent any real flux distribution except when the reactor is critical. In that case the fundamental lambda mode is the same as the fundamental α-mode.

The lambda modes are used widely in modal approaches to study different transients in nuclear reactors, such as the Boiling Water Reactor. According to Verdu [2010] the lambda modes can reproduce the time evolution of a critical system adequately in the majority of transients using a small number of modes. For subcritical systems the alpha modes are expected to be a more natural basis for a modal expansion method than the lambda modes.

Equivalently to the alpha eigenvalue problem also an adjoint form of the lambda eigenvalue problem can be formulated. The adjoint lambda eigenvalue problem is defined as

$$\mathbf{L}^\dagger\psi_m^\dagger = \frac{\mathbf{F}^\dagger}{\lambda_m^\dagger}\psi_m^\dagger . \tag{3.36}$$

The adjoint lambda modes will be used as weighting functions in the lambda mode expansion method treated in chapter 6.

3.5.2 The Power Method for lambda mode determination

The fundamental lambda mode can be solved in PHANTOM by means of the Power method in a quite similar way as the fundamental alpha mode.

Choose initial $\underline{\psi}_{old}$ with $\left\|\underline{\psi}_{old}\right\| = 1$

For $k = 1,\ldots..$ **do**

$\mathbf{L}\,\underline{\psi}_{new} = \mathbf{F}\,\underline{\psi}_{old}$

$k_{eff} = \underline{\psi}_{new} \cdot \underline{\psi}_{old}$

$\underline{\psi}_{new} = \dfrac{\underline{\psi}_{new}}{\left\|\underline{\psi}_{new}\right\|}$

$\underline{\psi}_{old} = \underline{\psi}_{new}$

$\underline{\psi}_{new} = k_{eff}\underline{\psi}_{new}$ this step gives a good initial guess for the next iteration

End

Each single power iteration step is a fixed source calculation in itself. In the formulation chosen by eq. (3.17) the fission operator disappears from the left-hand side and appears in the right-hand side: $Q_0 = \mathbf{F}\,\underline{\psi}_{old}$. The fact that the fission operator appears in the right hand side of the equation causes the calculation of lambda mode(s) to converge much quicker than the calculation of the alpha mode(s). It also allows the calculation of lambda modes for (super)critical systems.

3.5.3 The Arnoldi Method for lambda mode determination

Similar to the alpha modes the determination of more dominant eigenmodes of the lambda eigenvalue problem is performed by the Implicitly Restarted Arnoldi Method. The lambda eigenvalue equation is written into form of a standard eigenvalue problem $\mathbf{A}\underline{x} = \lambda\underline{x}$ by writing:

$$\left[\mathbf{L}^{-1}\mathbf{F}\right]\psi_\lambda = \lambda\psi_\lambda \tag{3.37}$$

This standard eigenvalue problem can be solved by ARPACK and this gives the eigenvalues λ and the eigenfunctions ψ_λ.

Since PHANTOM has been used already in a much more extensive way to calculate lambda modes and the results of lambda mode calculations during the thesis gave accurate results there is no reason to elaborate analytical test cases concerning the lambda mode computation in this thesis report.

3.6 Practical application of PHANTOM

For practical use of the PHANTOM code package the user must first of all create a mesh file describing the geometry of the system and link it for use in PHANTOM. For 2D and 3D geometries the mesh can be created with a program such as GMSH, but also a relatively simple fortran-script will work. Properties of a 1D-Mesh can be specified in a simple scriptfile. Secondly an ASCII or AMPX library must be used as an input of the cross sections. Finally the user has to specify several properties of the calculation in an input-file. An overview of the important input parameters and their options or relevant considerations is given in Table 3.4.

Table 3.4 Overview of important input properties for PHANTOM calculations

Property	**Options**
Cross section library	Asci, AMPX
Geometry	X, XY, XYZ, RZ, 1D Cylindrical, 1D Spherical
# Materials	Linking of the cross sections to the material numbers in the mesh
# Sources	Strength of sources
P_N-expansion	N > 0
Order of scattering	$0 \leq N_s \leq N$
Type of calculation	Fixed source, Lambda modes, Alpha modes, Time-dependent
Eigenvalue solver	Power method / Arnoldi Method (incl. # Arnoldi vectors)
Convergence criteria	Concerning the Arnoldi Method and Gauss-Seidel iterations
If time dependent: Time-dependent scenario	Source startup, Source shutdown, Pulsed mode
Time-dependent block	# time steps, size of time steps

After specifying the mesh, the cross sections and the relevant properties from Table 3.4, the calculation can be performed by PHANTOM. The results can be used afterward for post-processing, such as plotting fixed source and time-dependent solutions or eigenmodes of the system. Also the alpha modes and lambda modes can be used in the modal expansion theories to be developed in chapter 5 and 6. This procedure is schematically shown in Figure 3.9.

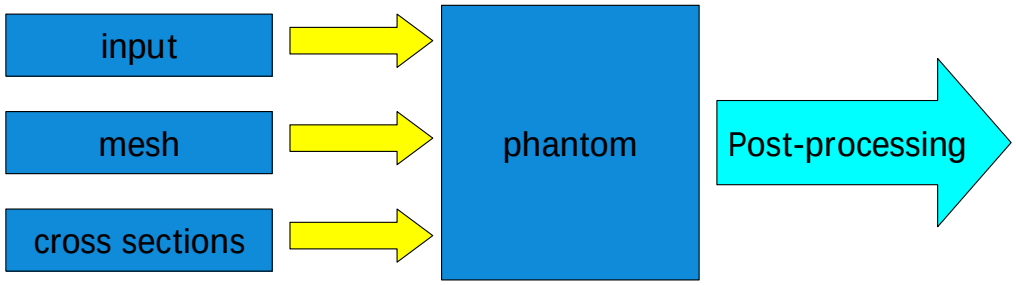

Figure 3.9 Practical scheme of the use of the PHANTOM code package

4 Steady state and transients of 3D GUINEVERE

In this chapter the results from several calculations of the GUINEVERE configurations are presented and the geometrical models used to perform the calculations are introduced. A short introduction of the GUINEVERE project was given in section 1.2. One can recall that the GUINEVERE reactor is first operated in a critical configuration and later during the GUINEVERE project in a subcritical configuration driven by the GENEPI-3C accelerator.

The first aim of this chapter is to determine and analyze the fundamental lambda mode of the critical GUINEVERE configuration with PHANTOM and to compare k_{eff} obtained by PHANTOM with values from MCNP and ERANOS calculations. The second aim is to study the time-dependent behaviour of a realistic 3D ADS-model by analyzing two transients of the subcritical configuration of GUINEVERE with PHANTOM.

If it would have been possible to calculate a sufficient number of alpha modes within reasonable time the subcritical configuration would also have been very interesting for application of the alpha mode expansion theory, developed in chapter 5. Unfortunately the calculation of several alpha modes in 3D simply takes too much time at the present moment.

4.1 The 3D-model of GUINEVERE

An introduction of the geometry of the GUINEVERE reactor and a short treatment of the generation of cross sections by SCALE is given in this section. Finally the mesh of both the critical configuration and the subcritical configuration is shown.

4.1.1 The geometry of the GUINEVERE reactor

The geometry of the critical configuration of the GUINEVERE reactor will be described briefly in this subsection to obtain a general impression of the dimension and lay-out of the facility. An extensive treatment of the geometry is given by Bianchini [2010] and Uyttenhove & Baeten [2008].

The boundary of the GUINEVERE reactor is a cylinder with a diameter of 160.8 *cm* and a height of 202.7 *cm*. Within the cylindrical vessel the GUINEVERE reactor consists of a square core lattice, surrounded by a stainless steel shaft and top and bottom support plates. The core is surrounded by a radial lead reflector around the core and lead reflectors above and below the core. The core itself is defined by a 12*x*12-lattice filled with fuel assemblies, lead assemblies, safety rods and air gaps for the 2 control rods. Above the core the 6 safety and 2 control rods consist of B_4C. The safety rods are equal to the fuel assemblies inside the core and below the core there are 6 air gaps to drop the safety rods in case of emergency. This creates a double safety effect due to the insertion of boron, which has a high absorption cross section, into the core and the extraction of fuel from the core. During the calculations it is assumed that the control and safety rods are in top position.

Each assembly in the core has a square section with a width of 8 *cm* and an active height of the fuel is 60.96 *cm*. The fuel assembly is subdivided into a 5x5-sublattice and contains 9 cylindrical fuel elements, 12 lead elements with cladding and 4 lead elements without cladding. The fuel elements consist of metallic uranium rodlets, which are enriched 30 w% in U-235. The cross sections used in the calculations by PHANTOM have been homogenized upon the level of the whole fuel assemblies and lead assemblies.

A schematic view of the GUINEVERE core and a fuel assembly is given in Figure 4.1.

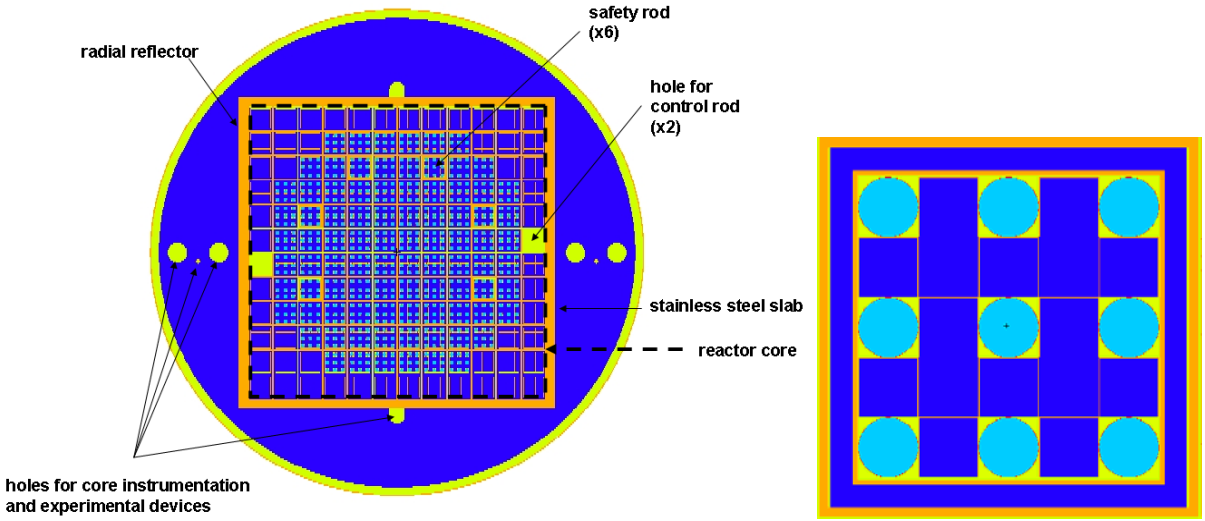

Figure 4.1 Horizontal cut of the critical GUINEVERE core (left) and a fuel assembly (right) (cyan = fuel, blue = lead, green = air, orange = stainless steel)

4.1.2 Cross sections

For the calculations of the GUINEVERE core a set of cross sections was generated with the SCALE package. The script used for the generation of the cross sections by SCALE can be found in appendix C. Cross sections were created for three different material mixtures: the fuel assemblies, lead and the B_4C in the control and safety rods. The air and void regions, associated with the control and safety rods and the central beamline of the subcritical configuration, are modeled by taking cross sections equal to zero.

The cross sections were determined by SCALE by performing a calculation over a cylindrical pin with a height of 60.96 *cm* consisting of an inner cylinder with fuel, surrounded by a small nickel layer and an outer cylinder to include the lead, stainless steel and air gaps inside the fuel assemblies. The nickel layer is added because in practice there is a small nickel paint layer around the fuel rodlets. The diameters of the pin for the SCALE calculation were determined by taking the area of the different materials in one fuel assembly and dividing them by 9 (fuel rodlets). The following radii were used for the pin:

$r < 0.6282$ *cm* *Fuel: U-235/U-238 mixture*

$r < 0.635$ *cm* *Nickel layer*

$r < 1.5045$ *cm* *Lead mixture, stainless steel of fuel assemblies, air inside assemblies*

To obtain cross sections for the B_4C of the control and safety rods, without disturbing the calculation of the cross sections of the homogenized fuel assembly, a very small layer of the B_4C was added around the pin and these cross sections were extracted separately. In the end one set of cross sections is obtained for the homogenization over the whole fuel assembly, one set of cross sections for the lead and stainless steel mixture, used for the lead assemblies and a set of cross sections to describe the B_4C.

The energy variable was discretized by using 10 energy groups. The distribution of the groups is shown in Table 4.1. Inside the group distribution emphasis lies on the higher neutron energies since GUINEVERE is a system without a moderator and a fast neutron spectrum is expected.

Table 4.1 Distribution of the energy variable over 10 energy groups

Group	Energy range
1	1.01 MeV – 20 MeV
2	670 KeV – 1.01 MeV
3	330 KeV – 670 KeV
4	100 KeV – 330 KeV
5	50 KeV – 100 KeV
6	9.5 KeV – 50 KeV
7	950 eV – 9.5 KeV
8	100 eV – 950 eV
9	1 eV – 100 eV
10	10 μeV – 1 eV

4.1.3 The grid used for the GUINEVERE calculations

During the GUINEVERE project the reactor is operated in both a critical configuration, without source, and a subcritical configuration driven by the accelerator. A geometrical model has been made for both configurations. The structured XYZ-grids used for both configurations are plotted in the XY-plane and XZ-plane in Figure 4.2.

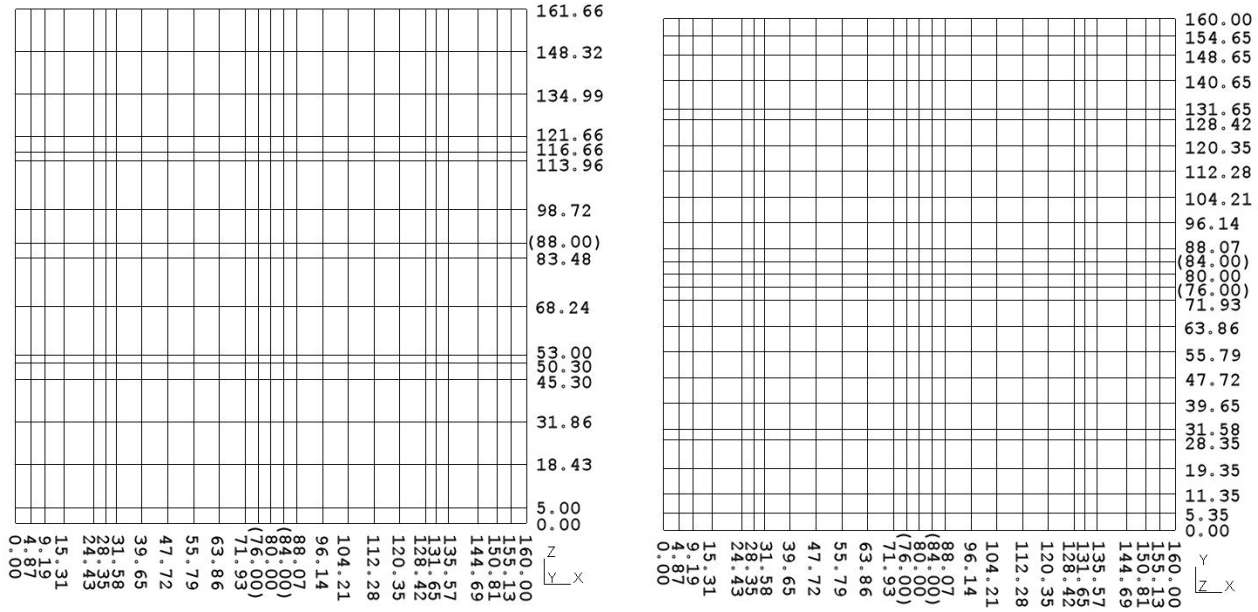

Figure 4.2 The grid of the (sub)critical GUINEVERE mesh in the XY and XZ-plane, dim. in *cm*, coordinates between parentheses are only used for the subcritical mesh

The mesh of the GUINEVERE model consists of 8-node hexahedral inner elements and 4-node quadrilateral boundary elements. The coordinates between parentheses are used only in the subcritical configuration to model the source and the accelerator beam. The mesh of the critical configuration comprises 9200 nodes, 7920 inner elements and 2436 boundary elements and the subcritical configuration comprises 11475 nodes, 9984 inner elements and 2848 boundary elements.

4.1.4 The mesh of the critical configuration

The geometrical model of a critical configuration without source of the GUINEVERE core is presented in this subsection. The XYZ-grid presented in Figure 4.2 is the basis of the mesh and the material regions are defined upon the elements of this XYZ-grid. The geometrical model of the critical

configuration is used to compare the values of k_{eff} obtained by PHANTOM using SCALE generated cross sections with other reference calculations.

The geometrical model of the critical GUINEVERE core is shown in the XY-plane for different heights in Figure 4.3. The red regions represent the fuel assemblies, grey regions lead, green regions the B_4C of the control and safety rods and the blue regions are void regions. The cylindrical reflector is modeled in an approximate way by the rectangular lead elements surrounded by void elements. The use of the void elements to describe the cylindrical reflector is necessary to ensure that a neutron streaming out through a boundary surface will not reenter the system at another point. Only such non-reentrant surfaces are allowed in neutron transport calculations.

In most calculations the reflector is modeled as a big square lead reflector to decrease the time to complete the calculation. Then the void regions at the borders of the mesh are replaced by lead. Using the void regions at the boundary causes the calculation by PHANTOM to converge only slowly and quite some inner iterations, see section 3.3.1, are required to solve the least-squares functional. A calculation of k_{eff} took over 7 hours using the cylindrical reflector with the void regions and less than 3 hours with the big square lead reflector. Values of k_{eff} will be compared later on for the cylindrical reflector and the square lead reflector.

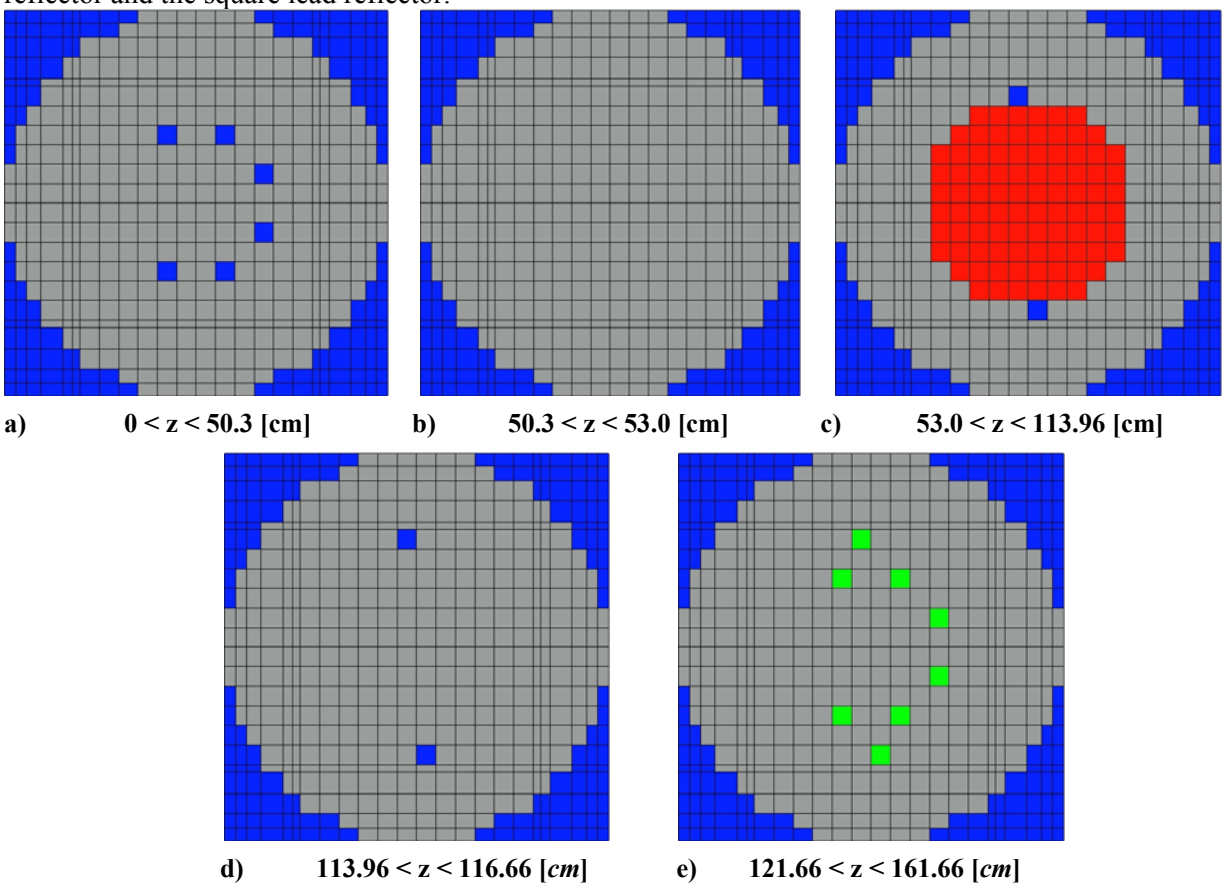

a) **0 < z < 50.3 [cm]** **b)** **50.3 < z < 53.0 [cm]** **c)** **53.0 < z < 113.96 [cm]**

d) **113.96 < z < 116.66 [*cm*]** **e)** **121.66 < z < 161.66 [*cm*]**

Figure 4.3 **XY-view of the critical GUINEVERE mesh with cylindrical reflector at different heights, grey = lead, red = fuel ass. , blue = void, green = B_4C**

A 3D side view of the core of the critical GUINEVERE mesh, without lead and reflector, is given in Figure 4.4 to get a better impression of the model.

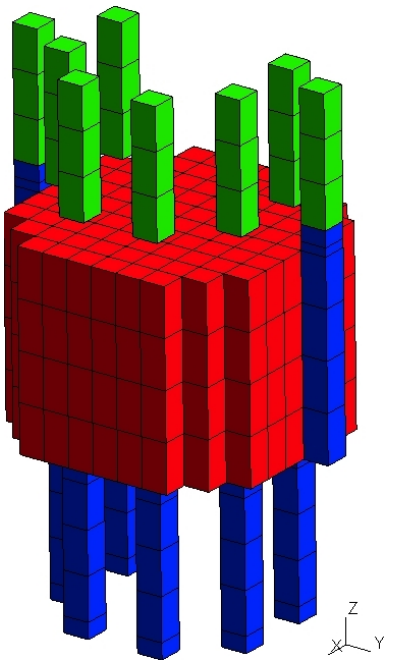

Figure 4.4 3D side view (without lead) of the critical GUINEVERE mesh

4.1.5 The mesh of the subcritical configuration

The subcritical configuration will be used to calculate the multiplication factor and to perform time-dependent calculations of the source-driven system. The subcritical system is modeled with a square lead reflector to decrease the computational time of the time-dependent calculations.

To implement the beam of the accelerator in the GUINEVERE model the 4 central fuel assemblies are replaced by a void region surrounded by lead in the upper half of the reactor. In the lower half of the core the central fuel assemblies are completely replaced by lead. In the z-direction one small layer (83.48 $cm < z <$ 88.0 cm) is added to include the source in the subcritical model. The source is defined as the 4 central elements, which consist of lead, of this layer. The geometrical model of the GUINEVERE core has been plotted in the XY-plane for different heights in Figure 4.5.

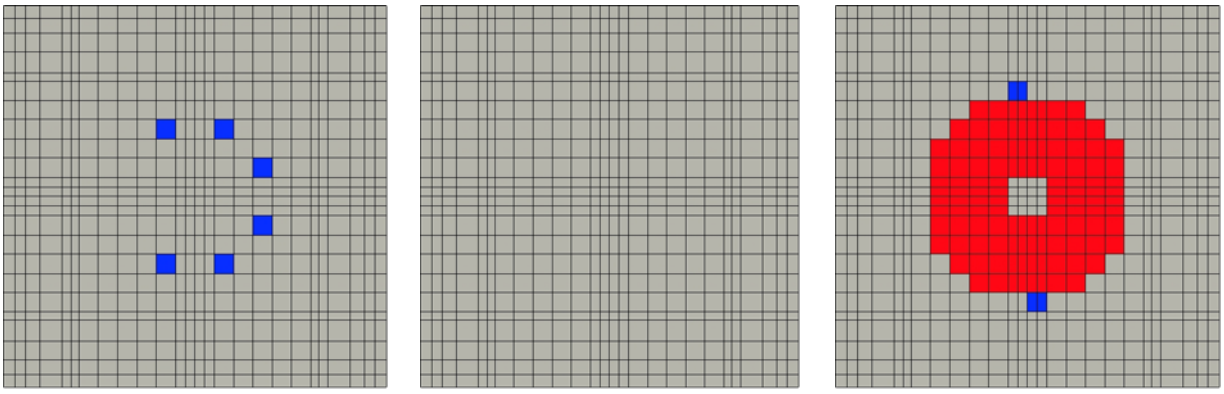

a) 0 < z < 50.3 [*cm*] **b) 50.3 < z < 53.0 [*cm*]** **c) 53.0 < z < 88.0 [*cm*]**

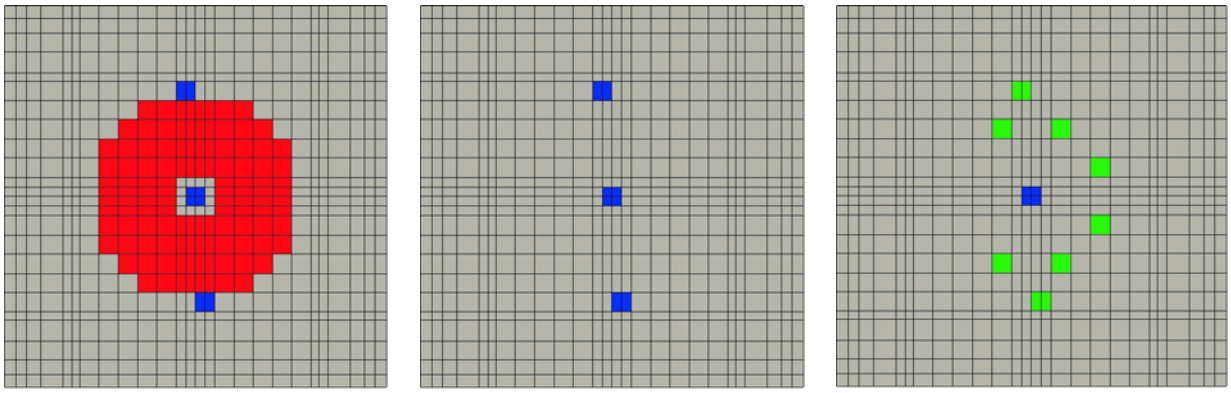

d) 88.0 < z < 116.66 [*cm*] e) 113.96 < z < 121.66 [*cm*] f) 121.66 < z < 161.66 [*cm*]

Figure 4.5 XY-view of the subcritical GUINEVERE mesh with square reflector at different heights, grey = lead, red = fuel ass. , blue = void, green = B_4C

4.2 Calculations on the critical configuration

4.2.1 The fundamental lambda mode

Calculations of the fundamental λ-mode were performed for the critical configuration with a square lead reflector using a P_1 and a P_3-expansion of the angular flux. k_{eff} was calculated with the P_1-expansion using isotropic scattering and linear anisotropic scattering. For the P_3-expansion also third order scattering was evaluated. The values of k_{eff} for the different calculation are given in Table 4.2.

Table 4.2 k_{eff} of the critical configuration using different angular expansions in PHANTOM

P_N-expansion	Scatter-order	k_{eff}	CPU-time [s]
1	0	1.05755	1415
1	1	1.00145	1338
3	0	1.08003	6337
3	1	1.02706	5957
3	3	1.02821	5931

The choice of a P_1 or a P_3-expansion has a quite significant effect on the result. The difference in k_{eff} between P_1 and P_3 is 0.02248 (isotropic scatter) and 0.02561 (linear anisotropic scatter). The order of scattering is also quite important. Using the P_3-expansion the difference between isotropic and linear anisotropic scattering of k_{eff} is 0.05297. The difference between 1st and 3rd order scattering is however small $\Delta k_{eff} = 0.00115$.

The value of k_{eff} obtained by PHANTOM (k_{eff} = 1.02821) is somewhat higher than values obtained by Uyttenhove & Baeten [2008] with MCNP (k_{eff} = 1.01031) and by Bianchini [2010] with ERANOS (k_{eff}= 1.01365). When the GUINEVERE reactor is modeled with the cylindrical reflector and void region outside of the cylinder a value of k_{eff} of 1.01621 is found for a P_3-expansion with 3rd order scattering. The latter value is close to the other reference values for k_{eff}. The relative differences are 0.58% (MCNP) and 0.29% (ERANOS) respectively. These differences can be explained by the differences in the cross section data used during the calculation. In the MCNP and the ERANOS model also more material mixtures, such as stainless steel, are taken into account than the 4 used in the PHANTOM calculation.

The fundamental lambda mode of the critical configuration with square lead reflector calculated by PHANTOM, using the P_3-expansion with 3rd order scattering, is used for visualization of the scalar neutron flux. The scalar flux has been plotted in the XY-plane at central height (z = 83.48 *cm*) of the

active fuel zone in the core for all 10 energy groups in Figure 4.6. The material composition of the mesh at central height of the core was shown in Figure 4.3c.

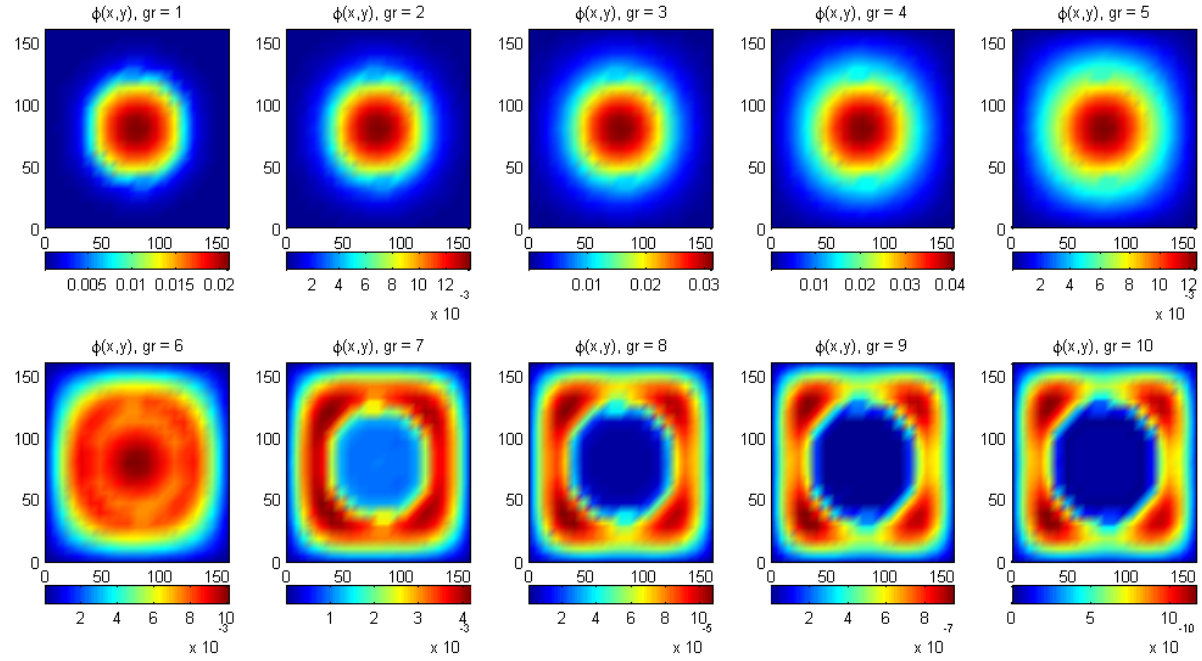

Figure 4.6 Scalar flux of fundamental λ-mode of critical configuration in XY-plane at z = 83.48 *cm*

For high energies the lambda mode at central height is dominated by the fuel region, where high energy neutrons are created during the fission process. In the 6th group the flux in the lead becomes of equal magnitude as in the fuel region. For the lower neutron energies (group 7 and higher) the lead reflector becomes the dominant region of the scalar flux. Due to the uranium the absorption cross section in the fuel region is much higher than in the lead reflector. As the neutrons are slowed down by scattering more and more neutrons are absorbed in the fuel region and consequently for the lower neutron energies the highest fluxes are found in the lead reflector.

A more detailed look at the graphs shows the effect of the air gaps, implemented for movement of the control rods, upon the scalar neutron flux. The neutron flux over a void region is completely determined by the flux at the elements surrounding it.

The scalar flux has also been plotted in the XY-plane above the core (z = 134.99 *cm*) for all 10 energy groups in Figure 4.7. The mesh at this height was plotted in Figure 4.3e.

A comparison of the color bars below the graphs shows that the scalar group fluxes in the region above the core is much lower for the groups containing high neutron energies than inside the fuel region at central height. The high energy neutrons are created inside the fuel region by the fission process and thus a higher neutron flux at central height in the core was to be expected. For lower energies (group 6 and higher) the group fluxes are of a similar magnitude since the flux is dominated by the lead regions around, above and below the core.

The B_4C of the control and safety rods has a significant effect on the neutron flux, especially for low energies, at which boron has a large absorption cross section. In the thermal region (group 10) basically all neutrons inside the control or safety rod region are absorbed. Due to the absorption by the control rods the flux inside the lead region above the core is slightly lower in the groups containing the lowest neutron energies than in the lead region around (or below) the core.

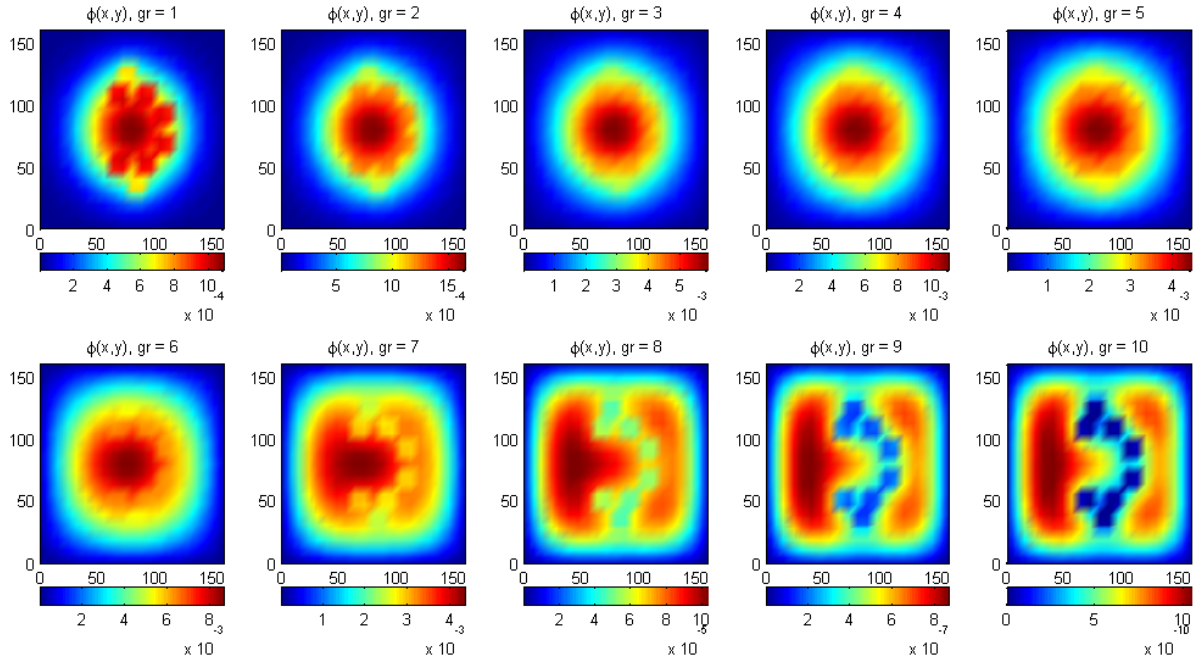

Figure 4.7 Scalar flux of fundamental λ-mode of critical configuration in XY-plane at z = 134.99 *cm*

The a-symmetric positioning of the control and safety rods also leads to an asymmetric flux profile. For the highest energy groups (with the lowest neutron energies) the neutron flux above the core is higher in the left half of the reactor. A small a-symmetry can also be observed at central height, plotted in Figure 4.6, of the GUINEVERE reactor for the lower neutron energies.

The scalar flux is plotted in the XY-plane below the core (z = 31.86 *cm*) for all 10 energy groups in Figure 4.8. The mesh at this height was plotted in Figure 4.3a.

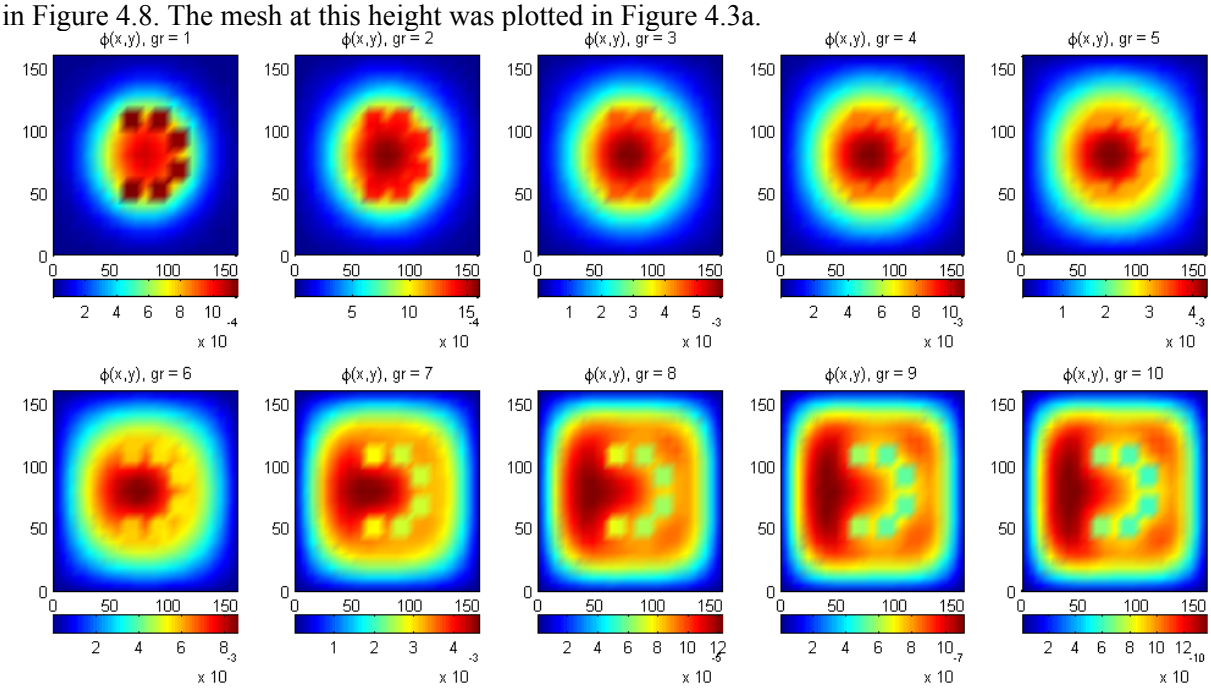

Figure 4.8 Scalar flux of fundamental λ-mode of critical configuration in XY-plane at z = 31.86 *cm*

Below the core the effect of the voids, due to the air gaps for movement of the safety rods, is visible for all 10 energy groups. In general the neutron flux over a void region is determined by the flux at the elements surrounding it. In the first group the flux at 31.86 *cm* height is higher in the void regions than in the material regions surrounding it in the XY-plane. In the first group the highest fluxes are found in

the active fuel region of the core ($z > 53.0$ *cm*). Below a height of 50.3 *cm* neutrons can travel through the void regions without being scattered or absorbed. So the void regions have become a streaming path for high energy neutrons moving away from the core and for this reason the flux at $z = 31.86$ *cm* is higher in the void regions for the first energy group.

At $z = 31.86$ *cm* the flux in the XY-plane tends to be lower inside the void regions than in the surrounding material regions for the lower neutron energies (group 6-10). At different height the flux is low inside the active fuel region and of course below the bottom of the reactor for the lower neutron energies. In this case the void regions act as a streaming path for the neutrons in the bottom lead reflector to travel out of the reflector in the direction of the core or to leak out of the bottom of the reactor.

It is interesting to notice that PHANTOM has no problem with handling such void regions. For diffusion codes the use of zero cross sections leads to more difficulties due to the division by Σ_t during the determination of the diffusion constant.

From the color bars below the graphs it is seen that the flux at low neutron energies is slightly higher below the core than above the core (at an almost equal distance from the center of the core). This is mainly caused by the strong absorption of low energy neutrons due to the control and safety rods above the core.

4.2.2 The energy spectrum

The energy spectrum of GUINEVERE can be determined at the central node of the active fuel region and at a node at central height inside the lead reflector. Inside the lead reflector the node with the highest flux in the 10th energy group was chosen. The group fluxes for the 10 groups at the two nodes are divided by the width of the energy group, ΔE_g. The result is shown in Figure 4.9 (left) and compared with an MCNP calculation performed by Uyttenhove [2010] at SCK (right). To compare both results the calculations are normalized by dividing by the flux values at an energy of 20 KeV. Since only 10 energy groups are used the spectrum by PHANTOM is only a coarse indication of the actual spectrum inside the GUINEVERE core.

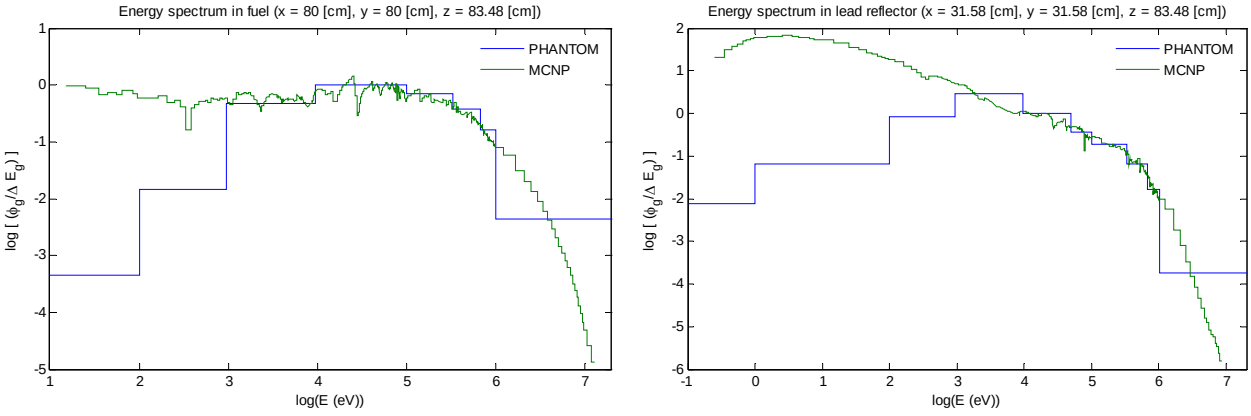

Figure 4.9 Plot of normalized energy spectrum central in the fuel (left) and in the lead reflector (right) as calculated by PHANTOM and by SCK using MCNP

The GUINEVERE reactor core has a fast spectrum since there is no moderator in the system and this can also be clearly observed from the energy spectrum by PHANTOM. The neutron flux inside the fuel region has its peak at an energy between 10 and 100 KeV. For low energies (< 100 eV) the flux inside the central fuel region is almost negligible. For the lead reflector the flux has its peak at an

energy between 1 and 10 KeV and for the high neutron energies (> 100 KeV) the flux is significantly smaller in the lead reflector compared to the fuel region.

Comparing the PHANTOM calculation with the MCNP calculation it is found that both calculations show great similarity for higher neutron energies (> 10^3 eV) and are quite different for the lower neutron energies (< 10^3 eV). The fluxes are much lower in the PHANTOM calculation for the lower neutron energies. The difference between the two calculations is mainly caused by differences in the SCALE generated cross sections and the cross sections used during the MCNP calculations. The SCALE generated cross sections used by PHANTOM were determined under simple assumptions.

4.2.3 Conclusions

Some general conclusions can be drawn from the results for the critical configuration. There is a significant difference in the values calculated for k_{eff} by PHANTOM when different orders of angular expansion and scattering are used. Using a P_3-expansion with third order scattering a value for k_{eff} of 1.01621 was calculated by PHANTOM for the critical configuration with cylindrical reflector. This value was close (< 0.6%) to values found by calculations with ERANOS and MCNP. When the cylindrical reflector was replaced by a large square reflector the computation finished roughly 2.5 times as fast at the price of a higher value for k_{eff} (1.02821). Due to the addition of the void regions for the description of the cylindrical reflector more iterations are required and the calculation converges much slower.

From plotting the scalar neutron flux of the fundamental lambda mode it became clear that the flux profile is dominated by the fuel region for high energies and by the lead reflector region for low energies. Further it was noticed that the boron carbide of the control and safety rods led to a large absorption of neutrons for the low neutron energies. The a-symmetric positioning of the safety and control rods leads to an a-symmetric flux profile. The void regions below the core were handled well by PHANTOM and also had a significant influence upon the flux shape.

From a plot of the energy spectrum at the central point of the fuel region it could be concluded that the highest neutron flux inside the fuel region occurs around 10 to 100 KeV. Inside the lead reflector the flux peaks between 1 and 10 KeV. The energy spectrum compared well to a MCNP calculation for high neutron energies (> 10^3 eV) but shows big differences for low energies (< 10^3 eV)

4.3 Calculations on the subcritical configuration

For the subcritical configuration of GUINEVERE the multiplication factor was calculated by PHANTOM. A value for k_{eff} of 0.98733 was obtained when a P_3-expansion with 3th order scattering was used and k_{eff} was found to be 0.93876 when a P_1-expansion with 1st order scattering is used. The difference between the two expansions upon the value of k_{eff} is large. Calculations of the transients in this subsection were performed with the P_1-expansion and 1st order scattering to be able to perform the calculations within a few days. An important remark before the interpretation of the results is that, due to the differences between the angular expansions for the value of k_{eff}, there might be some difference in the time scale of the transient when higher angular expansion orders are used. But the results are likely to be a good indication of the general properties of the evolution of the neutron flux over time in the GUINEVERE core.

Two transient scenarios have been studied. In the first scenario the ADS is operating under steady-state conditions and at $t = 0$ the source is turned off. In the second scenario the source is

switched on at $t = 0$ with a zero initial flux. The source of unit strength is chosen to be in the first energy group ($1.01\ MeV < E < 20\ MeV$).

To obtain accurate results from the Euler implicit time-integration scheme used by PHANTOM the time-step must be chosen small enough. To capture the most important events of the transient during the calculation the time-domain must be long enough. With respect to the computational time the number of time-steps should however not be too many. During both calculations 100 time steps of $2 \cdot 10^{-7}\ s$ were used to meet these three criteria.

4.3.1 Reactor shutdown

For the scenario of a source shutdown after operating under steady-state conditions the steady-state flux is solved first and used as an initial condition for the time-dependent calculation. The steady-state scalar flux is shown for the XY-plane at central height of GUINEVERE ($z = 83.48\ cm$) in Figure 4.10 for all 10 energy groups.

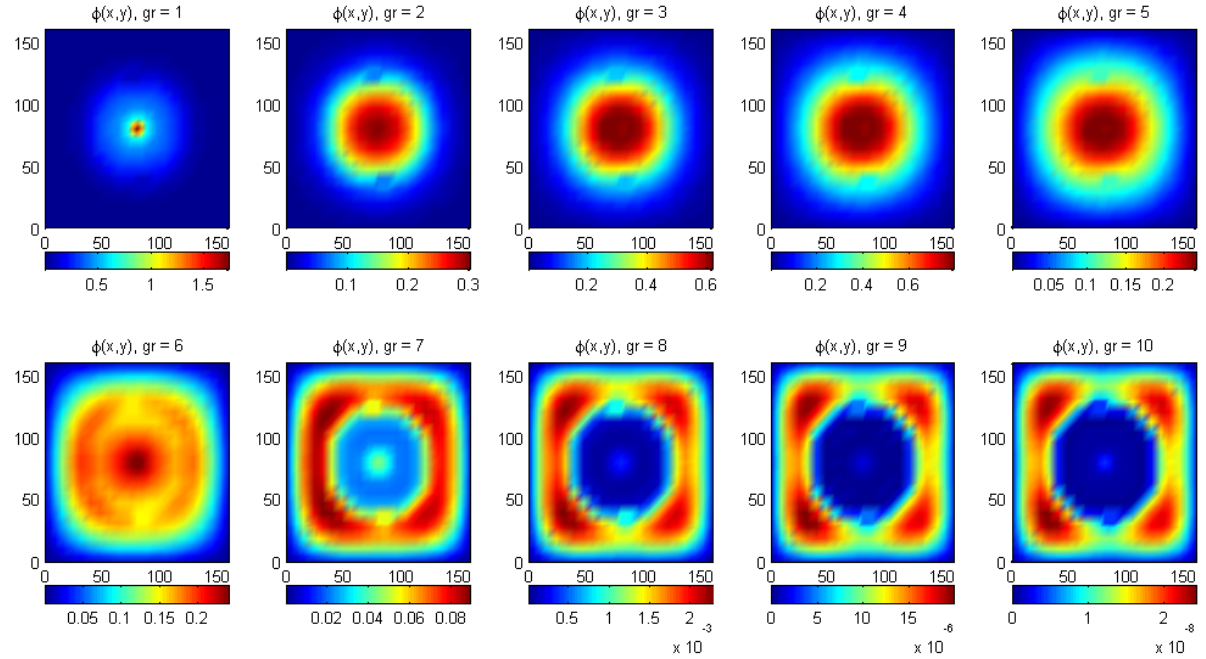

Figure 4.10 Steady state scalar flux in the XY-plane at central height in the core ($z = 83.48\ cm$)

For the higher neutron energies the flux is high in the fuel region of the core and at lower neutron energies the flux is low inside the fuel region and high inside the lead reflector. A similar observation was made for the fundamental lambda mode of the critical configuration in the previous subsection. While the shape of the group fluxes of the steady-state problem is at first sight not so much different from the fundamental lambda mode of the critical configuration, the contribution of the source neutrons results in a sharp peak in the source region of the first energy group flux. In section 2.2.3 it was already shown for a 1D diffusion ADS model with one energy group that the source influences the flux shape significantly. For increasing subcriticality the flux of a source-driven system deviated more and more from the fundamental mode.

It can also be noticed that for the lower energies (group 7-10) the flux is slightly higher inside the source region compared to the fuel assemblies surrounding it. In the subcritical configuration the four central fuel assemblies were replaced completely by lead in the lower half of the core and by lead and void in the upper half of the reactor. Since lead has a much lower absorption cross section than the fuel assemblies surrounding the lead in the center of the core, the flux is a bit higher in the source region.

Another possible cause is that low energy neutrons can travel from the top reflector to the source region trough the void of the accelerator beam. The increase of the flux at low energies inside the source region is not observed in the fundamental lambda mode of the critical configuration.

The steady-state flux is now used as an initial condition for a time-dependent calculation of the neutron flux. At t = 0 the source is turned off and the neutron flux in the subcritical system will decrease. The scalar flux has been plotted in Figure 4.11 for all 10 energy groups over a line in the x-direction (y = 80 *cm*, z = 83.48 *cm*).

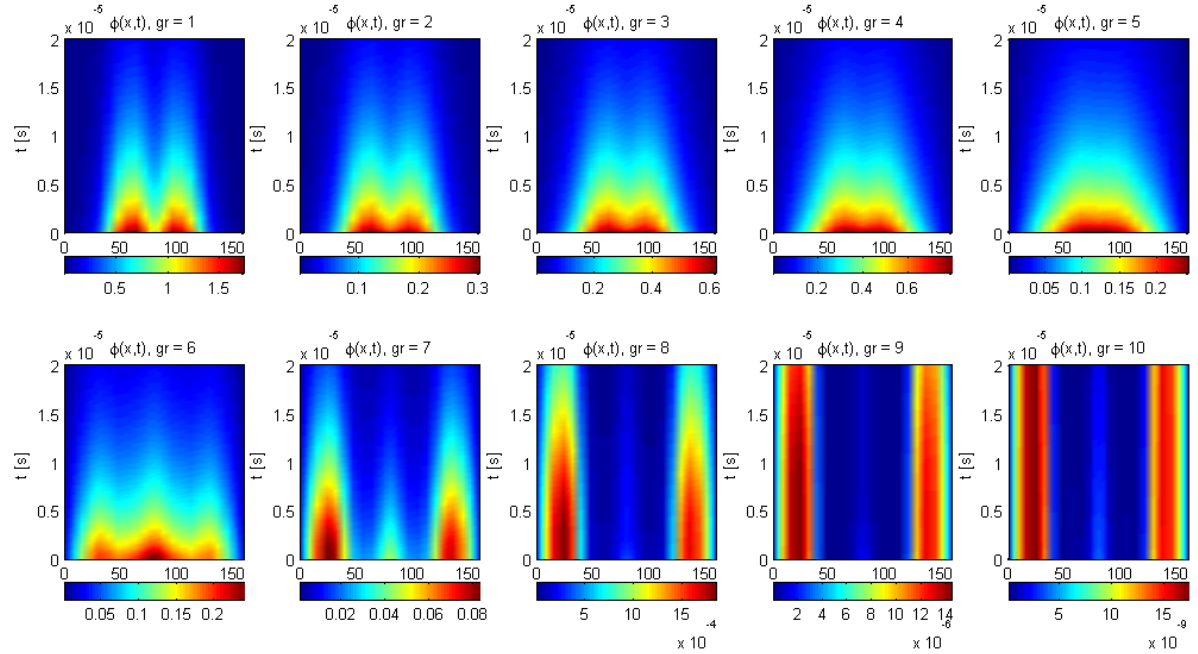

Figure 4.11 Scalar flux after source shutdown as a function of x and t at y = 80 *cm*, z = 83.48 *cm*

In the steady-state neutron flux a peak could be observed in the first energy group inside the source region. After turning of the source this peak almost immediately, within one time-step, disappears and the highest flux is found in the fissile fuel region. The decay of the source peak of the source turn-off can be described approximately by $\exp\left(-V_1\Sigma_{t,1}t\right)$, where the first group velocity V_1 is equal to $1.797\cdot10^9$ *cm/s* and the total group cross section $\Sigma_{t,1}$ is $1.938\cdot10^{-1}$ [cm^{-1}]. Filling in these numbers it is found that $2\cdot10^{-9}$ *s* after shutdown of the source only half of the amplitude of the source peak is left and after $2\cdot10^{-7}$ *s* the flux peak has completely disappeared.

A very interesting observation is that the shutdown transient appears to be described by a similar time scale for at least the first six energy groups. For the low neutron energies, especially the 9th and 10th group, the decay of the flux takes place on a much slower time scale. Meanwhile the fluxes in the 9th and 10th energy group are also very small.

4.3.2 Reactor start-up

The second transient scenario studied was the start-up of the reactor. Initially all group fluxes are zero and at t = 0 the source is switched on instantaneously. The build-up of the scalar neutron flux over time is plotted for all 10 energy groups in Figure 4.12 over a line in the x-direction (y = 80 *cm*, z = 83.48 *cm*).

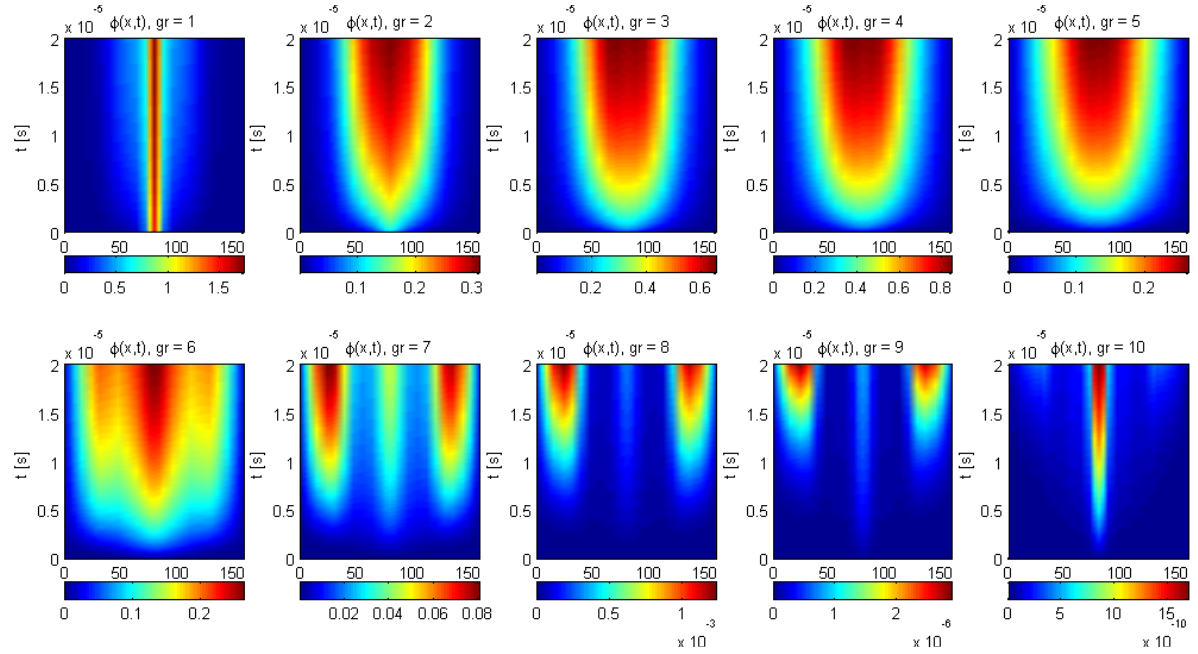

Figure 4.12 Scalar flux after source start-up as a function of *x* and *t* at *y* = 80 *cm*, *z* = 83.48 *cm*

In the first energy group a large peak in the source region occurs almost instantaneously (in the period of one time-step) after switching on the source. After this a slow additional build-up of the neutron flux takes place over the whole reactor volume, especially inside the fuel assemblies. For the lower energies the build-up of the flux takes place on a slower scale. In the 2nd till 5th energy group the flux increases in the fuel region during the transient. For the 6th till 9th energy group the flux initially increases faster in the source region but after a longer time the flux is much larger in the lead reflector region. In the 10th energy group only the increase of the flux in the source region is clearly visible. In the upper left and right corner the start of the flux build-up in the lead reflector can be seen vaguely, but it appears that the evolution of the neutron flux in the 10th energy group is too slow to capture the build-up of the flux in the lead reflector during the time-domain of the PHANTOM calculation. From the 10th-group flux of the steady-state calculation, plotted in Figure 4.10, it is known that over time the flux will become much larger in the lead reflector than in the center region.

After studying the startup of the ADS and a shutdown of the source it can be concluded that a big difference between the time scale of the physical process in the 9th and 10th energy group and the other 8 energy group exists. The fundamental time-eigenvalue for this system will be in accordance with the slow time scale of the 10th group and the fundamental alpha mode will describe the shape of the neutron flux associated with this slow time scale. The most important processes during the transient in the GUINEVERE core occur in the first 8 energy groups on a much faster time scale. For the determination of the relevant alpha modes for use in the modal expansion technique, treated in chapter 5, this raises an important issue. To determine the relevant alpha modes for the time-dependent flux expansion in an efficient and accurate way it is desirable that only alpha modes associated with these faster time scales are determined and that the slower time scale of the 9th and 10th energy group can be excluded from the calculation. This can be done by using a shift in the ARPACK routine to skip the calculation of the lower (and unimportant) alpha modes in order to calculate the alpha modes of interest or most likely also by combining the highest energy groups (group 8-10), containing the lowest neutron energies, into one group.

4.4 Conclusions

In this chapter a geometrical model of the GUINEVERE facility was made for both a critical core configuration and a subcritical core configuration. For the critical core configuration k_{eff} was determined with PHANTOM. It was found that the order of the angular expansion and the scattering order have a significant influence upon the value of k_{eff}. Using a P_3-expansion with third order scattering and modeling the lead reflector in a cylindrical shape the calculated k_{eff} was close to reference calculations with ERANOS and MCNP.

The flux profile of the fundamental lambda mode is dominated by the fuel region for high energies and by the lead reflector region for low energies. The highest neutron flux inside the fuel region occurs in the range from 10 to 100 KeV. Inside the lead reflector the flux peaks between 1 and 10 KeV. Further the effects of the control and safety rods were analyzed. The control and safety rods led to a large absorption of neutrons for the low neutron energies and the a-symmetric positioning of the safety and control rods leads to an a-symmetric flux profile in the system.

For the subcritical configuration of GUINEVERE the steady-state solution of the fixed source problem was determined first. In the first energy group the external neutron source has a significant influence on the flux shape. In the lower energy groups a small peak in the flux could be observed in the source region due to the replacement of the four central fuel assemblies by lead and some void in the upper half of the reactor. The steady-state flux was used as an initial condition for a calculation of a shutdown of the source. The peak inside the source region of the flux in the first energy group disappears almost instantaneously after turning off the source.

A second transient scenario considered was switching on the source with zero initial flux. It was found that the source neutrons caused the flux to peak inside the source region in the first energy group almost instantaneously. For both transient scenarios it was found that the neutron flux in the lower energy groups evolves on a slower time scale. The time scale of 9th and 10th energy group is much slower than the other energy groups. This may cause difficulties for the determination of the relevant alpha modes to apply the modal expansion technique describing the time-dependent neutron flux.

5 The alpha mode expansion

5.1 Alpha mode expansion theory

The evolution of the neutron flux over time inside an ADS after switching on the source or turning off the source can be determined by a direct calculation solving a fixed source problem originating from the transport equation after each time-step. This procedure was described in section 3.3.2. The time-dependent neutron flux can also be described by expressing the neutron flux as a summation over the product of time-independent spatial modes and time-dependent coefficients. A convenient choice for these modes are the ones obtained by solving the alpha eigenvalue problem defined in section 3.4.1. The alpha mode expansion technique can describe the time evolution of the neutron flux by an uncoupled set of ODEs once the alpha modes of a system have been determined. In this section the theory of the alpha mode expansion technique is derived.

5.1.1 Orthogonality of the alpha modes

The orthogonality relations of the alpha modes will be used to describe the time evolution of the modal expansion coefficients by an uncoupled set of ODEs. A derivation of the orthogonality relation of the alpha modes is given in appendix B. The orthogonality relation of the alpha modes is given by

$$\left(\alpha_n - \alpha_m{}^{\dagger}\right)\left\langle V^{-1}\psi_m^{\dagger}, \psi_n \right\rangle = 0\,, \tag{5.1}$$

where the inner product of two functions f and g is defined by integration over the whole range of space, energy and angle of the product of the two functions

$$\left\langle f, g \right\rangle = \int_V \int_E \int_\Omega f\left(\vec{r}, E, \hat{\Omega}\right) g\left(\vec{r}, E, \hat{\Omega}\right) d\hat{\Omega} dE dV\,. \tag{5.2}$$

The orthogonality relation implies that either the inner product $\left\langle V^{-1}\psi_m^{\dagger}, \psi_n \right\rangle$ is equal to zero or α_n must be equal to $\alpha_m{}^{\dagger}$ or both. $V^{-1}\psi_m^{\dagger}$ and ψ_n are orthogonal in case of non-degenerate eigenvalues.

5.1.2 The alpha mode expansion

The time-dependent neutron flux can be approximated by superposition of the alpha modes

$$\psi\left(\vec{r}, E, \hat{\Omega}, t\right) = \sum_n A_n\left(t\right)\psi_n\left(\vec{r}, E, \hat{\Omega}\right), \tag{5.3}$$

where $A_n\left(t\right)$ is the expansion coefficient for the n-th α-mode. The alpha modes are shape-functions and the expansion coefficients contain the time-dependent information of the flux expansion. It will be shown that the eigenvalue α_n play an important role in the determination of the expansion coefficients $A_n\left(t\right)$. An expression for the expansion coefficients is derived for a general source-driven neutron transport problem. Substituting eq. (5.3) into the transport equation, given by eq. (3.2), an expression for the coefficients $A_n\left(t\right)$ is obtained

$$\sum_n \frac{dA_n\left(t\right)}{dt}\frac{\psi_n}{V} = \sum_n A_n\left(t\right)\left[\mathbf{F} - \mathbf{L}\right]\psi_n + Q\left(t\right). \tag{5.4}$$

The inner product with the adjoint α-eigenfunction, as defined in eq. (5.2), is taken

$$\sum_{m,n}\left\langle \psi_m^{\dagger}, \frac{dA_n\left(t\right)}{dt}\frac{\psi_n}{V}\right\rangle = \sum_{m,n}\left\langle \psi_m^{\dagger}, A_n\left(t\right)\left[\mathbf{F} - \mathbf{L}\right]\psi_n\right\rangle + \sum_m \left\langle \psi_m^{\dagger}, Q\left(t\right)\right\rangle. \tag{5.5}$$

Use (3.31) and take terms independent of $\vec{r}, E$ or $\hat{\Omega}$ out of the brackets

$$\sum_{m,n} \frac{dA_n(t)}{dt} \left\langle \psi_m^\dagger, V^{-1} \psi_n \right\rangle = \sum_{m,n} A_n(t) \alpha_n \left\langle \psi_m^\dagger, V^{-1} \psi_n \right\rangle + \sum_m \left\langle \psi_m^\dagger, Q(t) \right\rangle. \tag{5.6}$$

If the alpha eigenvalues are non-degenerate the orthogonality of $\psi_m^\dagger$ and ψ_n is used to obtain an ordinary differential equation for each expansion coefficient $A_n(t)$

$$\frac{dA_n(t)}{dt} \left\langle \psi_n^\dagger, V^{-1} \psi_n \right\rangle = A_n(t) \alpha_n \left\langle \psi_n^\dagger, V^{-1} \psi_n \right\rangle + \left\langle \psi_n^\dagger, Q(t) \right\rangle. \tag{5.7}$$

The right-hand side of the equation is divided by the inner product on the left hand side and finally a relatively simple expression is obtained for $A_n(t)$

$$\frac{dA_n(t)}{dt} = \alpha_n A_n(t) + \frac{\left\langle \psi_n^\dagger, Q(t) \right\rangle}{\left\langle \psi_n^\dagger, V^{-1} \psi_n \right\rangle}. \tag{5.8}$$

This expression is similar to the one found by Cao [2008].

By definition of the alpha eigenvalue problem the operators **F** and **L** have been eleminated in the determination of the coefficients $A_n(t)$. Due to the biorthogonality relation of the alpha modes the coefficients $A_n(t)$ can be described by a set of uncoupled ordinary differential equations. This is very convenient because computation of $A_n(t)$ is now fairly easy and computationally cheap. For some simple cases the time-integration can even be done analytically.

If sufficient alpha modes are known a time-dependent calculation can be done without performing a full time-dependent transport calculation. Practical limitations in the use of the alpha modal expansion technique are i) the number of modes required before the modal flux reconstruction converges to the actual neutron flux and ii) the number of alpha modes that can be determined for a system with sufficient accuracy within a reasonable amount of computational time.

The alpha modes can also be used to reconstruct the steady state flux for a problem with a constant source Q_0. In this case A_n is determined by

$$A_n = -\frac{1}{\alpha_n} \frac{\left\langle \psi_n^\dagger, Q_0 \right\rangle}{\left\langle \psi_n^\dagger, V^{-1} \psi_n \right\rangle}. \tag{5.9}$$

5.2 Practical implementation of inner products

Inner products have to be evaluated during the calculation of the modal expansion coefficients, given by eq. (5.8) and eq. (5.9). Since the alpha modes used in the expansion theory are determined by the PHANTOM code the angular discretization has to be performed by spherical harmonics, the spatial discretization by finite elements and the energy discretization by multi-group theory. Important issues of the numerical integration over the phase-space originating from these discretizations are dealt with in this section.

5.2.1 Spatial and angular integration

Recall from eq. (3.8) that a function $f\left(\vec{r}, \hat{\Omega}\right)$ can be split up in an angular (spherical harmonics) and spatial dependent part as follows

$$f\left(\vec{r}, \hat{\Omega}\right) = \mathbf{f}\left(\vec{r}\right)^T \mathbf{Q}\left(\hat{\Omega}\right), \tag{5.10}$$

where $\mathbf{Q}\left(\hat{\Omega}\right)$ contains the spherical harmonics polynomials and $\mathbf{f}\left(\vec{r}\right)$ the spatial dependence of $f\left(\vec{r},\hat{\Omega}\right)$ for each angular moment. The inner product (excluding integration over energy) of two functions $f\left(\vec{r},\hat{\Omega}\right)$ and $g\left(\vec{r},\hat{\Omega}\right)$ is then given by

$$\left\langle f\left(\vec{r},\hat{\Omega}\right),g\left(\vec{r},\hat{\Omega}\right)\right\rangle_{r,\Omega}=\int_V\int_{4\pi}f\left(r,\Omega\right)g\left(r,\Omega\right)d\Omega dV=\int_V\int_{4\pi}\mathbf{f}^T\left(\vec{r}\right)\mathbf{Q}\left(\hat{\Omega}\right)\mathbf{g}^T\left(\vec{r}\right)\mathbf{Q}\left(\hat{\Omega}\right)d\Omega dV\,. \tag{5.11}$$

The product $\mathbf{g}^T\mathbf{Q}$ is a scalar. For this reason the product $\mathbf{g}^T\mathbf{Q}$ can be rewritten into $\left(\mathbf{g}^T\mathbf{Q}\right)^T$ and this is equal to $\mathbf{Q}^T\mathbf{g}$. Only the vector $\mathbf{Q}$ and $\mathbf{Q}^T$ depend on Ω reducing eq. (5.11) to

$$\left\langle f\left(\vec{r},\hat{\Omega}\right),g\left(\vec{r},\hat{\Omega}\right)\right\rangle_{r,\Omega}=\int_V\mathbf{f}^T\left(\vec{r}\right)\left[\int_{4\pi}\mathbf{Q}\left(\Omega\right)\mathbf{Q}^T\left(\Omega\right)d\Omega\right]\mathbf{g}\left(\vec{r}\right)dV\,. \tag{5.12}$$

Using the orthogonality relations, given by eq. (3.9), of the spherical harmonics the inner product reduces to

$$\left\langle f\left(\vec{r},\hat{\Omega}\right),g\left(\vec{r},\hat{\Omega}\right)\right\rangle_{r,\Omega}=\int_V\mathbf{f}^T\left(\vec{r}\right)\mathbf{g}\left(\vec{r}\right)dV\,. \tag{5.13}$$

Now $\mathbf{f}\left(\vec{r}\right)$ and $\mathbf{g}\left(\vec{r}\right)$ are expanded with the 'half' FEM basis functions introduced in section 3.2

$$\mathbf{f}\left(\vec{r}\right)=\sum_{e=1}^{E}\sum_{n=1}^{n_e}\mathbf{f}_n h_n^e\left(\vec{r}\right), \tag{5.14}$$

where E was the total number of elements and n_e the number of nodes of element *e*. Using the FEM expansion the volume-integral can be written as a summation of the integral over the volume of each element

$$\left\langle f\left(\vec{r},\hat{\Omega}\right),g\left(\vec{r},\hat{\Omega}\right)\right\rangle_{r,\Omega}=\sum_e\int_e\sum_{i=1}^{n_e}\sum_{j=1}^{n_e}\mathbf{f}_i^T\mathbf{g}_j h_i^e\left(\vec{r}\right)h_j^e\left(\vec{r}\right)dV=\sum_e\sum_{i=1}^{n_e}\sum_{j=1}^{n_e}\mathbf{f}_i^T\mathbf{g}_j\int_e h_i^e\left(\vec{r}\right)h_j^e\left(\vec{r}\right)dV\,. \tag{5.15}$$

The indexes i and j range from one to the number of nodes on the element *e*. The spatial integral over the basis functions on the element is evaluated by means of the (Gaussian) quadrature introduced in section 3.2.

5.2.2 Energy dependence

In order to evaluate the inner products of the α-mode expansion, also integration over energy is required. The integral over energy can be split up into a sum of integrals over the energy groups

$$\begin{aligned}\left\langle \psi^\dagger,V^{-1}\psi\right\rangle_{\vec{r},E,\hat{\Omega}}&=\int_E\left\langle\psi^\dagger\left(\vec{r},E,\hat{\Omega}\right),\frac{1}{V\left(E\right)}\psi\left(\vec{r},E,\hat{\Omega}\right)\right\rangle_{\vec{r},\hat{\Omega}}dE\\&=\sum_g\int_{E_g}^{E_{g-1}}\left\langle\psi^\dagger\left(\vec{r},E,\hat{\Omega}\right),\frac{1}{V\left(E\right)}\psi\left(\vec{r},E,\hat{\Omega}\right)\right\rangle_{\vec{r},\hat{\Omega}}dE\end{aligned}\,. \tag{5.16}$$

In the multigroup discretization one would intuitively write the integration over energy in terms of the group fluxes and group velocities as follows

$$\left\langle \psi^\dagger,V^{-1}\psi\right\rangle_{\vec{r},E,\hat{\Omega}}=\sum_g\frac{1}{V_g}\left\langle\psi_g^\dagger\left(\vec{r},\hat{\Omega}\right),\psi_g\left(\vec{r},\hat{\Omega}\right)\right\rangle_{\vec{r},\hat{\Omega}}\,. \tag{5.17}$$

The integration over the energy domain is treated as a summation of the contributions of each separate group. The product $\left\langle \psi_g^\dagger\left(\vec{r},\hat{\Omega}\right),\psi_g\left(\vec{r},\hat{\Omega}\right)\right\rangle_{\vec{r},\hat{\Omega}}$ is evaluated for each group by the method of the previous subsection.

5.3 Transient scenarios

For many practical applications it seems reasonable to assume that the amplitude of the neutron source varies in time but the shape of the source remains the same. In this case the source can be written as the product of a shape function and a time-dependent amplitude

$$Q\left(\vec{r},E,\hat{\Omega},t\right)=Q_0\left(\vec{r},E,\hat{\Omega}\right)T\left(t\right). \tag{5.18}$$

The coefficients $A_n\left(t\right)$ are now described by

$$\frac{dA_n\left(t\right)}{dt}=\alpha_n A_n\left(t\right)+\frac{\left\langle \psi_n^\dagger,Q_0\right\rangle}{\left\langle \psi_n^\dagger,V^{-1}\psi_n\right\rangle}T\left(t\right). \tag{5.19}$$

This expression can be used to obtain analytical expressions describing the time integration of the alpha mode expansion technique for some basic transient scenarios of an ADS.

5.3.1 Reactor shutdown

One realistic scenario to consider would be to turn off the accelerator after operating the reactor at a constant power level. First of all this is an important transient in the actual use of an ADS. In practice the accelerator will be turned off either on purpose or it happens unintended due to some excursion of the accelerator. Secondly this is an interesting scenario for studies of the modal expansion since it reveals the (prompt) time scales involved in an ADS. At the beginning of the transient both the fundamental and first few dominant modes as well as the higher modes are important for the modal flux approximation. During the transient the importance of the higher modes in the flux reconstructions reduces and at the end of the transient the flux can be described by only a few modes.

In this case first the coefficient $A_n\left(0\right)$ is determined by solving the steady state problem as described by eq. (5.9). The coefficients $A_n\left(0\right)$ are used as initial condition to solve

$$\frac{dA_n\left(t\right)}{dt}=\alpha_n A_n\left(t\right), \tag{5.20}$$

which leads to the following result

$$A_n\left(t\right)=A_n\left(0\right)e^{\alpha_n t}. \tag{5.21}$$

In a system without a source the contribution of alpha mode *n* to the flux expansion decays over time with constant α_n. This follows from the physical interpretation of the alpha mode, stated in section 3.4.1. The contribution of the modes with a large (negative) time-eigenvalue will die out quickly in the solution and after a longer period of time the solution will depend on a limited number of dominant alpha modes.

5.3.2 Reactor start-up

Another realistic scenario would be to turn on the accelerator in continuous mode. During the early stage of the transient the higher modes are most important. At later stages both the lower dominant

modes as well as the higher modes are relevant. After sufficient time the time-dependent neutron flux of the ADS stabilizes and converges towards the steady-state flux.

The initial condition is $A_n(0)=0$. Eq. (5.19) has to be solved to obtain the coefficients $A_n(t)$. Taking $\alpha_n A_n(t)$ to the left hand side and using the product rule this can be rewritten as

$$\frac{d}{dt}\left(e^{-\alpha_n t}A_n(t)\right)=\frac{\left\langle \psi_n^{\dagger},Q_0\right\rangle}{\left\langle \psi_n^{\dagger},V^{-1}\psi_n\right\rangle}T(t)e^{-\alpha_n t}. \tag{5.22}$$

After performing the integration with respect to time it is found that

$$A_n(t)=\frac{\left\langle \psi_n^{\dagger},Q_0\right\rangle}{\left\langle \psi_n^{\dagger},V^{-1}\psi_n\right\rangle}e^{\alpha_n t}\int_o^t T(t)e^{-\alpha_n t}dt. \tag{5.23}$$

If $T(t)$ is a step-function so $T(t)=1$ for $t\geq 0$ it is found that

$$A_n(t)=-\frac{1}{\alpha_n}\frac{\left\langle \psi_n^{\dagger},Q_0\right\rangle}{\left\langle \psi_n^{\dagger},V^{-1}\psi_n\right\rangle}\left(1-e^{\alpha_n t}\right). \tag{5.24}$$

After sufficient time the expansion coefficients $A_n(t)$ converge to the coefficients of the steady-state problem, given by eq. (5.9), and logically the time-dependent modal flux reconstruction converges towards the steady-state neutron flux.

For large negative values of α_n the coefficient $A(t)$ will converge rapidly towards the coefficient of the steady-state situation. As a result the time needed for the flux of the ADS to converge to the steady state situation is dominated by the time-eigenvalue of the fundamental mode.

5.3.3 Pulsed source

Another important time-dependent scenario for accelerator driven system is an accelerator working in a pulsed mode. The GENEPI-3C accelerator used in the GUINEVERE experiment can be used in both a continuous and a pulsed mode. Initially the neutron flux is zero in the ADS. At $t=0$ the accelerator is switched on during a pulse length t_p. After this the accelerator is turned off again and after one pulse period T_p it switches on again till $t=T_p+t_p$. A schematic plot is given in Figure 5.1.

Figure 5.1 Time-dependent amplitude of the pulsed neutron source

In terms of reactor physics this case is obviously more complex than the scenarios of starting up and turning off the reactor. The solution of this problem does in a certain sense consist of combining solutions of those two scenarios.

First a parameter $n_p(t)$ can be defined:

$$n_p(t)=p \text{ if } (p\text{-}1)T_p<t\leq pT_p. \tag{5.25}$$

The parameter $n_p(t)$ describes the number of pulses the accelerator has transmitted to the system, including the pulse it may be transmitting at *t*. The parameter $n_p(t)$ is needed in an analytical expression describing $A_n(t)$.

If the initial flux of the ADS is zero the coefficients $A_n(t)$ for an ADS working in pulsed mode can be calculated. If $(p\text{-}1)T_p < t \le (p-1)T_P + t_p$ they are given by

$$A_n(t) = -\frac{1}{\alpha_n}\frac{\langle \psi_n^\dagger, Q_0 \rangle}{\langle \psi_n^\dagger, V^{-1}\psi_n \rangle}\left[1 - e^{\alpha_n\left(t-(n_p(t)-1)T_p\right)} + \left(1-e^{\alpha_n t_p}\right)\sum_{p=1}^{n_p(t)-1} e^{\alpha_n\left(t-t_p-(p-1)T_p\right)}\right] \tag{5.26}$$

and if $(p\text{-}1)T_p + t_p < t \le pT_P$ by

$$A_n(t) = -\frac{1}{\alpha_n}\frac{\langle \psi_n^\dagger, Q_0 \rangle}{\langle \psi_n^\dagger, V^{-1}\psi_n \rangle}\left(1-e^{\alpha_n t_p}\right)\sum_{p=1}^{n_p(t)} e^{\alpha_n\left(t-t_p-(p-1)T_p\right)} \tag{5.27}$$

One can see that these expressions consist of combinations of the start-up and shutdown scenarios accompanied by appropriate time shifts for the contributions of the different pulses of the source.

5.3.4 Implicit Euler time-integration

If also the shape of the source $Q(\vec{r}, E, \hat{\Omega}, t)$ is time-dependent numerical time integration might be necessary. The time-integration of $A_n(t)$ in eq. (5.8) can be solved numerically by means of an implicit Euler time integration scheme. The biggest advantage of an implicit scheme is its numerical stability. Knowing $A_n(0)$ as an initial condition and discretizing the time-dependence in eq. (5.8), it follows that

$$\frac{A_n^{i+1} - A_n^i}{\Delta t} = \alpha_n A_n^{i+1} + \frac{\langle \psi_n^\dagger, Q^{i+1} \rangle}{\langle \psi_n^\dagger, V^{-1}\psi_n \rangle}, \tag{5.28}$$

where *i* denotes the time-step of the time integration scheme. This can be rewritten to obtain

$$A_n^{i+1} = \frac{A_n^i + \dfrac{\langle \psi_n^\dagger, Q^{i+1} \rangle}{\langle \psi_n^\dagger, V^{-1}\psi_n \rangle}\Delta t}{1-\alpha_n \Delta t}. \tag{5.29}$$

This expression can easily be implemented in a computer code.

5.4 Application to a 1-dimensional ADS Model

5.4.1 The 1-dimensional ADS Model

The alpha mode expansion technique has been applied to a 1-dimensional accelerator driven system model. A 1D ADS model is of course only a limited approximation of a real ADS-system. It does however contain much of the basic characteristics of source driven subcritical systems and is expected to reveal most of the important properties of the alpha mode expansion technique. For the alpha mode expansion technique itself it makes no difference if a 1-dimensional or 3-dimensional problem is studied and a significant amount of alpha modes can be calculated for a 1-dimensional problem within a reasonable amount of time.

The 1D ADS-model chosen to apply the alpha mode expansion technique is similar to the ADS model used by Lathouwers [2003]. The ADS is a symmetric one dimensional system of 240 *cm* width. It contains a lead-bismuth (at 10 kg/m^3) zone of 40 *cm* width in the center region, fuel zones (10%-enriched UO_2 at 5 kg/m^3) on the left and the right of 27 *cm* and reflector regions on the left and right of 73 *cm* width (iron at 7 kg/m^3). The system is spatially discretized by 240 uniformly sized elements and

has vacuum boundary conditions. Cross sections for the three different material zones in the system were generated with the SCALE package for a one- and three energy group discretization. The external neutron source is defined to have a width of 20 *cm* and is located at the center of the spallation zone (-10 $cm \leq x_{source} \leq 10$ *cm*). A schematic drawing of the ADS is given in Figure 5.2.

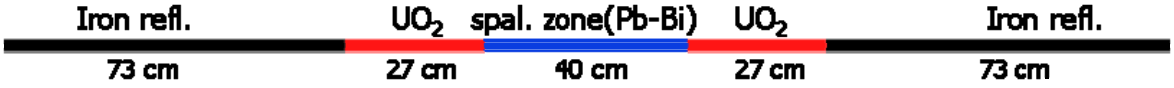

Figure 5.2 Schematic drawing of the 1D ADS model with vacuum boundary conditions

Numerical results of the steady state flux reconstruction with the alpha mode expansion and the different transient scenarios, discussed in section 5.3, will be presented for the 1D ADS-model in this section. A comparison will be made with results obtained by performing full time-dependent transport calculations with PHANTOM.

If the modal expansion technique can be used to approximate the transient behaviour of the 1D ADS model the technique itself should be easily expandable towards more complex systems as the principle behind the determination of the expansion coefficients $A_n(t)$ remains the same. The determination of a sufficient number of alpha modes is however computationally quite demanding at this moment making the applicability of the alpha mode expansion for complex multi-dimensional systems limited at the present moment.

5.4.2 One group results

In the simplest possible case the energy dependence of the problem is discretized by using only one energy group. Cross sections were generated with the SCALE package. A P_7-angular discretization with third order scatter is used during the calculations. In the 1-group case k_{eff} was determined with PHANTOM to be 0.93416. For the 1-group discretization 20 alpha modes were determined. The first three eigenvalues were found to be -23269 s^{-1}, -149296 s^{-1} and -315384 s^{-1} and correspond well to the ones found by Lathouwers [2003] with a similar 1D neutron transport code. The 19th α-eigenvalue is given by -7397735 s^{-1}, so a significant difference between the eigenvalues exists. The scalar flux of the first 6 alpha modes are plotted as an illustration of the shape of the alpha modes in Figure 5.3.

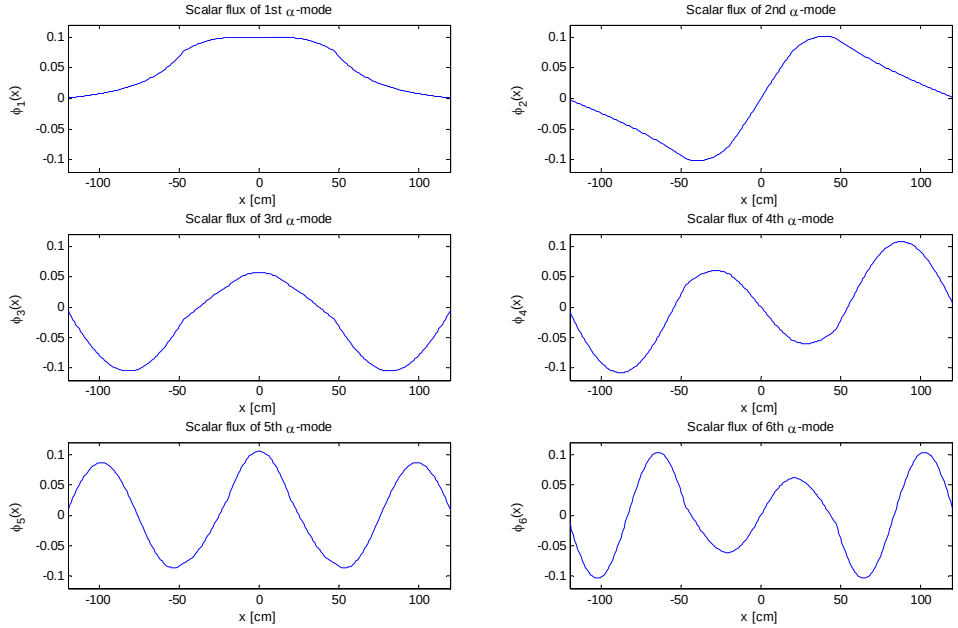

Figure 5.3 Scalar fluxes of the six dominant alpha modes of the 1-group 1D ADS model

The scalar flux of the fundamental alpha mode is positive and symmetric around $x = 0$. It can be seen that the *n*-th alpha mode contains $n-1$ zero crossings. Symmetric and asymmetric modes are found. The shape of the adjoint alpha modes is identical to the forward alpha modes. This will not be the case if more energy groups are used since the transport problem is not self-adjoint anymore due to the down-scattering operator.

The alpha modes have been used to reconstruct the steady-state flux of the 1D ADS model driven by a continuous isotropic source with unit strength. For this steady state problem the coefficients of the modal expansion are determined by eq. (5.9) and used in the modal expansion, represented in eq. (5.3). The summation of the modal approximation was truncated after a different number of modes (1, 5, 9 and 19) and the results are compared with a reference solution in Figure 5.4. The reference solution was generated by a fixed source calculation with PHANTOM.

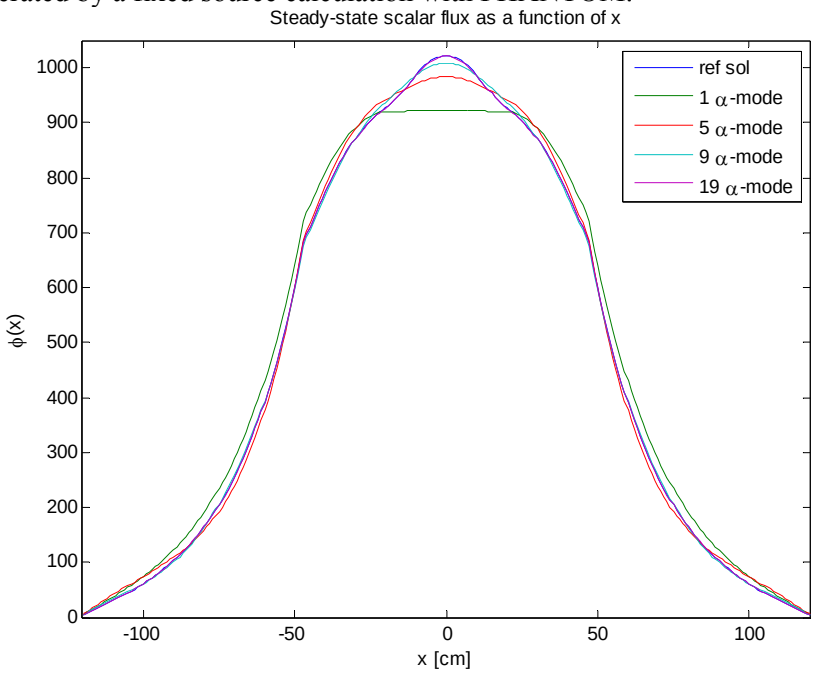

Figure 5.4 Comparison of the steady-state scalar flux reconstruction of the 1D ADS using different numbers of alpha modes and the reference solution by PHANTOM

In this 1-group case the fundamental alpha mode already gives a quite correct approximation of the flux, except for the source region. The addition of more modes into the modal expansion improves the result further and further. Using 19 modes the reference flux is accurately represented.

Now the source is turned off after operating the reactor at a constant power level. The solution of the steady state problem of the previous paragraph is used as an initial condition for the calculation of this transient. Again a reference solution is calculated in PHANTOM. The time-evolution of the coefficients in the modal expansion is calculated as prescribed by eq. (5.21).

The summation of the modal expansion is again truncated after 1, 5, 9 or 19 alpha modes and results are plotted in Figure 5.5 for the time-evolution of the scalar flux at $x = 0$ *cm*. For the steady-state problem the largest deviations between the modal expansion and the reference solution occurred at this position inside the source region.

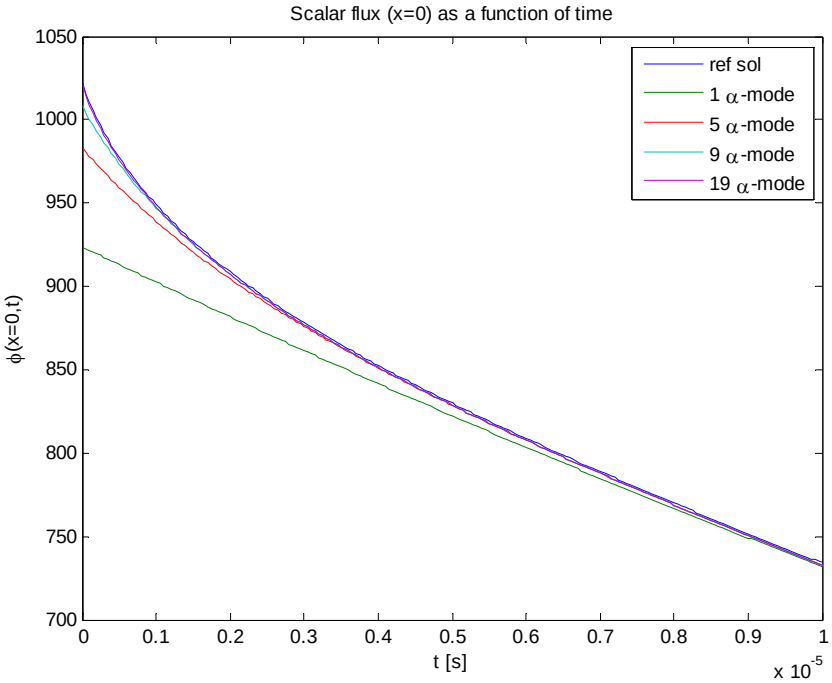

Figure 5.5 Scalar flux (x=0) of the 1D ADS after source shutdown using different numbers of modes

From the graphs in Figure 5.5 it can be concluded that the higher alpha modes play an important role in the steady state solution and during the beginning of the transient. After 10 μs the neutron flux can be accurately reconstructed by only the fundamental alpha mode. Using a sufficient number of alpha modes the scalar neutron flux can be very well represented for this transient with the discretization in one energy group.

5.4.3 Three group results

The 1D ADS model has also been investigated with a three-group energy discretization. The energy range of each group is given in Table 5.1.

Table 5.1 Energy range of the three energy groups

Group	Energy range
1	247.24 KeV – 19.64 MeV
2	27.394 KeV – 247.24 KeV
3	10 μeV – 27.394 KeV

Since the neutrons generated by the accelerator in an ADS have a high energy the continuous isotropic source with unit strength was placed into the first energy group. So the first energy group, with the highest neutron energies, contains the neutrons from the source and the neutrons from fission. The second group is chosen such that the highest flux still occurs in the central region of the ADS, which includes the fuel zone and the spallation zone. The third energy group is chosen such that the flux is lower in the fuel region than in the spallation zone and the reflector.

A P_7-angular discretization is used with third order scatter. 80 forward and adjoint alpha eigenfunctions were determined for the system and 76 of them are used for the reconstructions. For the other 4 modes the eigenvalues of the forward and the adjoint calculation did not match. The fundamental alpha eigenvalue is -38003 s^{-1} and the 72th eigenvalue is -10167897 s^{-1}. The 72th eigenvalue is the highest calculated alpha eigenvalue without an imaginary component. In total 13 complex eigenfunction pairs were determined, so the total number of (real) alpha modes used in the expansion is 63.

The steady-state neutron flux was reconstructed with the alpha modes and the scalar neutron flux is compared with the reference fixed source calculation by PHANTOM. The expansion coefficients $A_n(0)$ were determined with eq (5.9) and the superposition of the alpha modes, given by eq. (5.3), was taken. The scalar neutron flux is plotted in Figure 5.6.

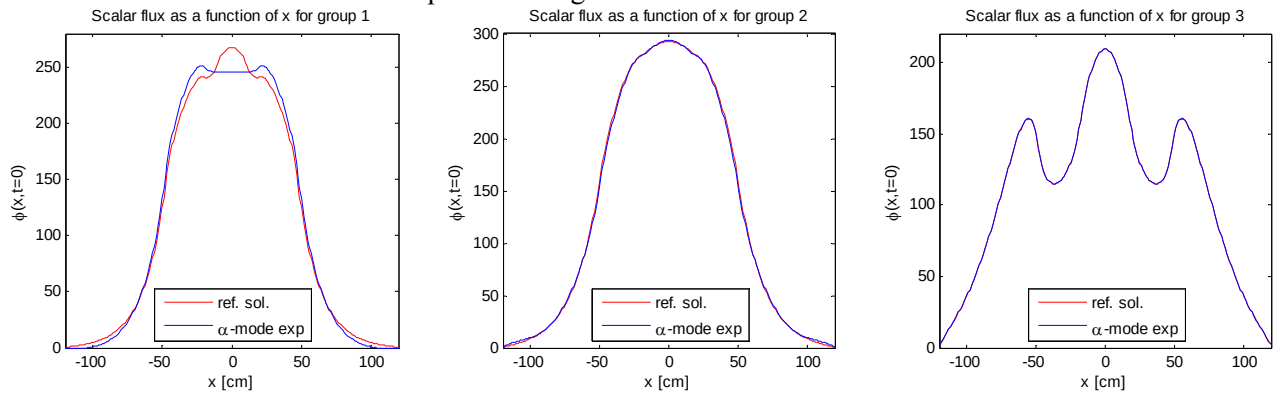

Figure 5.6 Steady state scalar flux reconstruction of the 1D ADS for the 3 different groups

The alpha mode reconstruction can describe the steady-state neutron flux quite well, but especially the reconstruction of the group flux in the first energy group is difficult inside the source region.

The transient scenario of turning off the source after operating under steady state conditions is investigated next. The steady-state flux is used as an initial condition of the time-dependent reference calculation. The coefficients $A_n(0)$ obtained for the steady-state alpha mode expansion are used to describe the time-evolution of the system by means of eq (5.21). The time-dependent neutron flux is plotted at $x = 0$ in Figure 5.7 for both the alpha mode expansion and the reference solution. The point $x = 0$ is chosen because this is obviously the most difficult point to represent by the steady-state alpha mode expansion.

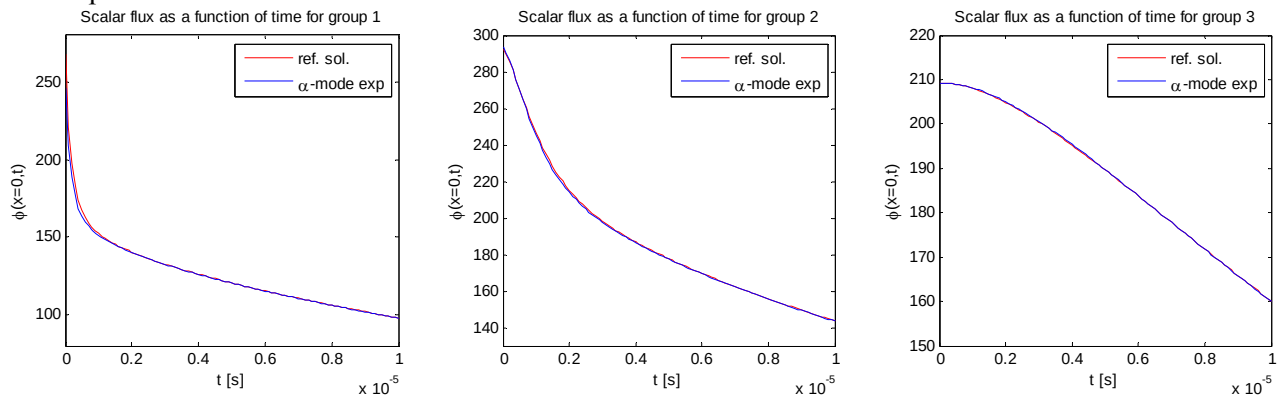

Figure 5.7 Time dependent scalar flux (x=0) of the 1D ADS for the 3 groups after source shutdown

The time-dependent neutron flux is very well represented by the alpha mode reconstruction in all three energy groups. Only during the early stage of the transient there is a small difference between the alpha mode reconstruction and the reference flux inside the source region in the first energy group. The flux at the end of the transient ($t = 10^{-5}$ s) is plotted in Figure 5.8.

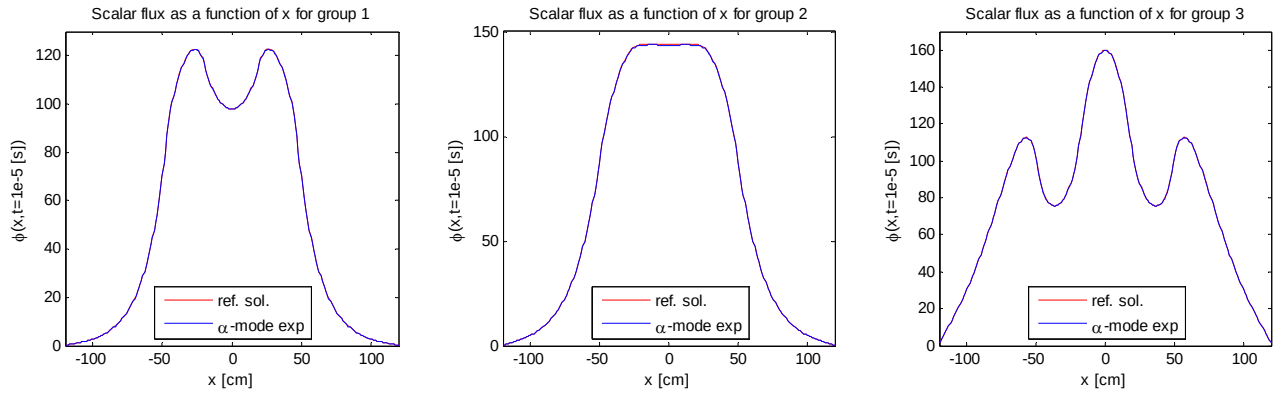

Figure 5.8 Scalar neutron flux reconstruction at the end of the transient for the 3 groups

Obviously the representation of the neutron flux is very accurate, also in the first energy group. Apparently the influence of the higher alpha modes has damped out and the flux is accurately described by only the lower alpha modes. It appears that for a correct representation of the steady state flux more alpha modes than the 63 used in the expansion will be required. It is however computationally difficult to determine these, since it requires a lot of computational time. The calculated higher alpha modes are sometimes inaccurate and a higher mode from the forward calculation cannot always be coupled to an eigenfunction from the adjoint calculation. This coupling is more difficult for higher alpha modes since sometimes eigenvalues are skipped during the forward or adjoint calculation. Eigenvalues of two different modes can also be close to each other or the eigenvalues calculated for the same mode are slightly different in the forward and adjoint calculation. The relative error in the scalar neutron flux has also been determined in a more quantative way for each energy group

$$rel.\ error = \frac{\left\langle \phi_{g,\alpha\_rec} - \phi_{g,ref}, \phi_{g,\alpha\_rec} - \phi_{g,ref} \right\rangle_{\vec{r}}}{\left\langle \phi_{g,ref}, \phi_{g,ref} \right\rangle_{\vec{r}}}, \tag{5.30}$$

where the brackets denote integration over space of the scalar fluxes. The error is a measure of the average deviation over space of the reconstructed flux with respect to the reference flux.

In Figure 5.9 the error in the scalar steady-state neutron flux is plotted for each energy group as a function of the number of modes used in the reconstruction. Also the error in the scalar neutron flux as a function of time is plotted when all 63 alpha modes are used.

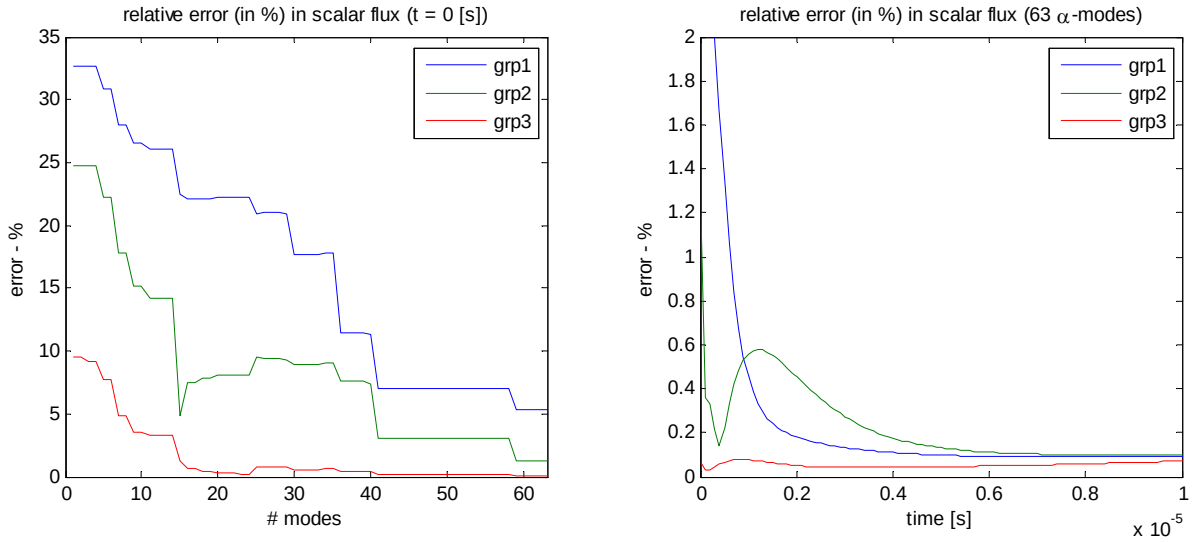

Figure 5.9 Error in the scalar flux as a function of modes (steady state) and time (63 modes)

The higher angular moments can also be included in the determination of the error. In that case the angular dependent fluxes, $\psi\left(\vec{r},E,\hat{\Omega},t\right)$, are used instead of the scalar flux and integration takes place over space and angle. It was found that the addition of the higher moments into the determination of the error basically made no difference for the magnitude of the relative error and plotted in a graph the relative error would look just the same as in Figure 5.9.

The reconstruction of the steady-state neutron flux requires the use of many modes. Using 63 modes there is still an error of around 6% in the first energy group flux due to the problems of reconstructing the flux in the source region. After a small time period the error in the first group drops rapidly. For the largest part of the transient the error in the alpha mode reconstruction is much smaller than 1% for all three energy groups. Except for the very early stage of the transient the alpha mode expansion is a very accurate way of describing the transient behaviour of the 1D ADS model in case of a source shutdown.

In the scenario of a startup of the source the time-evolution of the expansion coefficients is determined by eq. (5.24). The neutron flux at x = 0 obtained by the alpha modes expansion is compared to a reference solution by PHANTOM in Figure 5.10.

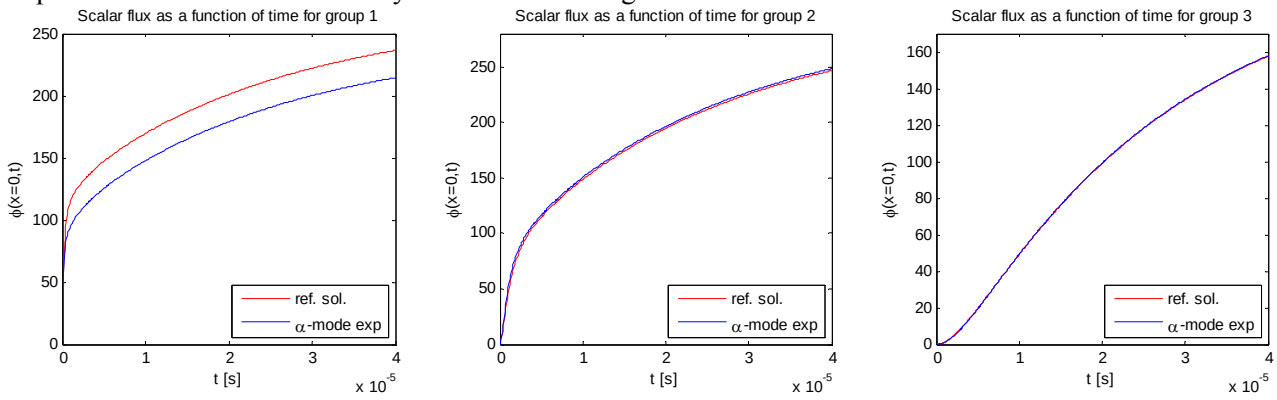

Figure 5.10 Time dependent flux (x=0) of the 1D ADS after source start-up for three groups.

The solution in the second and third energy group is quite accurate. In the first energy group there are more difficulties with the reconstruction inside the source region. After sufficient time the neutron flux will become equal to the steady-state neutron flux, plotted in Figure 5.6. At the end of the transient the error at x = 0 is of the same magnitude as the error in the reconstruction of the first group steady-state flux. One can also notice from Figure 5.10 that the largest part of the error in the first energy group flux already arises during the very early stage of the transient. This error can again be attributed to the missing higher alpha modes.

The final scenario to investigate is the case of the accelerator operating in a pulsed mode. This scenario was investigated for a pulse length t_p of 0.5 μs. The period T_p between the start of two pulses is 5 μs. In the end 8 pulses are emitted during the time domain of the calculation. The system was assumed to have a zero initial flux.

The expansion coefficients for this problem were determined with eq. (5.26) and eq. (5.27) . The reference and reconstructed scalar flux is plotted for the three energy groups in Figure 5.11 as a function of time at x = 0, where the greatest error in the flux reconstruction is expected.

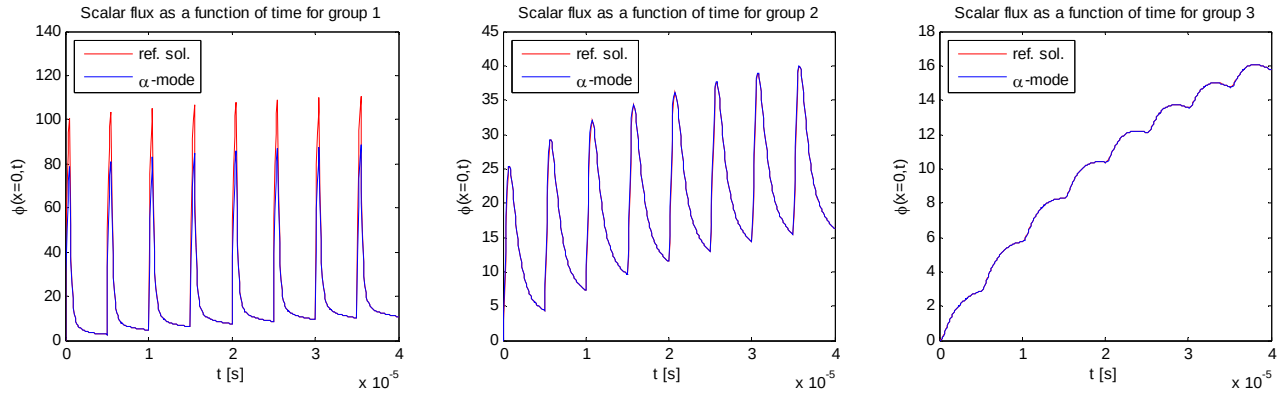

Figure 5.11 Time dependent flux (x=0) of the 1D ADS operating in pulsed mode for the three groups

At first it is interesting to focus on some properties of the physical behavior of the system for the different energy groups. In the first energy group there is a very rapid response to the power insertion by the source followed by a rapid decay after the end of the pulse. There is also a slow rise of the average flux in the first group as the number of pulses increases. In the second energy group the flux responds a bit slower to the power insertion, but also the decay takes place on a slower scale. In the third energy group the reaction to the power insertion is really slow. Most of the rise of the neutron flux in the third group takes place after the pulse has ended. This can be understood by realizing that it will take time before the neutrons, which are added in the first energy group by the source pulse and its consequential fission processes, are slowed down towards these lower energies. The lower energy neutrons also cause new fission reactions and are therefore responsible for the rise of the average flux in the first energy group with the very slow time scale of the third energy group.

If the alpha mode reconstruction is examined one sees that the main difficulty is encountered in the description of the neutron flux in the first energy group during the neutron insertion via the source pulse. Equivalently to the shutdown and start-up of the source scenarios the cause of this difficulty can again be found in the missing higher alpha modes. For the rest of the time domain and the other energy groups the description of the flux is very accurate.

An interesting result is the evaluation of the neutron flux at the end of a source pulse. The scalar flux is plotted for the three energy groups at the end of the eighth pulse at $t = 35.5\ \mu s$ in Figure 5.12.

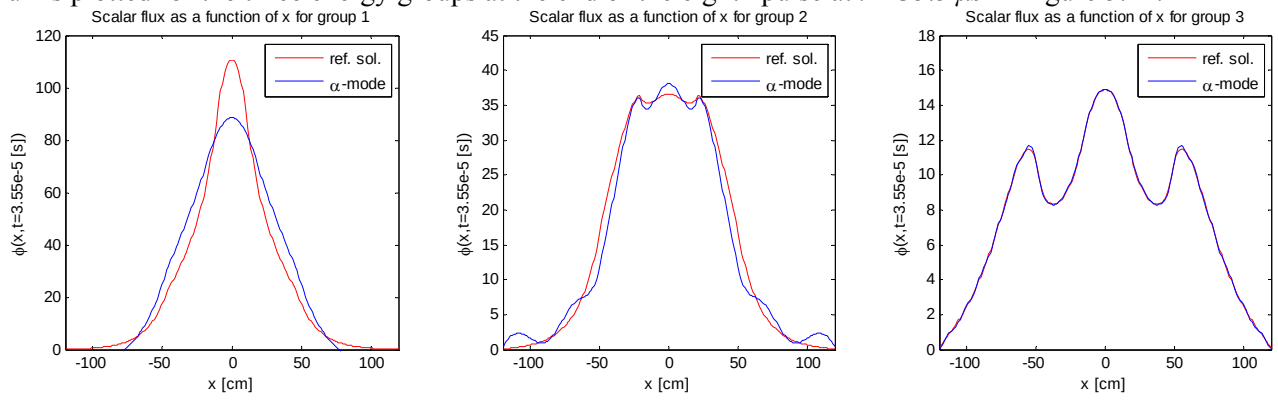

Figure 5.12 Flux of the 1D ADS operating in pulsed mode at the end of the eighth pulse ($t = 35.5\ \mu s$)

The flux reconstruction by the alpha modes clearly deviates from the reference solution in the first group. In the second group the reconstruction also does not match perfectly with the reference flux. In the third group the reconstruction leads to quite an accurate result. It appears that more modes are needed to improve the accuracy of the reconstruction at the moment the ADS is driven by the source or shortly after turning off the source. As mentioned before the higher alpha modes are difficult to

determine due to the computational time required and the inaccuracies in the determination of the higher forward and adjoint α-eigenfunctions.

A few general conclusions of the study of the 1-dimensional model with a 3 energy group discretization can be drawn. The reconstruction of the steady-state neutron flux with the alpha mode expansion technique is quite accurate with respect to the reference steady-state solution except for especially the source region of the first group flux. In case of a source shutdown the time-dependent neutron flux is well described by the alpha modes expansion except for the first energy group during the very early stages of a transient. The steady state solution and these early stages of the transient are hard to reconstruct due to the missing higher alpha modes, which describe the faster time scales involved in the decay of the neutron flux during the transient. The problems in reconstructing the rapidly varying neutron flux components also show up in case of the source start-up scenario and an ADS operating in a pulsed mode. The cause of this is again found in the lacking higher alpha modes. So a large number of modes is needed for a correct representation of the steady-state flux or flux calculations when the source is turned on.

5.5 Application to a 2D ADS model

5.5.1 The 2D ADS model

The 1D ADS model used in section 5.4 has been extended towards a 2D geometry. The same materials and cross sections are used as in the 1D ADS model of section 5.4. A schematic picture of the mesh of the 2D ADS model is given in Figure 5.13. The 2D model ADS covers 100 *cm* in the *x*-direction and 90 *cm* in the *y*-direction. Since the size of the ADS in the *x*-direction differs from the size in the *y*-direction no degenerate eigenmodes exist. If degenerate eigenmodes exist the alpha mode expansion technique can also be applied but then a coupled system of ODEs must be solved to describe the time-evolution of the expansion coefficients.

The ADS model consists of a lead-bismuth zone (blue) in the center region, a fuel zone (red) around it and an iron reflector (gray) surrounds the reactor core. The source region is defined as the lower left element (5x5 *cm*) of Figure 5.13, so its area amounts one quarter of the total area (10x10 *cm*) of the lead-bismuth zone.

Because of the symmetry of the 2D ADS, reflective boundary conditions are used in the *x*-direction and *y*-direction. This has two main advantages. First of all it reduces the mesh size of the computation by a factor 4. Secondly only the symmetric modes are calculated. If the source is positioned symmetrically with respect to the reflective boundaries only the symmetric modes will be required and the a-symmetric modes are not calculated unnecessarily. The calculations of the 2D model were performed using a P_3-expansion with third order scattering.

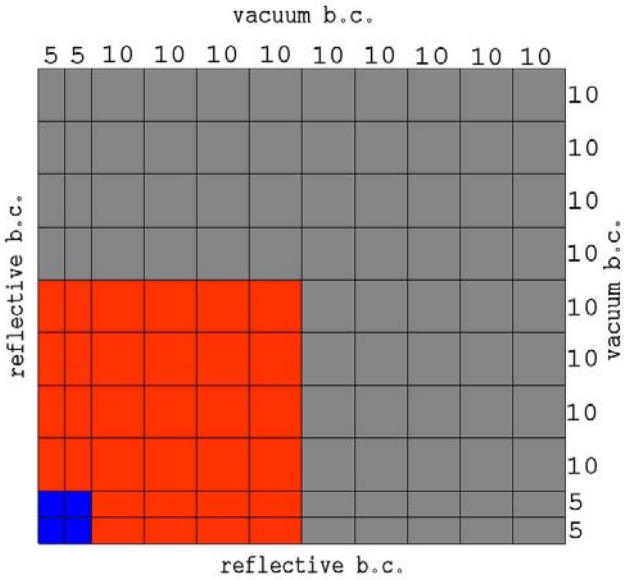

Figure 5.13 Mesh of the 2D ADS Model with boundary conditions and dimensions in *cm*

5.5.2 2D ADS model: 1-group results

A fixed source calculation was performed with PHANTOM to obtain the steady-state flux of the 2D ADS model with a source of unit strength using a 1 energy group discretization. PHANTOM was also used to perform a time-dependent calculation in case of a shutdown of the source after operating under steady-state conditions. The time-dependent calculation will later on be compared with the time-dependent alpha mode reconstruction. The scalar flux of the fixed source problem by PHANTOM is plotted in Figure 5.14.

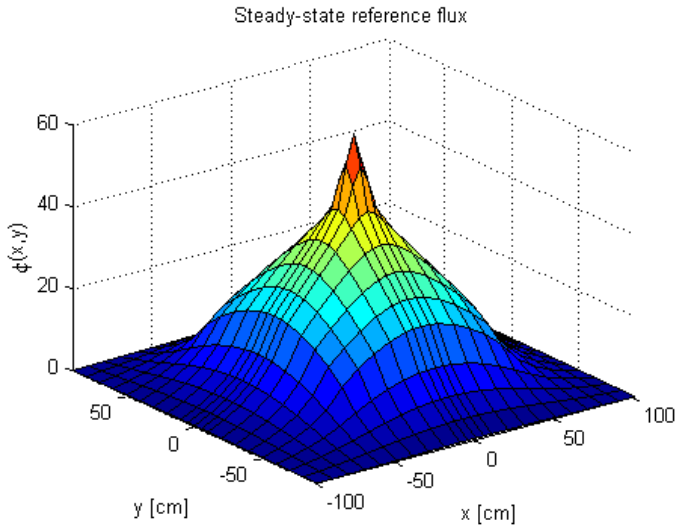

Figure 5.14 Steady state scalar flux of the 2D ADS model as calculated by PHANTOM

One should notice that the solution has been mirrored around the reflective boundaries to obtain a clear graphical interpretation of the physical process inside the ADS. So the solution is plotted over the full core instead of the quarter core defined in the mesh. The steady-state flux has a sharp peak in the center region due to the addition of the source neutrons. The flux is relatively high due to fission in the fuel zone around the source region and the flux is low inside the reflector at the boundaries of the ADS.

The alpha modes of the 2D ADS model were calculated by PHANTOM with the Arnoldi method, introduced in section 3.5.3. 90 eigenfunctions were calculated containing 14 complex eigenvalue pairs. Including the 42nd alpha mode into the expansion leads to a distortion of the flux profile by a noisy contribution to the neutron flux. The Arnoldi method will not always determine the higher alpha modes with sufficient accuracy and, as mentioned before, the calculated forward eigenfunctions do not always coincide with the adjoint eigenfunctions. One possible cause for the problems with the determination of the higher alpha modes may be that the mesh is quite coarse making it difficult to represent a (spatially) rapidly varying mode correctly upon the limited number of nodes. In the end the first 41 of the 90 alpha modes were used for an optimal result.

Figure 5.15 shows the steady-state scalar flux reconstruction using 1, 11, 21 or 41 alpha modes.

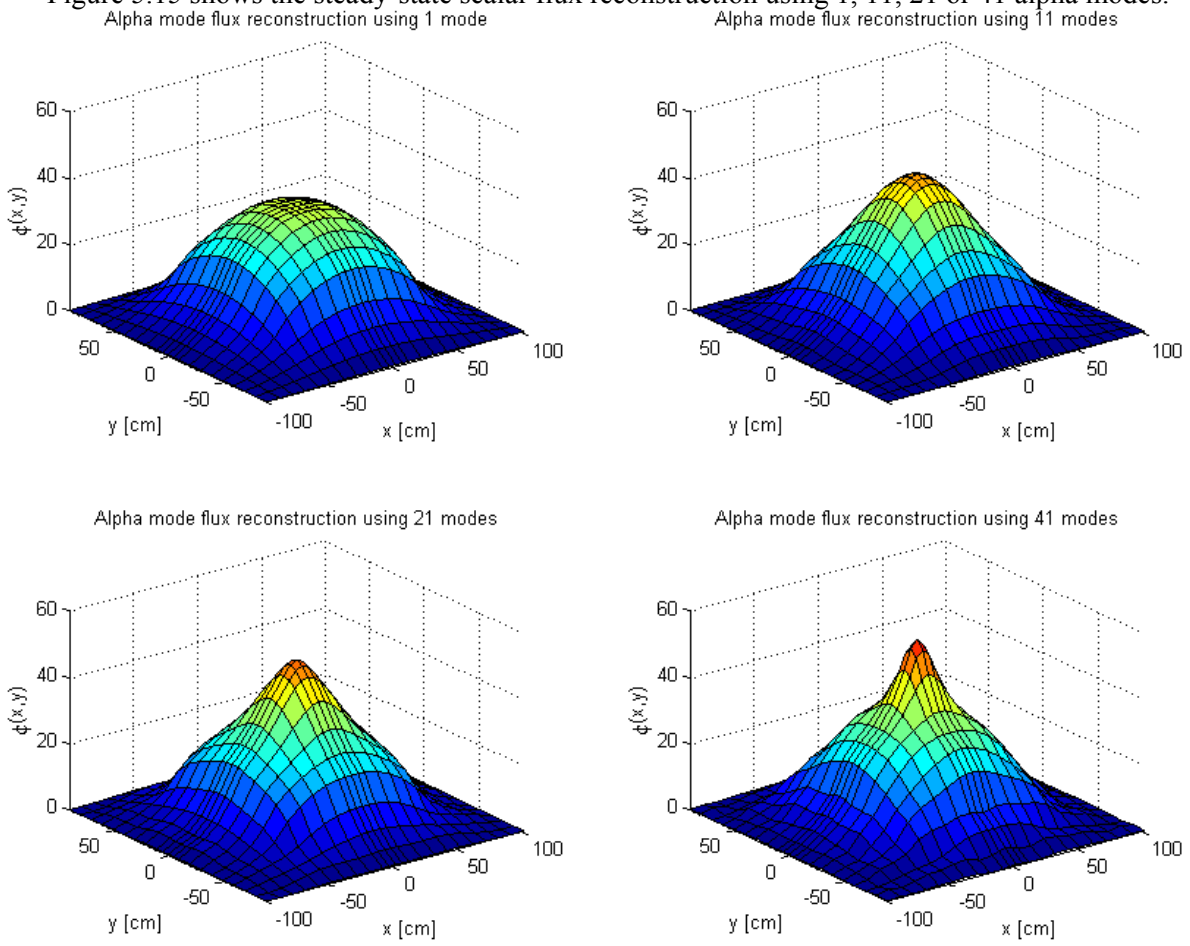

Figure 5.15 Steady state flux reconstruction of the 2D ADS using different number of alpha modes

Comparing these results with Figure 5.14 it is found that addition of more and more alpha modes improves the reconstruction significantly. The use of 41 alpha modes leads to a quite correct reconstruction of the steady-state flux in Figure 5.14. Only the peak in the source region is a bit sharper and higher in the reference flux. Using 41 modes the relative error in the scalar steady-state flux, by definition of eq. (5.30) is 2,81%. To improve the reconstruction of the neutron flux in the source region even more alpha modes are required. Unfortunately there were some issues with the accuracy of the determination of these higher alpha modes.

In Figure 5.16 an overview is given of the weights of the different modes in the alpha mode reconstruction. As one can also observe from Figure 5.15 the fundamental mode is of great importance, but also a lot of the higher modes give small, but relevant, contributions to the reconstructed flux. The

expansion coefficients $A_n(0)$ apart from the first few modes show no real decay in magnitude for the higher alpha modes. This also indicates that the solution of the model expansion has most likely not fully converged yet and also higher (> 41) modes can give relevant contributions to approximate the reference steady-state flux.

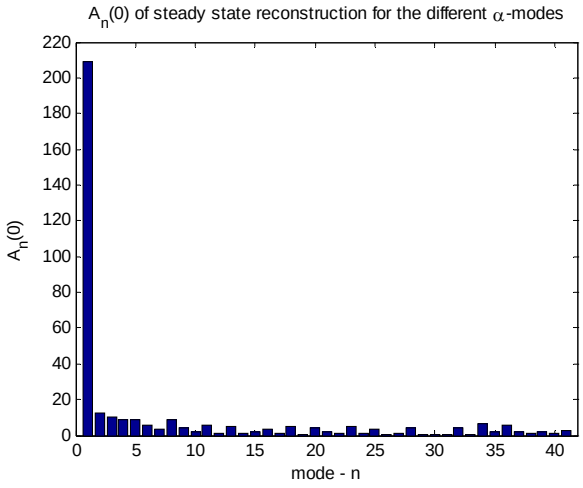

Figure 5.16 Importance of alpha modes in 2D-ADS steady-state flux expansion

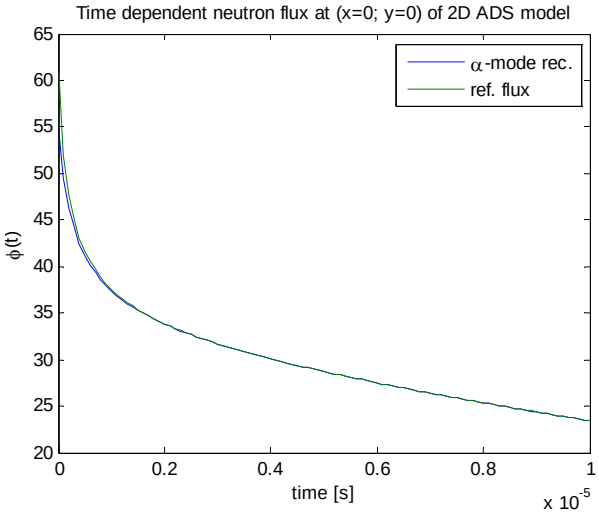

Figure 5.17 Reconstruction of scalar flux (*x,y* = 0) of the 2D ADS after source shutdown

The time-dependent neutron flux after a shutdown of the source was reconstructed using the 41 alpha modes. Equivalent to the 1D cases studied earlier the steady-state flux reconstruction shows the largest deviation from the reference solution in the center of the source region. So the time-dependent alpha mode reconstruction in case of a source shutdown has been compared to the reference solution by PHANTOM at the central position of the reactor (*x=0, y=0*) in Figure 5.17. In the PHANTOM reference calculation 100 time steps of 10^{-7} *s* each were used.

Apart from the very first stages of the transient the alpha mode reconstruction gives a very accurate result for the time-dependent neutron flux in the center of the reactor. At other positions in the reactor results with a similar accuracy can be found. Using 41 modes the relative error in the scalar flux, as defined by eq. (5.30), is only 0.33% after 5 time steps ($t = 5 \cdot 10^{-7}$ *s*) and after 100 time-steps ($t = 10^{-5}$ *s*) the relative error has reduced to 0.24%

5.5.3 2D ADS model: 3 group results

The 2D ADS model was also studied in a multi-group case. The three energy groups in Table 5.1 are used and the neutron source of unit strength is placed into the first energy group. The reference steady-state solution calculated with PHANTOM is plotted in Figure 5.18.

One first observation is that the source neutrons cause a sharp peak in the first group flux and secondly it is interesting to notice that for lower neutron energies (group 3) most neutrons are found in the iron reflector with its low absorption cross section and in the lead-bismuth center region, but the neutron intensity is much lower inside the fuel region due to the absorption of neutrons by the uranium-oxide. The absorption cross section of the uranium-oxide ($\Sigma_{a,3} = 1.14371 \cdot 10^{-2}$ cm^{-1}) is relatively large in the third energy group compared to the iron reflector ($\Sigma_{a,3} = 2.55270 \cdot 10^{-3}$ cm^{-1}) and the lead-bismuth region ($\Sigma_{a,3} = 3.36129 \cdot 10^{-4}$ cm^{-1}).

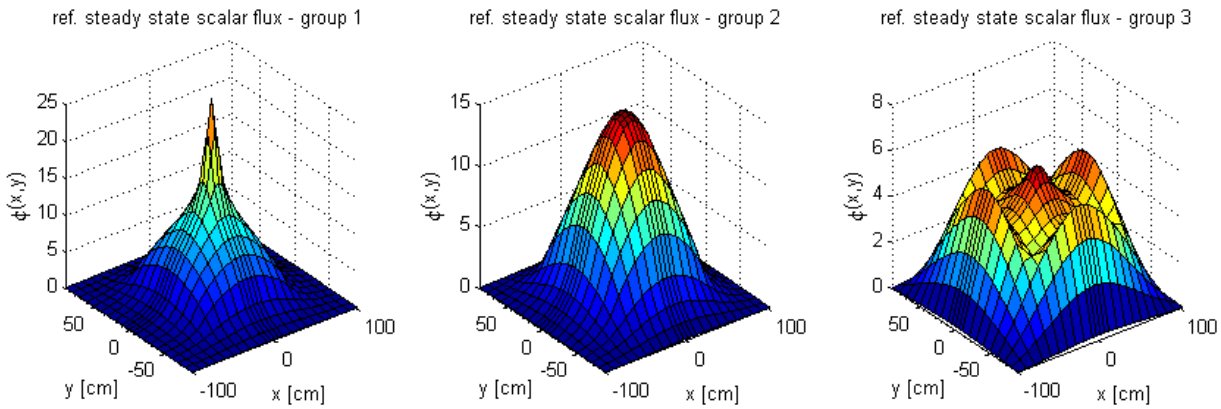

Figure 5.18 Steady state scalar flux of the 2D ADS model for three energy groups by PHANTOM

The alpha mode reconstruction can be compared with the reference steady-state group fluxes to check the correctness of the modal expansion. 90 alpha eigenvectors were calculated with the Arnoldi-method for a forward and an adjoint calculation. 81 (real) alpha modes remained after leaving out the forward eigenvectors that could not be linked to one of the adjoint eigenvectors, due to skipping of eigenvalues or simply a too large difference in eigenvalue, and after taking the complex eigenvalue pairs together into real modes. For each complex eigenvalue pair two complex vectors are regarded as one real mode.

The alpha mode reconstruction was in the end performed using only 31 alpha modes. The addition of the 32nd mode into the expansion led to a significant disturbance of the third energy group flux by some noisy contribution, similar as the problem encountered in the one-group case. Perhaps the coarseness of the mesh might be a possible cause for this behaviour. The first alpha eigenvalue was determined to be -66690 s^{-1} and the 31th alpha eigenvalue is -1873834 s^{-1}.

The alpha mode reconstruction of the steady-state flux is plotted in Figure 5.19.

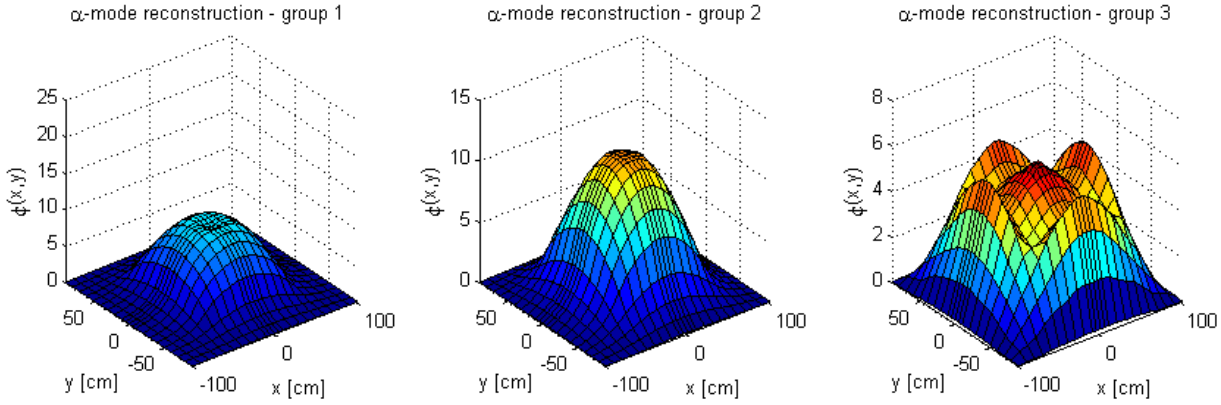

Figure 5.19 Steady state scalar flux reconstruction using 31 alpha modes for the three energy groups

The alpha mode reconstruction is unable to reconstruct the peak in the source region of the first group flux and this causes the relative error, defined by eq. (5.30), in the scalar flux reconstruction to be 27.93%. For the second group flux the shape of the reconstructed flux is similar to the reference flux but the amplitude is too low. The relative error of the 2nd group flux reconstruction is 16.25%. For the third group the reconstructed flux shows similarity to the reference flux with a relative error of 3.94%.

The shutdown of the neutron source has also been studied for the 2D ADS model using a three group energy discretization. In the PHANTOM reference calculation time steps of 10^{-7} *s* each were used. The alpha mode reconstruction in the center of the source region (*x=0*, *y=0*) is compared to the reference solution in Figure 5.20.

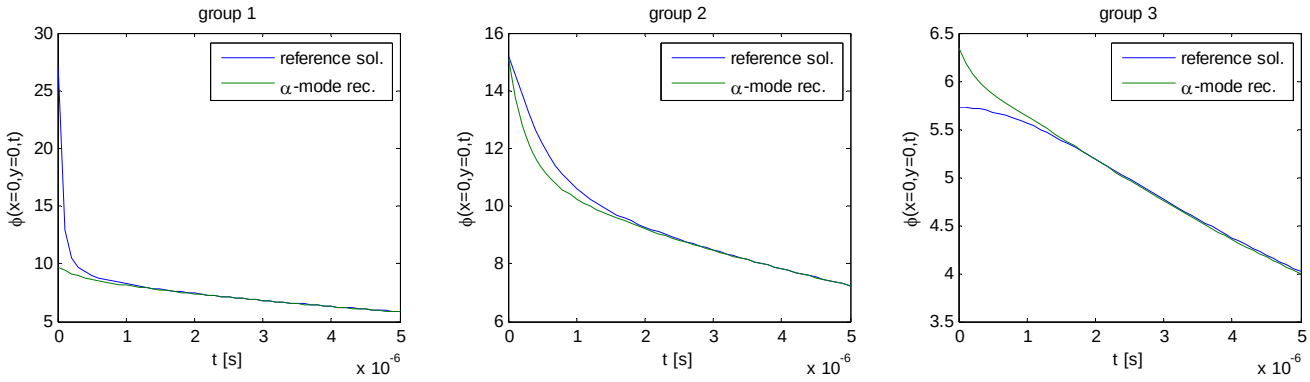

Figure 5.20 Reconstruction of time dependent scalar flux (*x*=0, *y*=0) after source shutdown

As observed before in the other cases the alpha modes can reconstruct the time-dependent behavior of the neutron flux in the center of the source region correctly after the source is turned off, except for the very early stages (the first 1 or 2 μs) of the transient. At other locations in the reactor the time-dependent neutron flux is also correctly described by the alpha mode expansion after the very early stages of the transient.

In Figure 5.21 the error in the scalar flux, determined by means of eq. (5.30), is plotted as a function of time for the three energy groups.

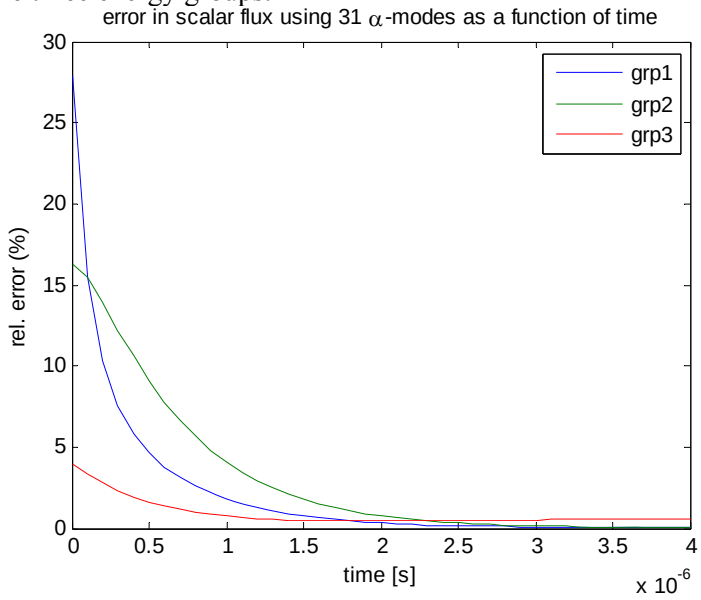

Figure 5.21 Relative error in the scalar flux reconstruction for three groups as a function of time.

The graph clearly visualizes that the solution of the alpha mode expansion is accurate with respect to the reference solution after the very early stages of the transient. After 4 μs the relative errors for the three different groups are respectively 0.0941% (1), 0,0687% (2) and 0,54% (3).

It can be concluded that using both a one energy and a three energy group discretization the alpha modes can correctly represent the time-dependent neutron flux, except for the very early stages, after a source shutdown. For a correct representation of the very early stages of the transients more alpha modes, than the 31 or 41 used now, are required. For the 2D model it is however difficult to determine these higher alpha modes in an accurate way with the Arnoldi package. Errors in the calculation of the higher modes regularly occur due to skipping of eigenvalues in either the forward or the adjoint calculation. Also the numerical accuracy seems to decrease during the calculation of the higher modes. The coarseness of the mesh might be an additional cause of the problems with the higher alpha modes. If a mode varies rapidly over the spatial domain it becomes hard to represent upon a mesh with a

limited number of nodes. Unfortunately it is not always possible to refine the mesh considering the computational time required for the determination of the alpha modes.

It is however promising that the alpha mode expansion theory in itself can be used in a multi-group discretization on a multi-dimensional reactor geometry.

5.6 A 2D simplified GUINEVERE model

The α-mode expansion technique has also been used to describe the time-dependent neutron flux after a shutdown of the source in a 2D-system with more similarity to the GUINEVERE reactor. The most important differences with respect to the ADS studied in the previous section are the use of lead in the reflector, a different material composition of the fuel region (fuel pins with a 30w%-enrichment mixed with lead) and the use of a 10 energy group discretization.

The same cross sections, produced by the SCALE package, of the GUINEVERE calculations in chapter 4 were used with the 10-energy group discretization, given by Table 4.1. A similar grid was used in the XY-plane as in the 3D model of GUINEVERE. The homogenised fuel assemblies and the lead assemblies were used as the two materials of this simplified 2D model of the GUINEVERE facility.

Initially also a void region was added for the beam in the source region and in one element outside the fuel region to resemble the effect of the control rod voids. The use of void regions led to some deviation (~1%) between the fundamental alpha eigenvalues of the forward and the adjoint calculation by PHANTOM with both the Arnoldi and Power method. It is not completely understood where this difference originates from. The deviation in the forward and adjoint eigenvalue leads to small errors in the time-dependent reconstruction of the neutron flux. Using a model without void regions this problem did not occur. Important fact is that this is a problem in the calculation of the alpha modes and not a problem of the modal expansion technique itself.

The simplified 2D GUINEVERE model is based upon the grid of the XY-plane of the 3D GUINEVERE model. But in this case the model is made symmetrical with respect to the X- and Y-axis. In this way less computational time is required and no asymmetric modes need to be calculated. Since the 2D model has an infinite dimension in the Z-direction the distances in the XY-plane had to be scaled down to obtain a subcritical system. A plot of the mesh of the 2D model with dimensions before scaling down is given in Figure 5.22. In the actual calculation the x and y coordinates were scaled with a factor of 0.66 to obtain a k_{eff} of 0.97502 (using a P_3-expansion with 3rd order scattering). This value of k_{eff} is quite similar to the one foreseen for the subcritical accelerator driven configuration in the GUINEVERE project.

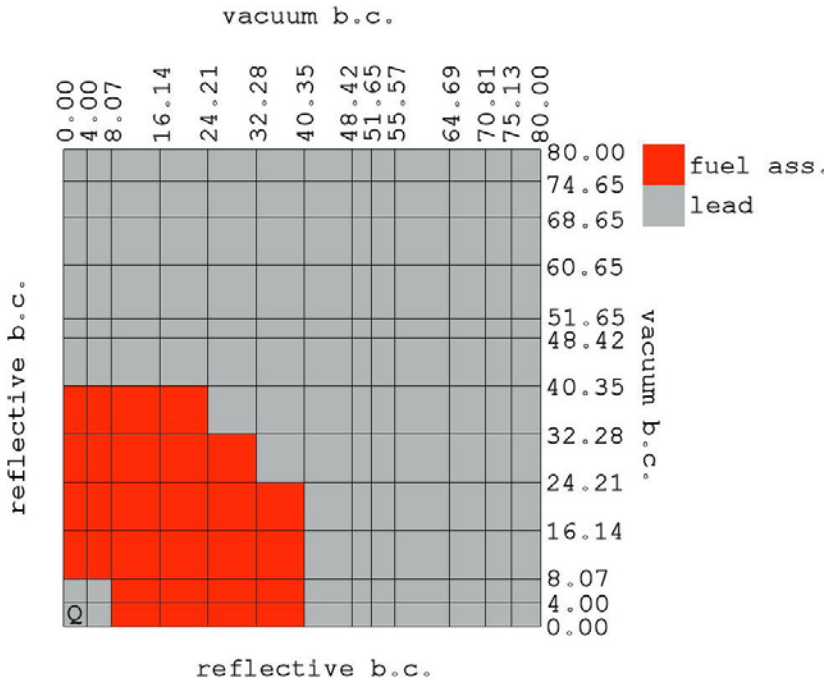

Figure 5.22 Spatial mesh of 2D GUINEVERE model with b.c. and dimensions in *cm* before scaling

The calculations on the 2D simplified GUINEVERE model were performed with a P_3-expansion with third order scattering.

In practice the flux for the system is almost negligible in energy group 9 and 10, because GUINEVERE is a system with a quite fast spectrum, since there is moderator. In section 4.3 it was observed from the time-dependent calculations of the 3D GUINEVERE model that a big difference between the time scale of the physical process in the 9th and 10th energy group and the other 8 energy group exists. The most important processes during the transients in the 2D simplified GUINEVERE model as well as the full 3D model occur on a faster time scale in the first 8 energy groups. It was concluded in section 4.3 that it is desirable to exclude the slower time scales associated with the 9th and 10th energy group from the calculation to determine the relevant alpha modes for the time-dependent flux expansion in an efficient and accurate way.

Only the first 8 energy groups in Table 4.1 were used during the calculations to ensure the calculation of only the relevant modes for the flux expansion. In this way the slow time scales associated with the 9th and 10th energy group are excluded from the calculation. 9 alpha modes are calculated by PHANTOM for the 2D ADS and used in the modal expansion. The fundamental alpha eigenvalue is -74575 s^{-1} and the 9th eigenvalue is -1075828 s^{-1}.

The steady-state problem is solved using a source in the first energy group of unit strength. The steady-state neutron flux obtained by the alpha mode expansion is compared to the reference fixed-source calculation by PHANTOM in Figure 5.23 and Figure 5.24. The solutions are compared over a line in the x-direction in the center of the ADS ($y=0$). Since the system is almost symmetrical this will give a correct representation of the accuracy of the reconstruction. The plotted 1D-graph has been mirrored around $x=0$ to obtain a better graphical interpretation of the flux profile in reality.

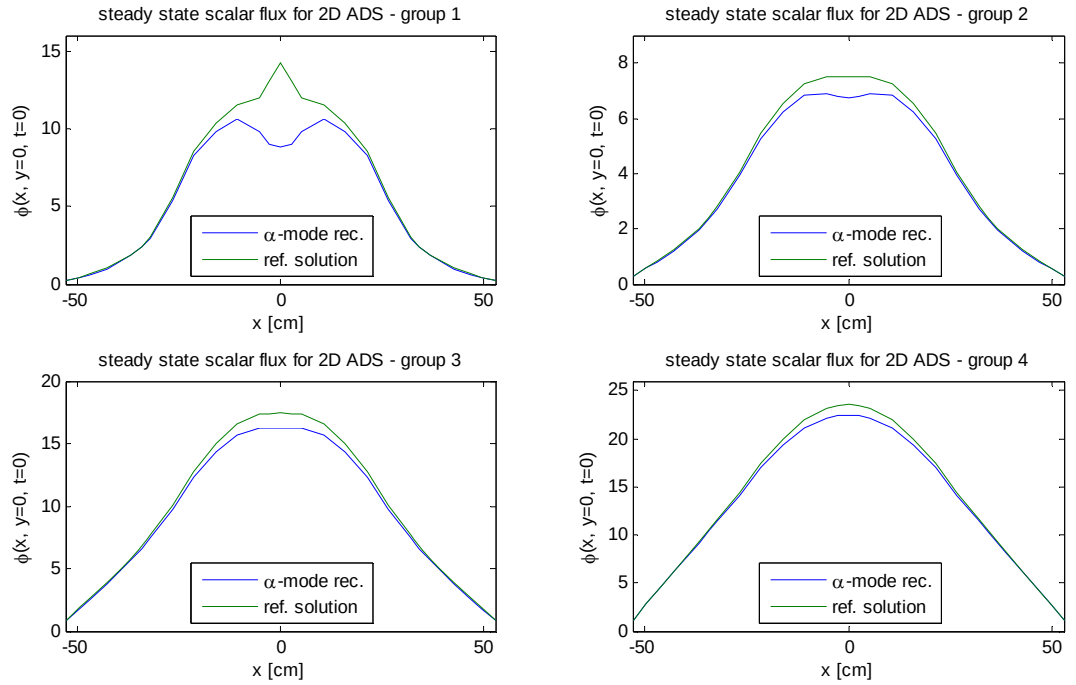

Figure 5.23 Steady state scalar flux reconstruction (group 1-4) of the simplified GUINEVERE model

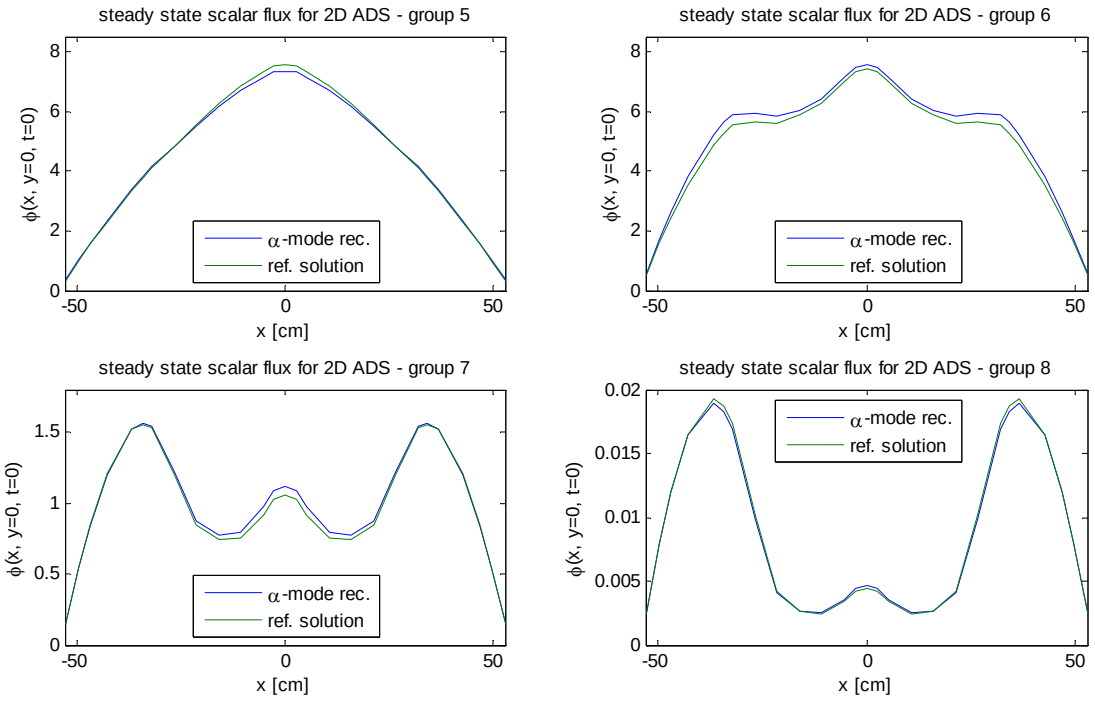

Figure 5.24 Steady state scalar flux reconstruction (group 5-8) of the simplified GUINEVERE model

The high energy source neutrons cause a small peak in the first group flux in the central region of the ADS. The neutrons created during fission also have a high energy (group 1). The neutrons slow down due to scattering. During the first stage of slowing down (group 2-5) the flux is the highest in the fissile fuel region. While the neutrons are slowed down due to scattering more and more neutrons are absorbed by the uranium in the fuel region. The neutrons have less chance of being absorbed in the lead reflector and the lead in the source region than in the uranium, since the absorption cross section of uranium is much larger than of lead. Therefore for the low energy neutrons (group 7, 8) the highest

scalar flux is found in the lead reflector and there is a small increase of the flux inside the source region.

Looking at the alpha mode expansion it should be observed that flux reconstruction compares quite well to the reference steady state flux. The largest difference is not surprisingly found in the group flux of the first energy group at the position of the source region. Also in the other groups there are some small deviations between the reference solution and the alpha mode expansion. But in general the reconstruction of the steady-state flux is still quite accurate. The relative errors, as defined by eq. (5.30), are smaller than 5% for all energy groups except the first (9,09%) and the sixth group (6,31%).

The time-dependent neutron flux of the 2D ADS has also been calculated by PHANTOM in case of turning off the source after operating the ADS under steady-state conditions. Time steps of 10^{-7} *s* were used in this reference calculation. The time-dependent alpha mode reconstruction at the central node of the ADS (*x=0*, *y=0*) using the 9 modes is compared to the reference solution in Figure 5.25 and Figure 5.26.

The general conclusion is that the alpha modes can again reconstruct the time-dependent neutron flux at x=0 accurately except for the very early stages of the transient. For most groups the time-dependent flux reconstruction is better at other positions since x=0 is for most groups obviously already the most difficult position for the steady-state flux reconstruction. In the 8th energy group there is a small difference between the reference solution and the alpha mode reconstruction.

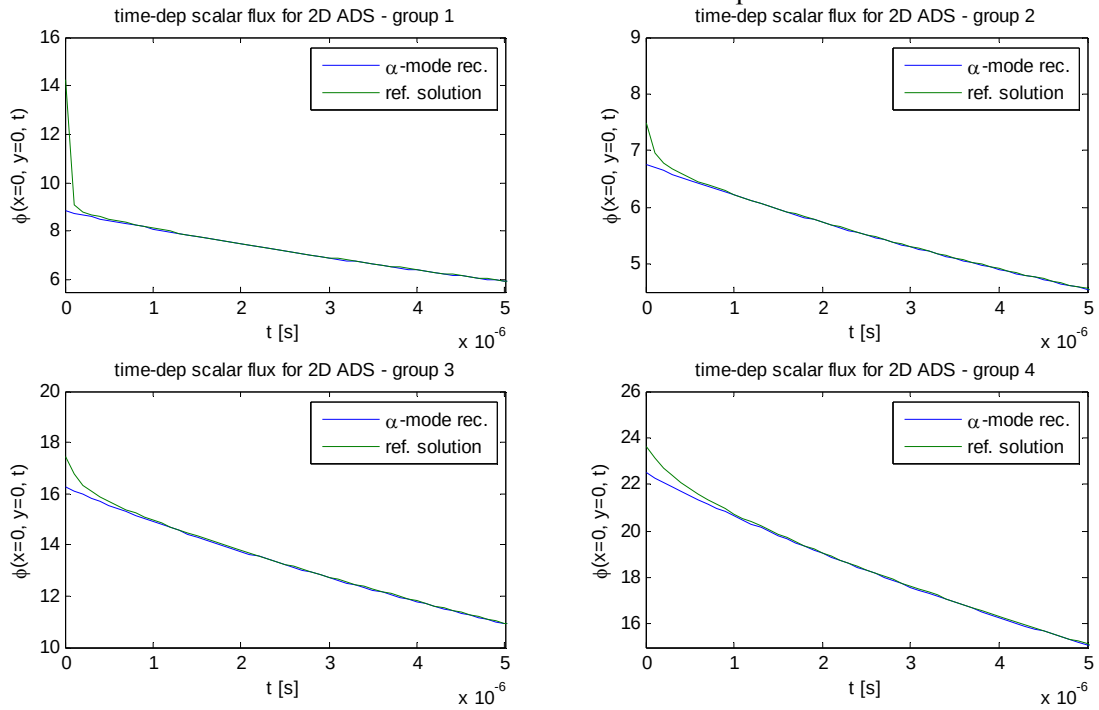

Figure 5.25 Time-dependent scalar flux reconstruction (group 1-4) of the simplified GUINEVERE model after source shutdown

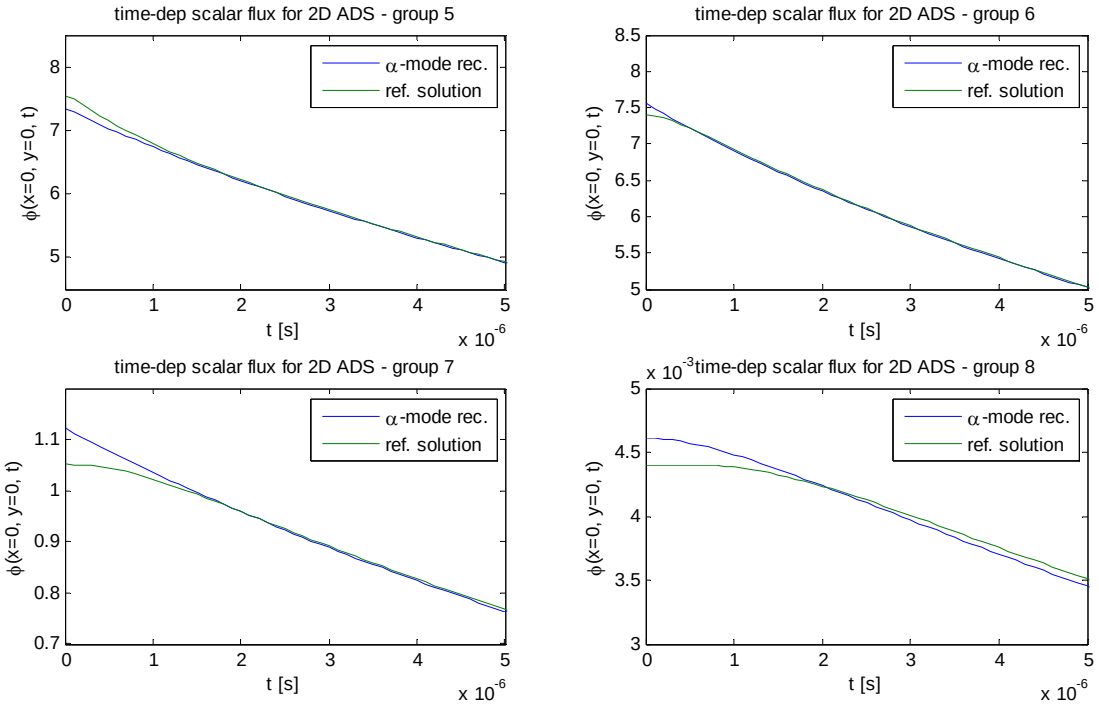

Figure 5.26 Time–dependent scalar flux reconstruction (group 5-8) of the simplified GUINEVERE model after source shutdown

The error in the alpha mode expansion, as defined by eq. (5.30), can be plotted as a function of time for each energy group. In this way the error can be quantified in a better way and the error is evaluated over the whole space domain, instead of one position. The error is plotted in Figure 5.27 for all eight energy groups.

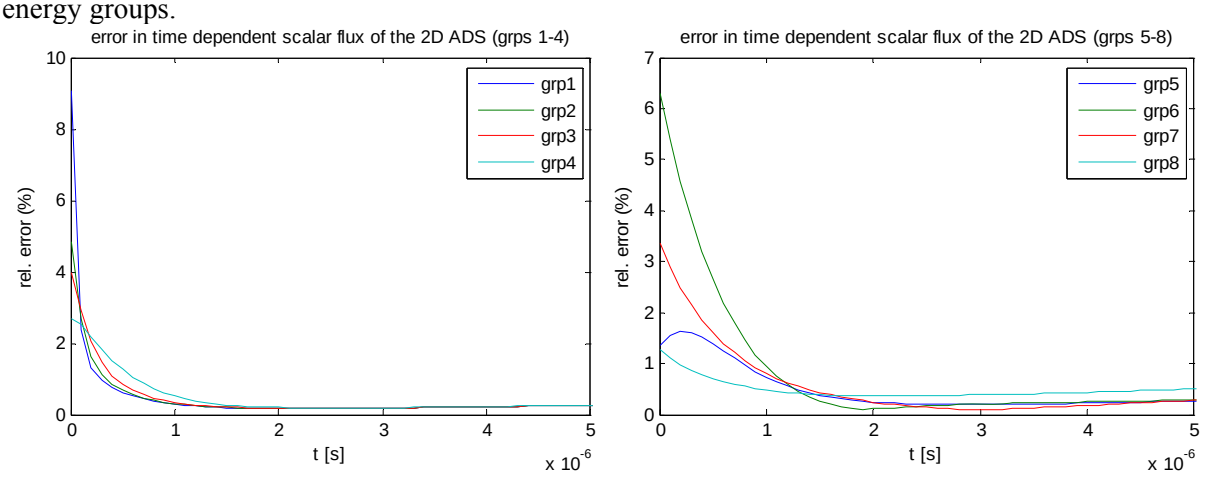

Figure 5.27 Error in flux reconstruction of each group after source shutdown as a function of time

Also from Figure 5.27 it is clear that for the very early stage of the transient there is an error in the group fluxes. But after a short time the solutions become very accurate. There is however a small increase in the error after some time. One possible cause is that a small error is introduced into the reference calculation by PHANTOM due to the use of the implicit time-integration scheme, while the time-integration of the alpha mode expansion coefficients is performed by the analytical expression of eq. (5.21). A small inaccuracy in the magnitude of the fundamental alpha eigenvalue could be another explanation of the slowly increasing error at the later stage of the transient.

In the end it can be concluded that also a more complex 2D ADS-model using a considerable amount of energy groups can be described properly by the alpha mode expansion technique. Still the

early stage of the shutdown transient remains difficult to reconstruct since more alpha modes are needed and those higher alpha modes are difficult to calculate. Also a proper choice of the energy groups is important to calculate the relevant alpha modes for the expansion in an efficient way.

5.7 Conclusions

Alpha modes were used as a basis for a modal expansion method to reconstruct the time-dependent neutron flux. In the alpha mode expansion theory an uncoupled system of ODEs describes the time-dependent behaviour of the system. If the neutron source can be expressed as the product of a constant shape function and a time-dependent amplitude three transient scenarios can be defined. The source can be turned off after operating under steady-state conditions, the source can be turned on with a zero initial flux condition or the reactor can be operated in a pulsed mode, which also has a zero initial condition. Under the assumption that the shape of the neutron source is constant over time exact analytical expressions describe the time-dependent behaviour of the neutron flux reconstruction in the alpha mode expansion theory.

To perform the alpha mode expansion a sufficient number of alpha modes must be determined with sufficient accuracy. In the practical cases studied it was found that the calculation of especially the higher (more than 30~80 modes) alpha modes often became numerically inaccurate. In some cases eigenvalues are skipped during the calculation, leading to a different order of the alpha eigenvalues in the forward and adjoint calculation. Also the difference between the forward and adjoint eigenvalue of the same mode tends to become larger for the higher modes. For the calculation of the alpha modes in 2D the coarseness of the mesh can also limit the accuracy of the higher alpha modes with rapid variations over space. Finally the solution of the multi-group problem only converges very slowly and consequently a lot of computational time is required to calculate a significant number of alpha modes.

The alpha mode expansion theory was used to study three different ADS models. A 1D ADS model, a 2D ADS model and a 2D simplified model of GUINEVERE. The first two models were studied with a one- and three energy group discretization. The simplified GUINEVERE model was studied with a 10 energy group discretization.

The general conclusion is that the alpha mode expansion technique works quite well to describe the time-dependent neutron flux in all three reactor models. The biggest difficulties were encountered during the steady-state fixed source solution and the very early stage of the shutdown transient. During a start-up of the source or in an ADS operating in pulsed mode the largest contribution to the error is created during a very short moment after starting up the source. More alpha modes are required for a correct reconstruction of the time-dependent neutron flux in these cases. After the very early stages of a shutdown transient the alpha mode expansion leads to very accurate results with errors of often far less than 1%.

The alpha mode expansion method should also be usable in 3D, since extension from 2D to 3D is straightforward. The greatest limitation is the computational time required to calculate the alpha modes.

6 Alternative methods: Lambda modes and POD

In this chapter two alternative bases for modal expansion methods are explored. First of all the lambda modes are investigated as a possible basis for the modal expansion technique describing the time-dependent behaviour of an accelerator driven system.

A second alternative method is the proper orthogonal decomposition (POD), in combination with the Galerkin projection. The POD can be used to create new basis function by sampling a known time-dependent solution of the neutron transport problem. Theory for the use of the POD in neutron transport problems with a source term is derived in this chapter. The method has not been applied to time-dependent problems. The programming of a code to do this would have been a too comprehensive task for this thesis.

6.1 Lambda mode expansion theory

Besides the alpha modes used in chapter 5 as a basis for a modal expansion method it is also possible to use another basis for the modal expansion method. One possible candidate is the use of lambda modes, introduced in section 3.5.1, as a basis for a modal expansion method to describe the time-dependent behaviour of an accelerator driven system. In this section the theoretical background of a modal expansion of the flux in terms of lambda modes is treated.

6.1.1 Biorthogonality of the lambda modes

The orthogonality relation of the lambda modes will be used during the derivation of an expression describing the time-dependent coefficients in the modal expansion of the neutron flux. The orthogonality relation is derived in appendix B and it is given by

$$\left(\frac{1}{\lambda_l}-\frac{1}{\lambda_m^\dagger}\right)\left\langle \psi_m^\dagger, \mathbf{F}\psi_l \right\rangle = 0 . \tag{6.1}$$

Either the inner product $\left\langle \psi_m^\dagger, \mathbf{F}\psi_l \right\rangle$ is equal to zero or λ_l must be equal to $\lambda_m{}^\dagger$ or both. In absence of degenerate eigenvalues the adjoint λ-mode $\psi_m^\dagger$ is orthogonal to $\mathbf{F}\psi_l$.

This biorthogonality relation of the lambda modes involves the fission operator $\mathbf{F}$ making the biorthogonal properties of the lambda modes slightly more inconvenient than the biorthogonal properties of the alpha modes.

6.1.2 The lambda mode expansion

In the modal approximation the neutron flux is expanded as a sum of lambda modes with time-varying coefficients

$$\psi\left(\vec{r},E,\hat{\Omega},t\right)=\sum_{l=1}^{M}B_l\left(t\right)\psi_l\left(\vec{r},E,\hat{\Omega}\right). \tag{6.2}$$

The modal approximation is substituted into the transport equation, given by eq. (3.2), and the inner product with $\psi_m^\dagger$ is taken resulting in

$$\sum_{l=1}^{M}\frac{dB_l\left(t\right)}{dt}\left\langle \psi_m^\dagger, V^{-1}\psi_l \right\rangle = \sum_{l=1}^{M}B_l\left(t\right)\left\langle \psi_m^\dagger, \left[\mathbf{F}-\mathbf{L}\right]\psi_l \right\rangle + \left\langle \psi_m^\dagger, Q\left(t\right) \right\rangle . \tag{6.3}$$

The definition of the lambda eigenvalue problem, given by eq. (3.35), can be used to rewrite the transport operator $\mathbf{L}$

$$\sum_{l=1}^{M}\frac{dB_l(t)}{dt}\left\langle \psi_m^{\dagger}, V^{-1}\psi_l \right\rangle = \sum_{l=1}^{M} B_l(t)\left(1-\frac{1}{\lambda_l}\right)\left\langle \psi_m^{\dagger}, \mathbf{F}\psi_l \right\rangle + \left\langle \psi_m^{\dagger}, Q(t) \right\rangle. \tag{6.4}$$

Since application of the transport operator $\mathbf{L}$ is difficult to include it is very convenient that $\mathbf{L}$ can now be excluded from the determination of $B_l(t)$.

From the biorthogonal properties of the lambda modes it follows for the non-degenerate case that $\left\langle \psi_m^{\dagger}, \mathbf{F}\psi_l \right\rangle = 0$ if $m \neq l$. After using this property eq. (6.4) reduces to

$$\sum_{l=1}^{M}\frac{dB_l(t)}{dt}\left\langle \psi_m^{\dagger}, V^{-1}\psi_l \right\rangle = B_m(t)\left(1-\frac{1}{\lambda_m}\right)\left\langle \psi_m^{\dagger}, \mathbf{F}\psi_m \right\rangle + \left\langle \psi_m^{\dagger}, Q(t) \right\rangle. \tag{6.5}$$

A system of equations showing great similarities was found by González [2010]. They studied the lambda mode expansion of an (initially) critical system with perturbed operators and without a source and found a similar structure of the system of equations describing the expansion coefficients.

A system of coupled ordinary differential equations must be solved to determine the time dependent coefficients in the lambda mode expansion. This makes the time integration of the coefficients in the lambda mode expansion mathematically slightly more complicated than the alpha mode expansion. Calculation of the coefficients also involves applying the fission operator once for each lambda mode in the expansion.

The lambda modes can also be used to reconstruct the steady state flux for a problem with a constant source Q_0. In this case $\frac{dB_l(t)}{dt} = 0$, so B_m is determined by:

$$B_m = -\frac{\left\langle \psi_m^{\dagger}, Q_0 \right\rangle}{\left(1-\frac{1}{\lambda_m}\right)\left\langle \psi_m^{\dagger}, \mathbf{F}\psi_m \right\rangle} \tag{6.6}$$

These values B_m are used as an initial condition for a transient calculation where the source is shut down after operating the ADS under steady state conditions. Otherwise $B_m(0)$ will be equal to zero in case of starting up the ADS.

6.2 Numerical procedure

The numerical procedures required to perform the expansion with lambda modes are for a great part similar to the numerical procedures used in the alpha mode expansion technique. Most of the inner products are calculated in the same way. Compared to the alpha mode expansion there are two important differences. The first one deals with the angular and energy dependence of the inner product containing the fission operator. The second one arises from the time-integration of the system of coupled ordinary differential equations. For the three time-dependent scenarios defined in section 5.3 an implicit Euler scheme is used to solve $B_m(t)$.

6.2.1 Angular and energy dependence of the fission operator

The treatment of the energy and angular dependence in the calculation of $\left\langle \psi^{\dagger}, \mathbf{F}\psi \right\rangle$ in the lambda mode expansion is slightly different from the other inner products encountered in this thesis. These differences are caused by the application of the fission operator $\mathbf{F}$, which requires integration of the flux ψ over the angle $\hat{\Omega}'$ and energy E'. In this subsection an evaluation of the integration over the

angle and energy of the inner product $\left\langle \psi^{\dagger}, \mathbf{F}\psi \right\rangle$ is made. The spatial integration of $\left\langle \psi^{\dagger}, \mathbf{F}\psi \right\rangle$ is performed in the same way as the spatial integration of the alpha modes in section 5.2.1.

The fission operator is defined by

$$\mathbf{F}\psi = \frac{\chi_g}{4\pi}\sum_{g'=1}^{G} \nu\Sigma_{f,g'} \int_{4\pi} \psi_{g'}\left(\hat{\Omega}'\right) d\hat{\Omega}' . \tag{6.7}$$

Without spatial integration the inner product is given by

$$\left\langle \psi^{\dagger}, \mathbf{F}\psi \right\rangle_{E,\hat{\Omega}} = \sum_{g=1}^{G} \int_{4\pi} \psi_g^{\dagger}\left(\vec{r},\hat{\Omega}\right) d\hat{\Omega} \frac{\chi_g}{4\pi} \sum_{g'=1}^{G} \nu\Sigma_{f,g'} \int_{4\pi} \psi_{g'}\left(\vec{r},\hat{\Omega}'\right) d\hat{\Omega}' . \tag{6.8}$$

The group flux is expanded in terms of the spherical harmonics polynomials $Q_i\left(\hat{\Omega}\right)$ introduced in chapter 3

$$\psi_g\left(\vec{r},\hat{\Omega}\right) = \sum_i \psi_{g,i}\left(\vec{r}\right) Q_i\left(\hat{\Omega}\right). \tag{6.9}$$

To solve the inner product the integral of $Q_i\left(\hat{\Omega}\right)$ over $\hat{\Omega}$ must be solved. Using the fact that $Q_0\left(\hat{\Omega}\right) = Q_0 = \sqrt{\frac{1}{4\pi}}$ is the only constant function of the spherical harmonics polynomials and applying the orthogonality relations of the spherical harmonics polynomials, the integral is found to be

$$\int_{4\pi} Q_i\left(\hat{\Omega}\right) d\hat{\Omega} = \sqrt{4\pi} \int_{4\pi} Q_i\left(\hat{\Omega}\right) Q_0\left(\hat{\Omega}\right) d\hat{\Omega} = \sqrt{4\pi}\delta_{i0} . \tag{6.10}$$

$\left\langle \psi^{\dagger}, \mathbf{F}\psi \right\rangle_{E,\Omega}$ is now rewritten in terms of the spherical harmonics polynomials $Q_i\left(\hat{\Omega}\right)$

$$\left\langle \psi^{\dagger}, \mathbf{F}\psi \right\rangle_{E,\Omega} = \sum_{g=1}^{G} \sum_i \psi_{g,i}^{\dagger}\left(r\right) \int_{4\pi} Q_i\left(\hat{\Omega}\right) d\hat{\Omega} \frac{\chi_g}{4\pi} \sum_{g'=1}^{G} \nu\Sigma_{f,g'} \sum_j \psi_{g',j}\left(r\right) \int_{4\pi} Q_j\left(\hat{\Omega}'\right) d\hat{\Omega}' \tag{6.11}$$

and integrated over the angle

$$\left\langle \psi^{\dagger}, \mathbf{F}\psi \right\rangle_{E,\Omega} = \sum_{g=1}^{G} \psi_{g,0}^{\dagger}\left(r\right) \chi_g \sum_{g'=1}^{G} \nu\Sigma_{f,g'} \psi_{g',0}\left(r\right) . \tag{6.12}$$

So a relatively simple expression is obtained and, as mentioned before, the spatial integration can be performed as usual.

6.2.2 Time integration of the lambda mode expansion coefficients

The time evolution of the coefficients $B_m\left(t\right)$ can be evaluated by an Euler implicit time-integration scheme if the initial conditions $B_m\left(0\right)$ are known. Implicit Euler time-integration is relatively easy to implement and it is numerically stable for each time-step size Δt. Equation (6.5) can be written in a matrix-vector notation

$$\mathbf{A}\frac{d\underline{B}}{dt} = \mathbf{M}\underline{B} + \underline{\underline{Q}} . \tag{6.13}$$

The coefficients of the matrix $\mathbf{A}$ are given by $A_{ml} = \left\langle \psi_m^{\dagger}, V^{-1}\psi_l \right\rangle$, $\mathbf{M}$ is a diagonal matrix with coefficients: $M_{mm} = \left(1 - \frac{1}{\lambda_m}\right)\left\langle \psi_m^{\dagger}, \mathbf{F}\psi_m \right\rangle$ and the vector $\underline{\underline{Q}}$ is given by: $\underline{\underline{Q}} = \left\langle \psi_m^{\dagger}, Q\left(t\right) \right\rangle$.

Now an implicit Euler time-integration scheme is applied to obtain

$$\mathbf{A}\frac{\underline{B}^{i+1}-\underline{B}^{i}}{\Delta t}=\mathbf{M}\underline{B}^{i+1}+\underline{\underline{Q}}^{i+1}, \tag{6.14}$$

and upon rewriting

$$\left(\frac{\mathbf{A}}{\Delta t}-\mathbf{M}\right)\underline{B}^{i+1}=\frac{\mathbf{A}}{\Delta t}\underline{B}^{i}+\underline{\underline{Q}}^{i+1} \tag{6.15}$$

This system can be solved by MATLAB using Gaussian elimination.

6.2.3 Stability issues

In practice difficulties were encountered with the stability of the time-integration of the system of ODEs. If the system is studied when the source is turned off after operating under steady-state conditions the system of ODEs (6.13) reduces to:

$$\frac{d\underline{B}}{dt}=\left[\mathbf{A}^{-1}\mathbf{M}\right]\underline{B} \tag{6.16}$$

It is known from standard differential equation books that the system is unstable if $\mathbf{A}^{-1}\mathbf{M}$ has one or more eigenvalues with a positive real part [Borrelli & Coleman., 1998]. In practice this problem arose for the cases studied in section 6.3 when a large number of lambda modes was used. Of course in theory this should not be anticipated for a subcritical system. The most plausible explanation can be found in numerical errors in the determination of especially the higher lambda modes leading to an unstable system due to the coupling between the modes.

For the actual transient calculations with the lambda modes this instability did not pose any real problems since in the cases studied most of the information of the lambda mode expansion is contained in the fundamental mode and perhaps a few other dominant modes. But when also the higher modes are used the choice of a small time step Δt often caused the generation of unstable results due to the instability of the underlying system. For systems, which also require the higher modes for the flux reconstruction, this instability is a serious problem.

6.3 Results: Lambda mode expansion in the 1D ADS model

The lambda modes expansion technique has been applied to the same 1D ADS model that was studied with the alpha modes in section 5.4. The lambda modes are used to reconstruct the steady-state solution and the solution during a transient using a 1-group and a 3-group energy discretization. Results are compared with a reference solution and the 3-groups case results are also compared with the alpha mode reconstruction in subsection 5.4.3.

6.3.1 1-group results

The time-evolution of the 1D ADS model has been studied for the scenario of an ADS initially operating under steady state conditions. At $t=0$ the source is switched off.

80 eigenvectors of the lambda eigenvalue problem were calculated by PHANTOM with the Arnoldi method. The first 56 of these 80 eigenvectors correspond to the actual lambda modes of the system. For the last 24 eigenvectors the eigenvalues were some random, practically zero, values (in the order of 10^{-16} instead of 10^{-3}) and contained imaginary components (also in the order 10^{-16}). Higher lambda modes than these 56 either do not exist or could not be calculated by PHANTOM.

The instability of the time-integration of the system of ODEs, described in section 6.2.3, occurred when more than the first 16 lambda modes of the 56 lambda modes were used in the modal expansion.

As a consequence the reconstruction of the scalar neutron flux was performed using the expansion in terms of the first 16 lambda modes and the reference solution have been plotted in Figure 6.1 for the steady state situation (at $t = 0$) and the end of the time-domain of the calculation ($t = 10^{-4}\,s$).

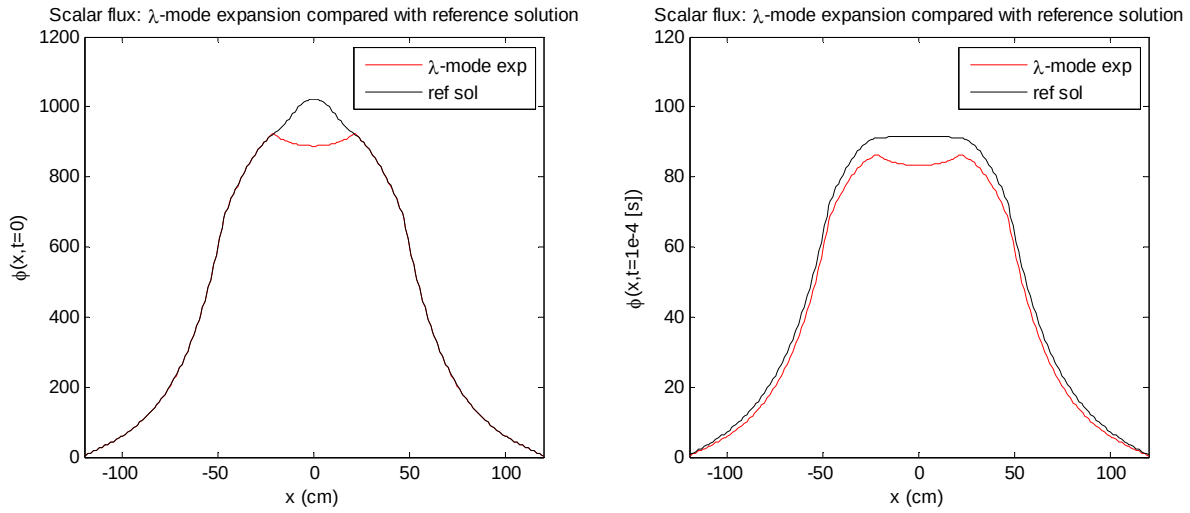

Figure 6.1 Reconstructed scalar flux and reference flux of 1D ADS at $t = 0\ s$ and $t = 0.0001\ s$

Except for the source-region, without any fissile material, the lambda modes expansion agrees well with the reference solution for the steady state situation. After $10^{-4}\ s$ the lambda modes expansion slightly deviates from the reference solution.

Figure 6.2 shows the difference in the lambda mode reconstruction of the steady-state flux and the time-dependent flux when only the fundamental lambda mode is used or 16 lambda modes are used in the expansion. Adding more modes than the fundamental mode in the expansion only leads to small changes in the steady-state reconstruction. For the description of the time-dependent flux the addition of more modes only leads to very small changes in the amplitude of the flux, but the actual characteristics of the transient remain the same.

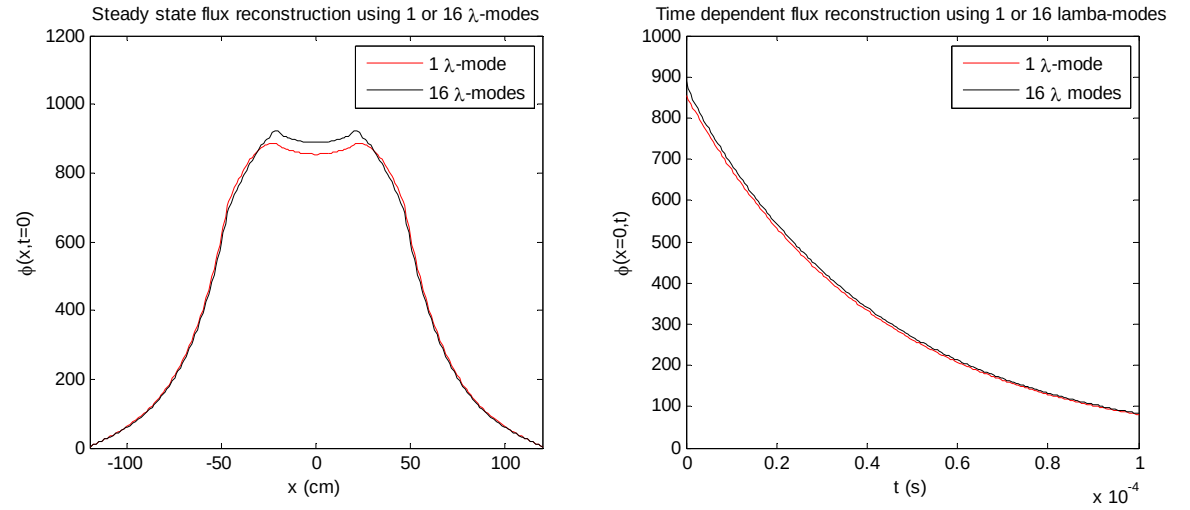

Figure 6.2 Steady-state and time-dependent (x=0) scalar flux reconstruction of the 1D ADS model using 1 or 16 λ-modes

The time-dependent scalar flux reconstruction using 16 lambda modes is compared with the reference solution in Figure 6.3 at two different positions, $x = 0$ *cm* and $x = 50$ *cm*.

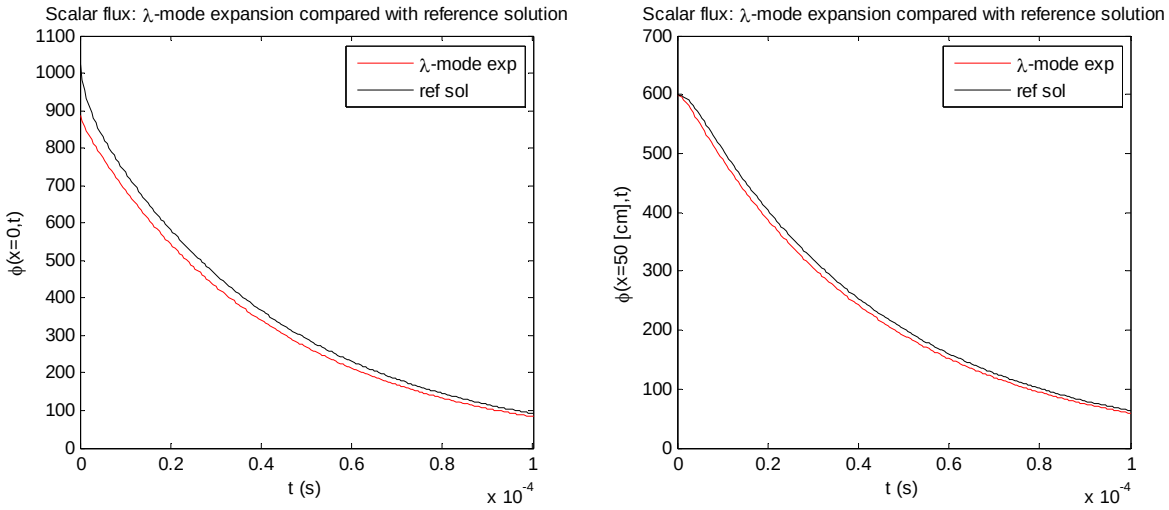

Figure 6.3 Time evolution of reference and reconstructed scalar flux at $x = 0$ *cm* and $x = 50$ *cm*

The time dependent neutron flux obtained by the lambda modes expansion follows the time-dependent reference solution closely. At $x = 50$ *cm* both solutions are basically equal to each other at $t = 0$. The relative difference between the two solutions is only 0,0294 %. It is quite remarkable that after some time the difference between the two solutions becomes larger. At $t = 5 \cdot 10^{-5}$ *s* the relative difference between the two values is a significant 4,98 %. After 10^{-4} *s* the relative difference has increased to 6,73 %.

For the 1-group case the lambda modes can describe the steady state solution of the problem quite well except for the non-fissile source region. The time-integration leads to larger errors. So for an exact representation of the time-evolution the lambda modes seem less useful than the alpha modes. As shown in chapter 5 the alpha modes can reconstruct the solution of this problem with a very high accuracy. However the lambda modes still give a reasonable estimate of the neutron flux and are much cheaper to calculate than the alpha modes. But especially the higher lambda modes sometimes lead to an unstable coupled system of ODEs which makes the solution physically unreliable. However in this particular case the higher modes were not so relevant for the lambda mode reconstruction. It will be interesting to check the accuracy of the lambda mode expansion technique in a multi-group problem.

6.3.2 3-group results

The transient scenario of turning off the source after operating under steady-state conditions has also been studied with the lambda modes expansion using 3 energy groups. For the 3-group problem also 80 eigenvectors of the lambda eigenvalue problem were calculated, of which, equal in the 1 group-case, 56 could be qualified as the lambda modes of the system. In the 3-group case the use of more than the first 14 lambda modes caused the time-integration of the system of ODEs to become unstable. In the end 14 lambda modes are used in the reconstruction of the flux. The flux reconstruction after turning off the source is compared with a reference solution by PHANTOM and with the alpha modes reconstruction. The steady-state neutron flux, which is equal to the neutron flux of the time-dependent problem at $t = 0$ is plotted in Figure 6.4 for the different energy groups.

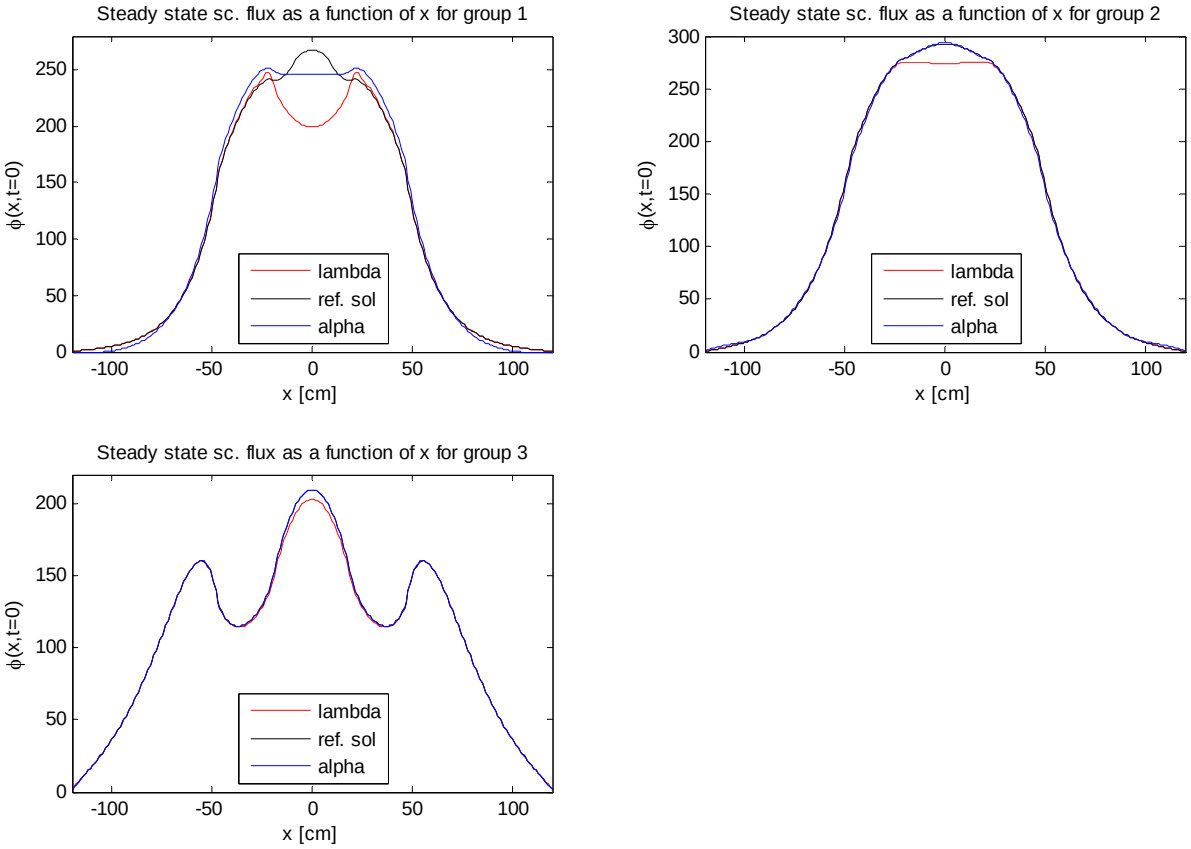

Figure 6.4 Comparison of the α- and λ-mode expansion and the reference solution of the steady-state scalar flux of the 1D ADS for 3 energy groups.

The flux generated by the lambda mode expansion, using the first 14 lambda modes, for most of the space domain agrees very well with the reference neutron flux. Inside the non-fissile source region the lambda mode expansion leads to worse results. This also occurred in the 1-group case studied in the previous subsection.

In the first energy group, which contains the highest neutron energies, the source neutrons are created. Also the alpha modes have small difficulties with a correct representation of the flux in this first energy group. For the higher groups the alpha modes expansion gives good results over the whole spatial domain. The lambda modes on the other hand still show small deviations from the reference calculation in the higher energy groups.

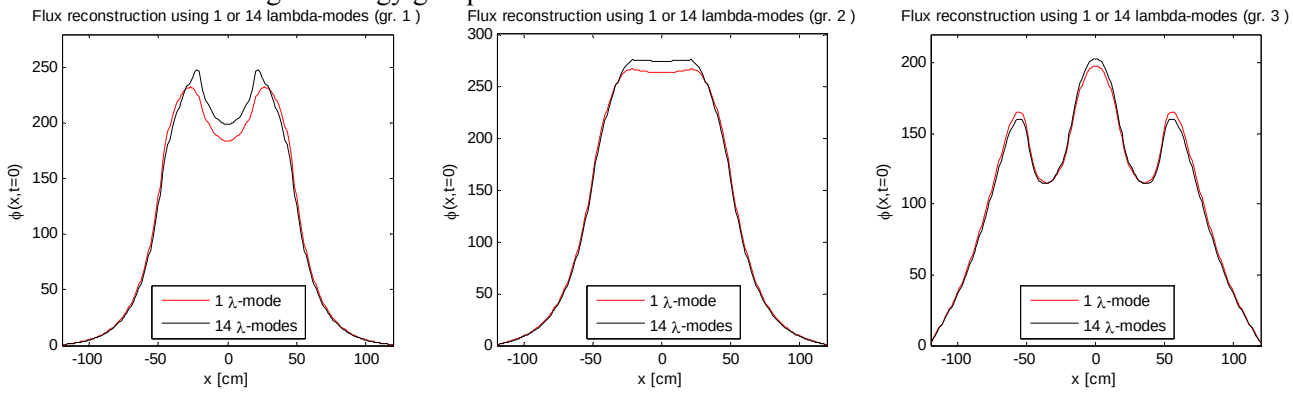

Figure 6.5 Modal expansion of the 3-group steady-state scalar flux of 1D ADS using 1 or 14 λ-modes

Figure 6.5 shows the difference in the lambda modes reconstruction of the steady state flux when only the fundamental mode is used or all 14 modes are used.

Just as with the one group case the fundamental lambda mode is of great importance in the 3-groups case. The higher modes are not very important in the reconstruction and the difference between 14 modes or only the fundamental mode for the time-dependent behaviour is also very small.

Figure 6.6 shows the time-evolution of the scalar neutron flux at the center of the ADS ($x = 0$ *cm*) for the different energy groups. Again 14 lambda modes were used in the reconstruction.

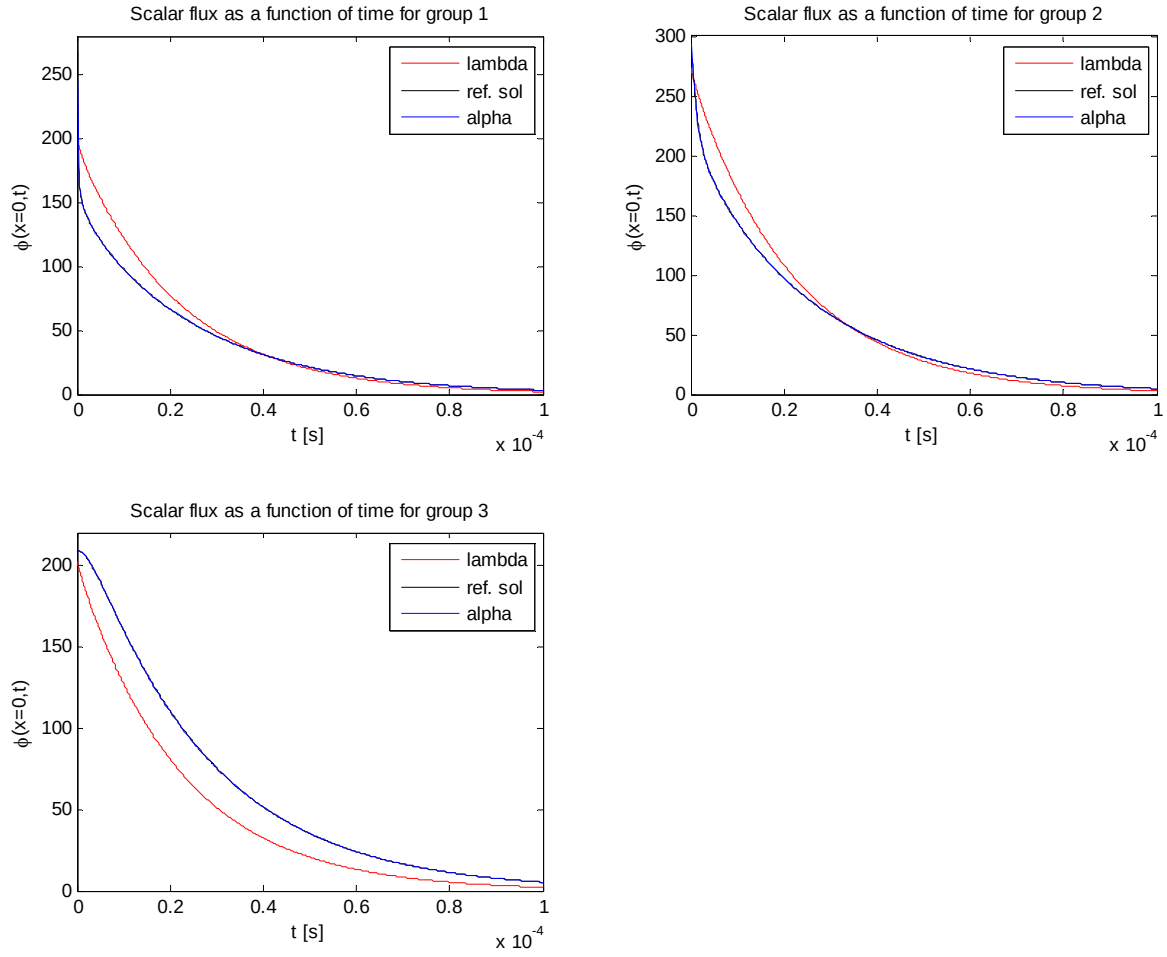

Figure 6.6 Time evolution of steady state scalar neutron flux of 1D ADS for 3 groups at $x = 0$ *cm*

The description of time evolution by the lambda mode expansion technique gives a rough estimate of the time dependent behaviour of the ADS. In all three energy groups it is however not really an accurate reconstruction of the neutron flux. Obviously the alpha mode expansion is a much better method to describe the time-dependent behaviour of the system.

Figure 6.7 shows the scalar neutron flux after 10^{-4} *s*. The difference between the lambda mode reconstruction and the reference solution is large. The alpha mode expansion on the other hand does give a very accurate result and is much more suitable to describe the time-dependent behaviour in an accurate way.

One big advantage of the lambda modes is that the calculation of 80 lambda modes of the system takes around 4 minutes, while the determination of 80 alpha modes requires a bit less than 8 hours of computational time. As mentioned in section 3.5.2 the large difference in computational time occurs because during the determination of the lambda modes the fission operator occurs in the right-hand side of the fixed source problem.

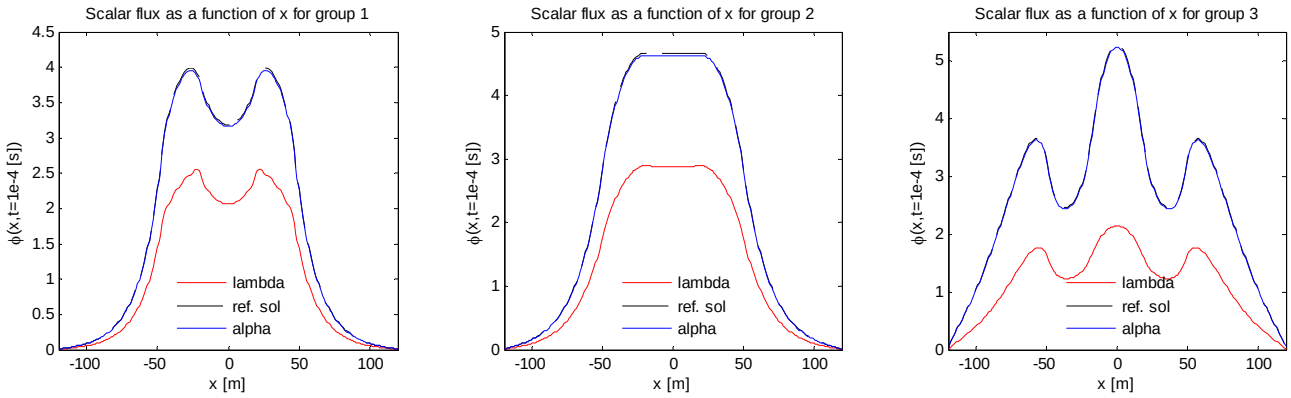

Figure 6.7 Scalar flux reconstruction of 1D ADS at 0.1 *ms* after source shutdown for 3 groups

Looking at the results it is obvious that the lambda mode expansion might only be used as a very rough estimate of the time-dependent behaviour of the system. The fundamental lambda mode is of great importance in the flux reconstruction. The addition of higher modes only leads to minor changes in the flux reconstruction and using more than 14 modes leads to instability of the system of ODEs describing the time-integration of the expansion coefficients.

Despite the larger computational effort due to the determination of the alpha modes the alpha mode expansion is a much better candidate for an accurate description of the time-dependent behaviour of the system.

6.4 Proper Orthogonal Decomposition

Proper orthogonal decomposition (POD), in combination with the Galerkin projection, has been used in many applications in science and engineering to represent the dynamics of large-scale systems by a smaller number of degrees of freedom. An interesting example of the POD combined with the Galerkin projection can be found in the work by Fang [2009] in the field of ocean modelling. The POD, combined with the Galerkin projection, might also be a way to describe the dynamic behaviour of an accelerator driven system.

6.4.1 Basis functions

The POD can find an optimal set of orthogonal basis functions to describe the dominant components of the dynamics of a large-scale system by only a finite number of these basis functions. In practice often only surprisingly few of the POD basis vectors are required.

A certain variable Z, for instance the neutron flux, can be described by a set of snapshots $Z_k(\mathbf{x},t_k)$ sampled at different moments in time: $[t,...,t_k,...,t_K]$. Here K is the number of snapshots of uniform weight, $\mathbf{x}$ are usually the spatial variables and in reactor physics it may also include energy and angle. In general snapshots might also be obtained by sampling with respect to variations of another variable than time.

The average of the ensemble of snapshots is defined by

$$\bar{Z}(\mathbf{x}) = \frac{1}{K}\sum_{k=1}^{K} Z_k(\mathbf{x},t_k). \tag{6.17}$$

Now the deviation of $Z_k(\mathbf{x},t_k)$ from the mean is taken

$$z_k(\mathbf{x},t_k) = Z_k(\mathbf{x},t_k) - \bar{Z}(\mathbf{x}). \tag{6.18}$$

Using $z_k(\mathbf{x},t_k)$, the covariance matrix $\mathbf{C}$ can be calculated. Its coefficients $\mathbf{C}_{k,l}$ are determined by

$$\mathbf{C}_{k,l} = \frac{1}{K}\left\langle z\left(\mathbf{x},t_k\right), z\left(\mathbf{x},t_l\right)\right\rangle_{\mathrm{x}} \qquad \text{for } l,k = 1.....K\,. \tag{6.19}$$

The K*x*K-matrix $\mathbf{C}$ has *K* real and positive eigenvalues λ_j. The eigenvectors $y_j\left(k\right)$ of $\mathbf{C}$ are sorted in descending order with respect to λ_j. Now the POD bases can be calculated as a linear combination of the snapshots

$$\Phi_j\left(\mathbf{x}\right) = \sum_{k=1}^{K} y_j\left(k\right) z\left(\mathbf{x},t_k\right). \tag{6.20}$$

The orthonormal POD basis vectors $\hat{\Phi}_j\left(\mathbf{x}\right)$ are obtained by normalization of $\Phi_j\left(\mathbf{x}\right)$

$$\hat{\Phi}_j\left(\mathbf{x}\right) = \frac{\Phi_j\left(\mathbf{x}\right)}{\sqrt{\left\langle \Phi_j\left(\mathbf{x}\right), \Phi_j\left(\mathbf{x}\right)\right\rangle_{\mathbf{x}}}}. \tag{6.21}$$

The POD basis vectors $\hat{\Phi}_j\left(\mathbf{x}\right)$ for a certain model variable *Z* have been constructed and can be used in the Galerkin projection. An alternative method to construct similar basis vectors is the singular value decomposition (SVD).

6.4.2 Galerkin Projection of the neutron transport equation

The neutron flux can be written in terms of the average of the ensemble of snapshots $\bar{\psi}\left(\vec{r},E,\hat{\Omega}\right)$ plus a linear combination of the POD basis functions $\Phi_{n,\psi}\left(\vec{r},E,\hat{\Omega}\right)$

$$\Psi\left(\vec{r},E,\hat{\Omega},t\right) = \bar{\psi}\left(\vec{r},E,\hat{\Omega}\right) + \sum_n A_{n,\psi}\left(t\right)\Phi_{n,\psi}\left(\vec{r},E,\hat{\Omega}\right). \tag{6.22}$$

The expansion is substituted into the neutron transport equation to obtain

$$\frac{1}{V}\frac{d}{dt}\left(\bar{\psi} + \sum_n A_{n,\psi}\left(t\right)\Phi_{n,\psi}\right) = \left[\mathbf{F}-\mathbf{L}\right]\left(\bar{\psi} + \sum_n A_{n,\psi}\left(t\right)\Phi_{n,\psi}\right) + Q\,. \tag{6.23}$$

Use $\frac{d\bar{\psi}}{dt} = 0$, bring *v* to the right hand side of the equation and take the inner product (by integrating over energy, angle and volume) with $\Phi_{m,\psi}$. This is the so-called Galerkin Procedure, which consists of using the same basis functions of the expansion in the projection. A general treatment of the Galerkin procedure is given by Strang [1973]. The projections results in

$$\left\langle \sum_n \frac{dA_{n,\psi}\left(t\right)}{dt}\Phi_{n,\psi}, \Phi_{m,\psi}\right\rangle = \left\langle V\left[\mathbf{F}-\mathbf{L}\right]\left(\bar{\psi} + \sum_n A_{n,\psi}\left(t\right)\Phi_{n,\psi}\right), \Phi_{m,\psi}\right\rangle + \left\langle VQ, \Phi_{m,\psi}\right\rangle. \tag{6.24}$$

Since $A_{n,\psi}\left(t\right)$ does not depend on energy, angle and position it can be taken out of the integral and the orthonormality $\left\langle \Phi_{n,\psi}, \Phi_{m,\psi}\right\rangle = \delta_{mn}$ of the POD basis functions is used

$$\frac{dA_{m,\psi}\left(t\right)}{dt} = \left\langle V\left[\mathbf{F}-\mathbf{L}\right]\left(\bar{\psi} + \sum_n A_{n,\psi}\left(t\right)\Phi_{n,\psi}\right), \Phi_{m,\psi}\right\rangle + \left\langle VQ, \Phi_{m,\psi}\right\rangle \tag{6.25}$$

The initial condition $A_{m,\psi}\left(0\right)$ is given by

$$A_{m,\psi}\left(0\right) = \left\langle \left(\Psi\left(t=0\right) - \bar{\psi}\right), \Phi_{m,\psi}\right\rangle. \tag{6.26}$$

The time-dependent coefficients $A_{m,\psi}\left(t\right)$ in the expansion of the neutron flux in terms of the POD basis functions are described by a set of ordinary differential equations. For the determination of the coefficients $A_{m,\psi}\left(t\right)$ the fission and transport operators, $\mathbf{F}$ and $\mathbf{L}$, have to be applied several times.

6.4.3 Steady-state flux reconstruction by POD basis functions

The POD basis functions have been determined for a source shutdown in the 1D ADS model introduced in section 5.4. A reference solution of the neutron flux is sampled to obtain the snapshots. The used reference solution of the scalar neutron flux using a three group energy discretization in case of a source shutdown is partially plotted in Figure 5.6, Figure 5.7 and Figure 5.8. 101 snapshots are used, the first one originating from the initial or steady-state flux and the other 100 are the fluxes after each time step. Using these 101 snapshots the POD basis functions were determined using eq. (6.17) till eq. (6.21). The first 5 POD basis functions are plotted in Figure 6.8. The POD basis functions were determined by sampling of a reference solution of the system.

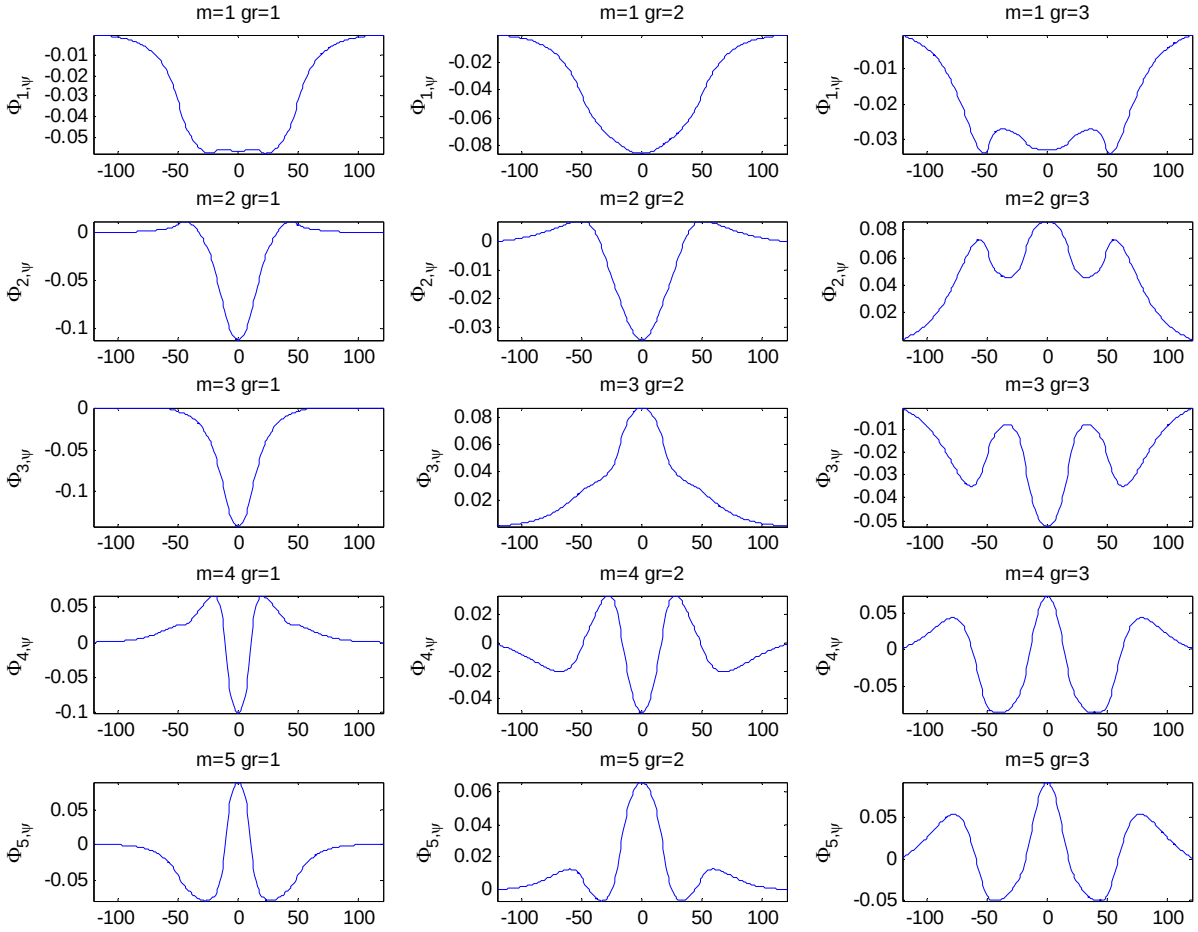

Figure 6.8 Plots of the first 5 POD basis functions of the 1D ADS model for the three energy groups

The POD basis functions have remarkable shapes, but these basis functions can reconstruct the reference steady state flux quite well. The POD basis functions are used to reconstruct the steady state flux of the 1D ADS model. The coefficients $A_{m,\psi}(0)$ were calculated according to eq. (6.26) and the reconstruction was made as in eq. (6.22). The steady state flux using 1, 2 or 5 POD basis functions for the three energy groups are shown in Figure 6.9 and compared with the original steady-state flux, where the sampling of the basis functions was based upon.

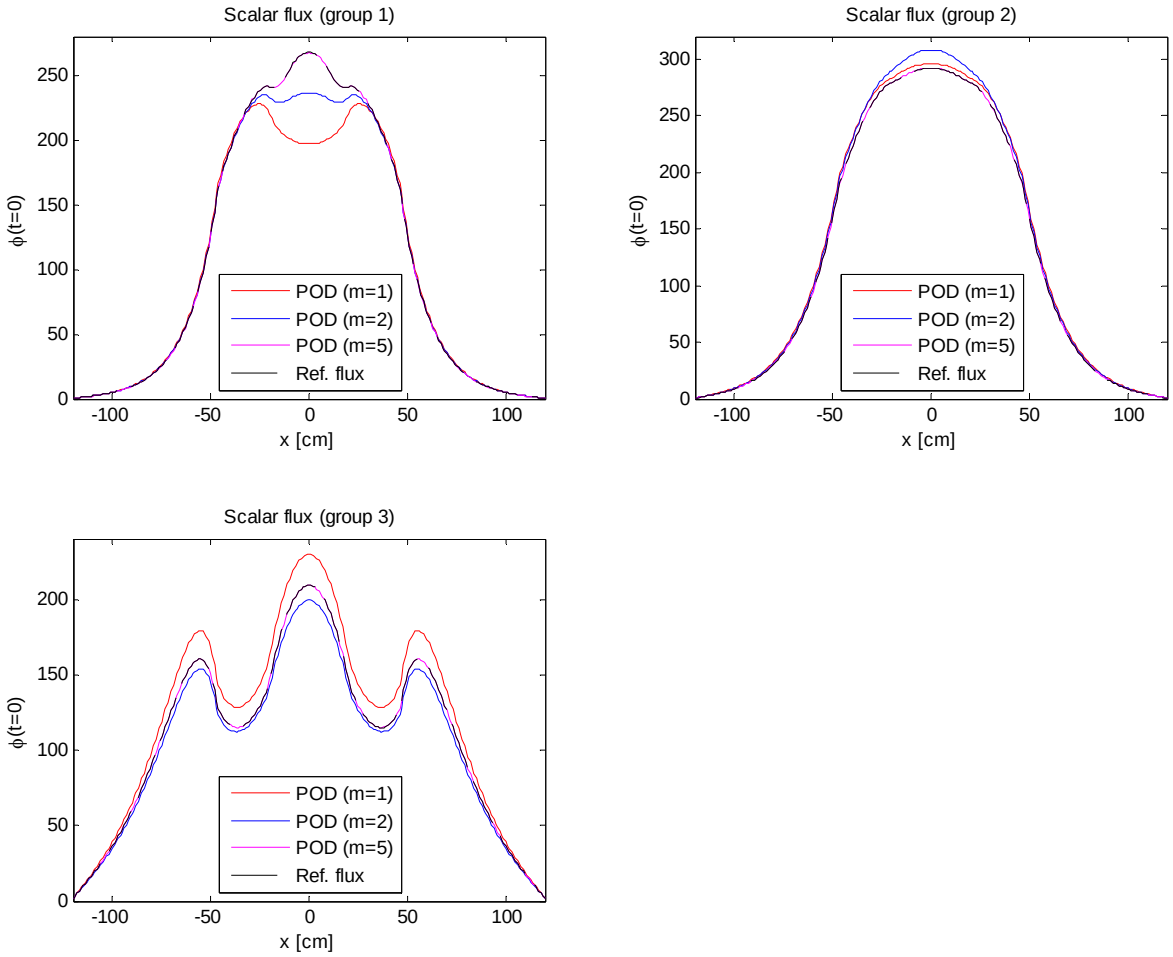

Figure 6.9 Steady-state flux reconstruction for 3 groups of 1D ADS by 1, 2 or 5 POD basis functions

It appears that the use of only five POD basis functions already leads to very accurate results. The flux from this POD reconstructed flux is almost indistinguishable from the reference steady-state flux.

6.4.4 Concluding remarks about the POD

The POD in combination with the Galerkin projection upon the neutron transport equation might be an interesting way to model the time-dependent behaviour of a system. Though it should be noted that its application is less general than the alpha modes expansion since one particular time-dependent solution with fixed source strength and position is sampled to obtain the basis functions. In the alpha mode expansion the user can describe varying source strengths and/or positions with the same set of alpha modes.

The basis functions of the POD are more like a mathematical trick while the alpha modes and lambda modes originate from a more physical basis incorporating features of the reactor geometry and the neutron transport equation. As a result the POD requires the application of the transport operator $\mathbf{L}$. Application of the transport operator $\mathbf{L}$ involves calculating the transport term, given by $-\hat{\Omega}\cdot\nabla\psi\left(\vec{r},E,\hat{\Omega},t\right)$, of eq. (3.1). This is a non-trivial task but also the scattering term $\int_{4\pi}\int_{0}^{\infty}\Sigma_s\left(\vec{r},E'\rightarrow E,\hat{\Omega}'\rightarrow\hat{\Omega},t\right)\psi\left(\vec{r},E',\hat{\Omega}',t\right)dE'd\hat{\Omega}'$, can in case of anisotropic scattering become complicated. This would have made the programming of an appropriate numerical code a very

comprehensive task and beyond the scope of this thesis. It should also be noted that application of the transport operator $\mathbf{L}$ can be computationally demanding. But a study of the possibilities of the POD in time-dependent neutron transport problems might be an interesting subject for future research.

6.5 Conclusions

The lambda modes expansion was applied to a 1D ADS model using a one group and a three group energy discretization. For both one and three energy groups the lambda modes reconstruction of the steady-state neutron flux leads to reasonable results except for the non-fissile source region.

For the transient scenario of turning off a source after operating under steady-state conditions the time-integration of the lambda modes leads to some deviation from the reference flux in the one-group case and significant deviations in the three-group case. The alpha mode expansion leads to much more accurate results in the three-group case. The lambda modes are much cheaper to calculate than the alpha modes, but it seems that they can only be used as a very rough estimate in the description of time-dependent problems.

During some of the cases studied in this chapter the use of a large number of lambda modes led to an unstable system of differential equations to describe the time dependence of the expansion coefficients. This instability is probably caused by inaccuracies in the determination of the higher lambda modes. Since in the cases studied the fundamental lambda mode was usually by far the most important component of the lambda mode reconstruction and the higher modes were only of small influence the instability of the system of ODEs was not such a problem. For systems requiring a large number of lambda modes in the expansion for an accurate reconstruction of the flux the instability will be a very serious issue.

The instability of the system of ODEs and the quite inaccurate description of the time-dependency of the neutron flux by the lambda modes expansion makes the alpha modes expansion the preferable modal expansion technique for the description of space-time kinetics in accelerator driven systems.

The proper orthogonal decomposition was investigated as a method to construct a basis for a modal expansion method. It was shown that the POD basis vectors can be used to reconstruct the steady-state reference flux of a 1D ADS model.

A major drawback of applying the POD to time-dependent problems is its requirement to apply the transport operator. The transport operator is difficult to implement, since it involves the $-\hat{\Omega}\cdot\nabla$-term and in general it can involve anisotropic scattering. The transport operator is also computationally demanding to calculate. This made practical implementation of this method for transient calculations too elaborate for this moment. It is also not completely clear what the real advantages of the POD in the field of neutron transport might be. But in the future it might be interesting to study the possibilities of applying the POD in time-dependent neutron transport problems.

7 Conclusions and Future work

7.1 Conclusions

It was shown with a 1D diffusion model in chapter 2 that the role of the delayed neutrons reduces significantly as the subcriticality of a system increases and that the delayed neutrons can be considered as a constant background upon the time scales considered during the transient calculations of this thesis.

The alpha modes are used as a basis for the modal expansion technique and direct time-dependent calculations are performed by PHANTOM to check the accuracy of the modal expansion technique. Therefore it was verified with several testcases that the PHANTOM code package calculates the alpha eigenvalues correctly and that the time-integration during the direct time-dependent transport calculation is performed correctly by PHANTOM in chapter 3.

In chapter 4, k_{eff} was calculated for the critical configuration of the GUINEVERE facility and the value obtained by PHANTOM was close to reference calculations with ERANOS and MCNP. It was unfortunately not possible to calculate a substantial number of alpha modes for the subcritical configuration within a reasonable time-frame, because the calculation of the alpha modes converges very slowly, especially for multi-group problems. The study of the influence of a start-up and a shutdown of the source showed that the build-up or decay of the neutron flux in the 9th and 10th energy group takes place on a much slower time scale than in the lower energy groups (containing the highest neutron energies). This difference in time scale, apart from the slow convergence of the calculation, would also complicate the calculations of the relevant alpha modes for the modal flux reconstruction, since the most important physical processes take place in the first eight energy groups on a faster time scale. For the calculation of the relevant alpha modes the slower time scales should be excluded from the calculation.

The alpha mode expansion technique has been applied to a 1D ADS model and a 2D ADS model in chapter 5 using a 1 and 3-energy group discretization and to another 2D model with the cross sections used during the GUINEVERE calculations. The alpha mode expansion was used to describe the flux of the steady-state problem and the transient scenarios of starting up and turning off the source. The 1D ADS model was also studied using 3 energy groups for a source operating in a pulsed mode. For these transient scenarios the alpha mode expansion technique can describe the time-dependency of the modal expansion coefficients by analytical expressions.

In general it was found that the alpha mode expansion technique has difficulties to describe the neutron flux correctly inside the source region for the energy group of the source at the moment the source is switched on or shortly afterwards. Outside the source region and for the other energy groups the alpha mode reconstruction was usually quite accurate. During a start-up of the source most of the error in reproducing the flux is created by the processes on a very fast time scale during the first instants of the transient. After a shutdown of the source the alpha mode expansion describes the neutron flux very well except for the very early stages of the transient, which are again associated with the very fast time scales in the system. In practical cases often more than 50 modes are required to describe these fast time scales. The errors in the flux reconstruction can in all cases be contributed to the missing higher alpha modes, associated with these faster time scales, in the modal expansion.

The determination of the higher alpha modes by PHANTOM with the Arnoldi method was often found to be difficult. In the first place the calculations are computationally expensive due to slow convergence of the calculation. The higher modes are also often calculated in a numerically less accurate way for the higher modes, the difference between the eigenvalues of the forward and adjoint calculation is often bigger for a higher mode. Sometimes eigenvalues are skipped during the forward or adjoint calculation. This also happens more often for the higher modes. In the 2D case the addition of a higher alpha mode sometimes deteriorates the quality of the flux reconstruction. This could be caused by the coarseness of the mesh used in the 2D models. The mesh is not capable of representing a mode that varies rapidly in the spatial domain due to the limited number of nodes. Refining the mesh is however also not always possible due to the computational time required for the determination of the alpha modes.

It should be concluded that the alpha mode expansion technique can already reconstruct the time-dependent neutron flux of an ADS quite accurately during a transient, except in the source region for the flux contributions associated with the very fast time scales. Improvements of the calculation of the (higher) alpha modes would significantly improve the accuracy of the modal expansion technique for these fast time scales.

Lambda modes were investigated as a possible alternative basis for the modal expansion technique in chapter 6. The lambda mode expansion technique was applied to the same 1D ADS used with the alpha modes and the results were compared with the reference solution and the alpha mode expansion. It was discovered that the lambda mode expansion can describe the flux reasonably for the steady-state problem except for the non-fissile source region. The fundamental mode was by far the most important mode of the reconstruction. In contrast to the alpha mode expansion the time-dependency of the lambda mode expansion coefficients is described by a coupled set of ODEs. The use of a large number of modes resulted in an unstable system of ODEs. The instability is probably caused by numerical inaccuracies in the determination of the higher modes. If only a limited number of modes was used this problem did not occur. The reconstruction of the time-dependent flux by the lambda mode expansion led to quite inaccurate results. Despite the short calculation time of the lambda modes the alpha modes are a much better option to describe the time-dependent neutron flux in an ADS in an accurate way.

The POD basis functions were also investigated as a possible alternative basis for a modal expansion technique. Only a few POD basis functions were required to reconstruct the steady-state flux. A major drawback of applying the POD to time-dependent problems is its requirement to apply the transport operator, which is difficult to implement and computationally demanding to calculate. For this reason practical implementation of the POD for transient calculations would have been beyond the scope of this thesis. In the future it might be interesting to study the possibilities of applying the POD in time-dependent neutron transport problems.

7.2 Future work

As indicated in the conclusions of the thesis the alpha mode expansion technique itself can accurately describe the time-dependent neutron flux in a system, but the accuracy is limited because of difficulties with the determination of the alpha modes and the applicability is limited because of the time required to calculate the alpha modes. The most important recommendation for future research is

to work on a speed up of the calculation of the alpha modes by PHANTOM and to improve the accuracy of the determination of the higher alpha modes.

If a significant speed up of the alpha mode calculation can be implemented in PHANTOM the alpha modes of the subcritical configuration of the 3D GUINEVERE model can be calculated and the alpha mode expansion technique can be applied to describe the transients of the 3D model of GUINEVERE and other 3D ADS models.

For the short time scales of the transients considered during the thesis the delayed neutrons could be considered as a constant background. When the time-dependent neutron flux is studied for transient upon a longer time scale ($> 0.1\ s$) it will be necessary to include delayed neutrons into the computation of the alpha modes. The appropriate expressions describing the modal expansion coefficients are given by Cao [2008].

An interesting idea for future research is to investigate the possibility of calculating alpha modes for (super)critical systems. By an appropriate shift during the calculation also the alpha modes for (super)critical systems can be determined. This might offer the possibility of using alpha modes for the description of critical systems. The possibility of a shift in the other direction can also be investigated to improve the accuracy and to speed up the calculation of the higher alpha modes in subcritical systems.

Finally for more complex geometries it might be very interesting to investigate the possibilities of using the proper orthogonal decomposition in combination with the Galerkin projection to describe the time-dependent neutron flux during a transient.

Acknowledgements

At the end of this MSc.-thesis I would especially like to thank Dr. D. Lathouwers, section PNR, TU Delft, for his supervision over my master's project. Danny's input during the weekly meetings was very valuable for the progress made during the thesis and helped me to keep a critical view upon my own research. I would also like to thank Danny for his feedback during the process of writing the thesis report.

I would also like to thank ir. W. Uyttenhove, from the SCK in Mol, for his input for my project, especially considering the GUINEVERE facility, and I would also like to thank Wim for the monthly conversations about my masters project. Of course I would also like to express thanks to the other members of the thesis committee and the people of the PNR-group for their assistance during the project.

Finally I would like to express thanks to you as a reader for your interest in reading my thesis about modal expansion techniques and transients in accelerator driven systems.

A Spherical harmonics polynomials and their properties

This appendix gives an overview of the real spherical harmonics polynomials used by PHANTOM for the discretization of the angular dependence of the neutron flux. In quantum mechanics the complex Y_{lm}-functions are used [Griffiths, 2005]. The neutron flux is however a real quantity making it desirable to work with an alternative set of Y_{lm}-functions compared to the complex Y_{lm}-functions encountered in quantum mechanics. Before giving the definition of the real spherical harmonics polynomials, the Legendre polynomials and associated Legendre polynomials must be defined. The Legendre polynomials $P_l(\mu)$ are defined as

$$P_l(\mu) = \begin{cases} 1 & l = 0 \\ \dfrac{1}{2^l l!}\dfrac{d^l}{d\mu^l}\left(\mu^2 - 1\right)^l & l > 0 \end{cases}, \tag{A.1}$$

and the associated Legendre polynomials for $m \geq 0$ are defined as

$$P_l^m(\mu) = (-1)^m \left(1-\mu^2\right)^{m/2} \frac{d^m}{d\mu^m} P_l(\mu). \tag{A.2}$$

The real spherical harmonics are also described by Weisstein [2003]. PHANTOM divides the real spherical harmonics into even parts Y_{lm}^e and odd parts Y_{lm}^o, defined as

$$\begin{aligned} Y_{lm}^e &= \sqrt{\frac{2l+1}{4\pi}\left(2-\delta_{m,0}\right)\frac{(l-m)!}{(l+m)!}} P_l^m(\mu)\cos(m\chi); \qquad 0 \leq m \leq l \\ Y_{lm}^o &= \sqrt{\frac{2l+1}{4\pi}\left(2-\delta_{m,0}\right)\frac{(l-m)!}{(l+m)!}} P_l^m(\mu)\sin(m\chi); \qquad 0 < m \leq l \end{aligned}. \tag{A.3}$$

An important and very convenient property of the real spherical harmonics polynomials is their orthonormality, which is characterized by

$$\begin{aligned} &\int_{4\pi} Y_{lm}^e(\Omega) Y_{l'm'}^e(\Omega)\, d\Omega = \delta_{l,l'}\delta_{m,m'} \\ &\int_{4\pi} Y_{lm}^o(\Omega) Y_{l'm'}^o(\Omega)\, d\Omega = \delta_{l,l'}\delta_{m,m'} \\ &\int_{4\pi} Y_{lm}^e(\Omega) Y_{l'm'}^o(\Omega)\, d\Omega = 0 \end{aligned}. \tag{A.4}$$

B Orthogonality of alpha and lambda modes

B.1 Orthogonality of the alpha modes

The orthogonality relations of the α-modes are used in section 5.1.2 to obtain the uncoupled set of ODEs describing the expansion coefficients of the α-mode expansion. The orthogonality relations are derived in the following way. The forward α-eigenvalue equation, given by eq. (3.31), is multiplied with $\psi_\alpha^\dagger$, and the adjoint α-eigenvalue equation, given by eq. (3.32), is multiplied with ψ_α. Both equations are integrated over the whole phase-space and the second equation obtained is subtracted from the first one. The inner product is defined by integration over the whole range of space, energy and angle

$$\langle f, g \rangle = \int_V \int_E \int_\Omega f\left(\vec{r}, E, \hat{\Omega}\right) g\left(\vec{r}, E, \hat{\Omega}\right) d\hat{\Omega} dE dV \,. \tag{B.1}$$

The following relation is obtained

$$\left(\alpha_n - \alpha_m{}^\dagger\right)\left\langle \frac{\psi_m^\dagger}{V}, \psi_n \right\rangle = \left\langle \psi_m^\dagger, \left[\mathbf{F}-\mathbf{L}\right]\psi_n \right\rangle - \left\langle \psi_n, \left[\mathbf{F}-\mathbf{L}\right]^\dagger \psi_m^\dagger \right\rangle, \tag{B.2}$$

where ψ_m and ψ_n represent the m-th and the n-th α-eigenfunction. By definition of the adjoint operator $\langle f, \mathbf{A}g \rangle = \langle g, \mathbf{A}^\dagger f \rangle$ the two terms on the right hand-side are equal. The final orthogonality relation is obtained

$$\left(\alpha_n - \alpha_m{}^\dagger\right)\left\langle \frac{\psi_m^\dagger}{V}, \psi_n \right\rangle = 0 \,. \tag{B.3}$$

It is concluded that either the inner product $\left\langle \frac{\psi_m^\dagger}{V}, \psi_n \right\rangle$ is equal to zero or α_n must be equal to $\alpha_m{}^\dagger$ or both. $\frac{\psi_m^\dagger}{V}$ and ψ_n are orthogonal in case of non-degenerate eigenvalues. The preceding derivation of the biorthogonality relation of the α-modes can also be found in chapter 6 of Bell & Glasstone [1985].

B.2 Orthogonality of the lambda modes

The λ-modes, introduced in section 3.5.1, were used in chapter 6 to perform a modal expansion of the time-dependent neutron flux. The biorthogonality relations of the λ-modes were used to simplify the system of ODEs describing the evolution of the modal expansion coefficients over time. The bi-orthogonality relations of the lambda modes are derived as follows.

The λ-eigenvalue problem eq. (3.35) is multiplied with $\psi_m^\dagger$ and the adjoint λ-eigenvalue problem eq. (3.36) with ψ_l. Then all terms are integrated over the whole phase-space and the second equation is subtracted from the first one, leading to

$$\left\langle \psi_m^\dagger, \mathbf{L}\psi_l \right\rangle - \left\langle \psi_l, \mathbf{L}^\dagger \psi_m^\dagger \right\rangle = \left\langle \psi_m^\dagger, \frac{\mathbf{F}}{\lambda_l}\psi_l \right\rangle - \left\langle \psi_l, \frac{\mathbf{F}^\dagger}{\lambda_m^\dagger}\psi_m^\dagger \right\rangle. \tag{B.4}$$

When the definition of the adjoint operator $\langle f, \mathbf{A}g \rangle = \langle g, \mathbf{A}^\dagger f \rangle$ is used the terms on the left hand side cancel out and the inner products on the right hand side can be combined

$$\left(\frac{1}{\lambda_l} - \frac{1}{\lambda_m^\dagger}\right)\left\langle \psi_m^\dagger, \mathbf{F}\psi_l \right\rangle = 0 \,. \tag{B.5}$$

Either the inner product $\left\langle \psi_m^\dagger, \mathbf{F}\psi_l \right\rangle$ is equal to zero or λ_l must be equal to $\lambda_m{}^\dagger$ or both. In absence of degenerate eigenvalues the adjoint λ-mode $\psi_m^\dagger$ is orthogonal to $\mathbf{F}\psi_l$. It is important to notice that this biorthogonality relation for the λ-modes involves the fission operator $\mathbf{F}$. This makes the biorthogonal properties of the λ-modes slightly more inconvenient than the biorthogonal properties of the α-modes.

C Cross section processing by the SCALE package

In this appendix the script that was used to generate cross sections with SCALE for the GUINEVERE calculations in chapter 4 and section 5.6 is given. A 238-group library is used to calculate the cross sections.

```
=shell
ln -fs /home/pnr/inas/scale5.1/data/scale.rev02.xn238v6 xn238
end
=csasi parm=centrm

xn238
```

The material compositions are defined for four materials. (1 = Uranium, 2 = Nickel cladding, 3 = Lead and stainless steel mixture in one fuel assembly, 4 = B_4C of the control/safety rods)

```
read comp
U-235  1 0 1.4280E-2 300 END
U-238  1 0 3.2899E-2 300 END
NI-58  2 0 6.2170E-2 300 END
NI-60  2 0 2.3920E-2 300 END
NI-61  2 0 1.0400E-3 300 END
NI-62  2 0 3.3115E-3 300 END
NI-64  2 0 8.4841E-4 300 END
N-14   3 0 2.8109E-5 300 END
N-15   3 0 1.0437E-7 300 END
O-16   3 0 6.0769E-7 300 END
C      3 0 5.5382E-5 300 END
PB-206 3 0 6.0235E-3 300 END
PB-207 3 0 5.8669E-3 300 END
PB-208 3 0 1.3082E-2 300 END
FE-54  3 0 6.6387E-4 300 END
FE-56  3 0 1.0421E-2 300 END
FE-57  3 0 2.4059E-4 300 END
FE-58  3 0 3.1775E-5 300 END
NI-58  3 0 8.6344E-4 300 END
NI-60  3 0 3.3253E-4 300 END
NI-61  3 0 1.4858E-5 300 END
NI-62  3 0 4.7311E-5 300 END
NI-64  3 0 1.2138E-5 300 END
CR-50  3 0 1.3645E-4 300 END
CR-52  3 0 2.6281E-3 300 END
CR-53  3 0 2.9797E-4 300 END
CR-54  3 0 7.4024E-5 300 END
SI-28  3 0 1.6297E-4 300 END
SI-29  3 0 8.2519E-6 300 END
SI-30  3 0 5.4774E-6 300 END
MO-94  3 0 1.5220E-6 300 END
MO-95  3 0 2.6196E-6 300 END
MO-96  3 0 1.0742E-5 300 END
MO-97  3 0 1.5715E-6 300 END
CO-59  3 0 1.7408E-5 300 END
CU-63  3 0 2.9207E-5 300 END
CU-65  3 0 1.3018E-5 300 END
MN-55  3 0 2.7221E-5 300 END
P-31   3 0 1.4753E-5 300 END
B-10   4   2.0330E-2 300 END
B-11   4   8.1793E-2 300 END
C      4   5.1059E-2 300 END
```

A self-shielding calculation is performed for a square pitch fuel pin in an infinite lattice. The square pitch consists of three layers: fuel (material 1), clad (material 2) and moderator (material 3).

```
read celldata
latticecell squarepitch
fuelr=0.6282 1
cladr=0.6350 2
hpitch=1.3333 3
cellmix=1111 end
more data adj=0 cof=3 bal=fine icon=cell
end more
end celldata
end
=shell
mv ft03f001 $RTNDIR/wght.out
mv ft02f001 $RTNDIR/1.mixd
ln -fs /home/fwols/scale/boron/1.mixd
ft04f001
end
```

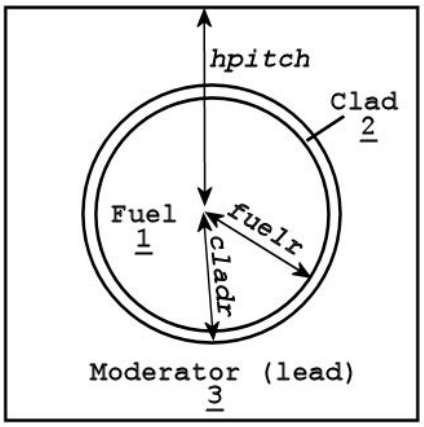

Figure C.1 Scheme of square pitch fuel pin

Both the 238-group cross sections of the homogenized fuel pin and the separate material regions are extracted and used in `xsdrn` to collapse the 238 group cross sections into 10 energy groups for the materials of the homogenized fuel assembly, the lead/stainless steel mixture and the B_4C of the control and safety rods. For the calculation one cylindrical pin with a height of 60.96 *cm* is used. The cross sections in the output contain up to 5th order scattering.

```
=xsdrn
collapsing
0$$ a3 4 a5 3 e
1$$ 2 3 17 a6 3 3 16 5 1 e
3$$ 1 e
4$$ -1 10 3 -2 e
5* a7 60.96 t
13$$     1       2  3
14$$    1111     3  4
15**     1       1  1
t
33## f1 t
35** 14i 0.0 1.5 1.50005 1.5045e
36$$ 15r1 2 3e
39$$ 1 3 2e
51$$ 22r1 8r2 9r3 5r4 7r5 6r6 13r7 15r8
     104r9 49r10 t
end
=shell
cp ft03f001 $RTNDIR/xs_10br.out
end
```

The set of cross sections obtained in `xs_10br.out` for the three materials (fuel assembly, lead and B_4C) is used in the calculations of the GUINEVERE facility.

Bibliography

G.I. Bell and S. Glasstone, Nuclear Reactor Theory, Robert E. Krieger Publishing, 1985.

G. Bianchini, M. Carta, F. Pisacane, M. Frisoni, V. Peluso, Set-up of a deterministic model for the analysis of the GUINEVERE experience, PHYSOR Conference, Pittsburgh, 2010.

R.L. Borrelli, C.S. Coleman, Differential equations: a modeling perspective, John Wiley & Sons Inc., 1998.

P. Bosio, P. Ravetto, M. Rostagno, A. Barzilov, Multipoint methods in nuclear reactor kinetics, Mathematical methods for nuclear applications, Salt Lake City, 2001.

Y. Cao, Space-time kinetics and time-eigenfunctions, PhD. Thesis, University of Michigan, 2008.

E.B. Dahl, V. Protopopescu, N. Sjöstrand, On the relation between decay constants and critical parameters in monoenergetic neutron transport, Nuclear Science and Engineering, vol. 83, pp. 374-379, 1983.

J. Duderstadt and L. Hamilton, Nuclear Reactor Analysis, Wiley Interscience, 1976.

S. Dulla, P. Ravetto, M. Rostagno, G. Bianchini, M. Carta and A. D'Angelo, On some features of spatial neutron kinetics for multiplying systems, International Conference on Mathematics and Computation, Gatlinburg, 2003.

S. Dulla and P. Picca, Consistent multipoint kinetics for source-driven systems, Progress in nuclear Energy, vol.48, pp. 617-628, 2006.

F. Fang, C.C. Pain, I.M. Navon, G.J. Gorman, M.D. Piggott, P.A. Allison, P.E. Farrell and A.J.H. Goddard, A POD reduced order unstructured mesh ocean modeling method for moderate Reynolds number flows, Ocean Modelling, Vol. 28, pp. 127-136, 2009.

M. Gockenbach, Understanding and implementing the finite element method, Society for Industrial and Applied Mathematics, 2006.

S. González-Pintor, D. Ginestar, G. Verdú, Time integration of the neutron diffusion equation on hexagonal geometries, To appear in: Mathematical and Computer modeling, 2010.

A. Greenbaum, Iterative methods for solving linear systems, Society for Industrial and Applied Mathematics, 1997.

David J. Griffiths, Introduction to Quantum Mechanics, Second edition, Pearson Prentice Hall, 2005.

L. Hogben, Handbook of linear algebra: discrete mathematics and its applications, Chapmann and Hall/CRC, 2007.

E. Isaacson, H. B. Keller, Analysis of numerical methods, Dover Publications, 1994.

J. Van Kan, A. Segal, F. Vermolen, Numerical Methods in Scientific Computing, VSSD, 2005.

D. Lathouwers, Iterative computation of time-eigenvalues of the neutron transport equation, Annals of Nuclear Energy, vol. 30, pp. 1793-1806, 2003.

D. Lathouwers, Neutron Transport Discretization using a Least-Squares Approach, PNR, Delft University of Technology, 2007.

R. Lehoucq, D. Sorensen and C. Yang, ARPACK Users' Guide: Solution of Large Scale Eigenvalue Problems with Implicitly Restarted Arnoldi Methods, 1997.

Z. de Lima, F. da Silva, A. Alvim, A modal multidimensional kinetics method using pseudo-harmonics, Annals of Nuclear Energy, vol. 36., pp. 752-759, 2009.

P. Ravetto, Problems in the neutron dynamics of source-driven systems, Part of: Nuclear Reaction Data and Nuclear Reactors, pp. 843-868, 2000, Vol. 2.

P. Ravetto, S. Dulla and M. Rostagno, Accelerator-Driven Systems (ADS) Dynamics, Workshop at the 2003 IAEA meeting on technology and applications of Accelerator Driven Systems (ADS), Trieste, 2003.

P. Saracco and G. Ricco, Various operating regimes of a subcritical system as a function of subcriticality in one-group theory, Nuclear Science and Engineering, vol. 162, pp. 167-177, 2009.

K.P. Singh, R.S. Modak, S.B. Degweker, Kanchhi Singh, Iterative schemes for obtaining dominant alpha-modes of the neutron diffusion equation, Annals of Nuclear Energy, Vol. 36, pp. 1086-1092, 2009.

G. Strang, An analysis of the finite element method, Prentice-Hall, 1973.

W. Uyttenhove, P. Baeten, GUINEVERE: Safety studies – Neutronics Calculations, SCK CEN, Technical Report R-4705 v. 2, 2008.

W. Uyttenhove, P. Baeten, G. Van den Eynde, A. Kochetkov, D. Lathouwers and M. Carta, The neutronic design of a critical lead reflected zero-power reference core for on-line subcriticality measurements on ADS, *submitted for* Annals of Nuclear Energy, 2010.

G. Verdu, D. Ginestar, J. Roman, V. Vidal, 3D Alpha modes of a nuclear power reactor, Journal of Nuclear Science and Technology, Vol. 47, No. 5, pp. 501-514, 2010.

Eric W. Weisstein, CRC concise encyclopedia of mathematics, Second edition, Chapman & Hall / CRC, 2003.

M. Williams, CRC Handbook of Nuclear Reactor Calculations, Volume III: Perturbation theory analysis, CRC Press Inc., 1988.

Zienkiewicz, Taylor, The finite element method: Volume 1: The Basis, Butterworth Heinemann, 5th ed., 2000.